Journal of Nanomaterials

Nanocomposites

Guest Editor: Chunxiang Cui

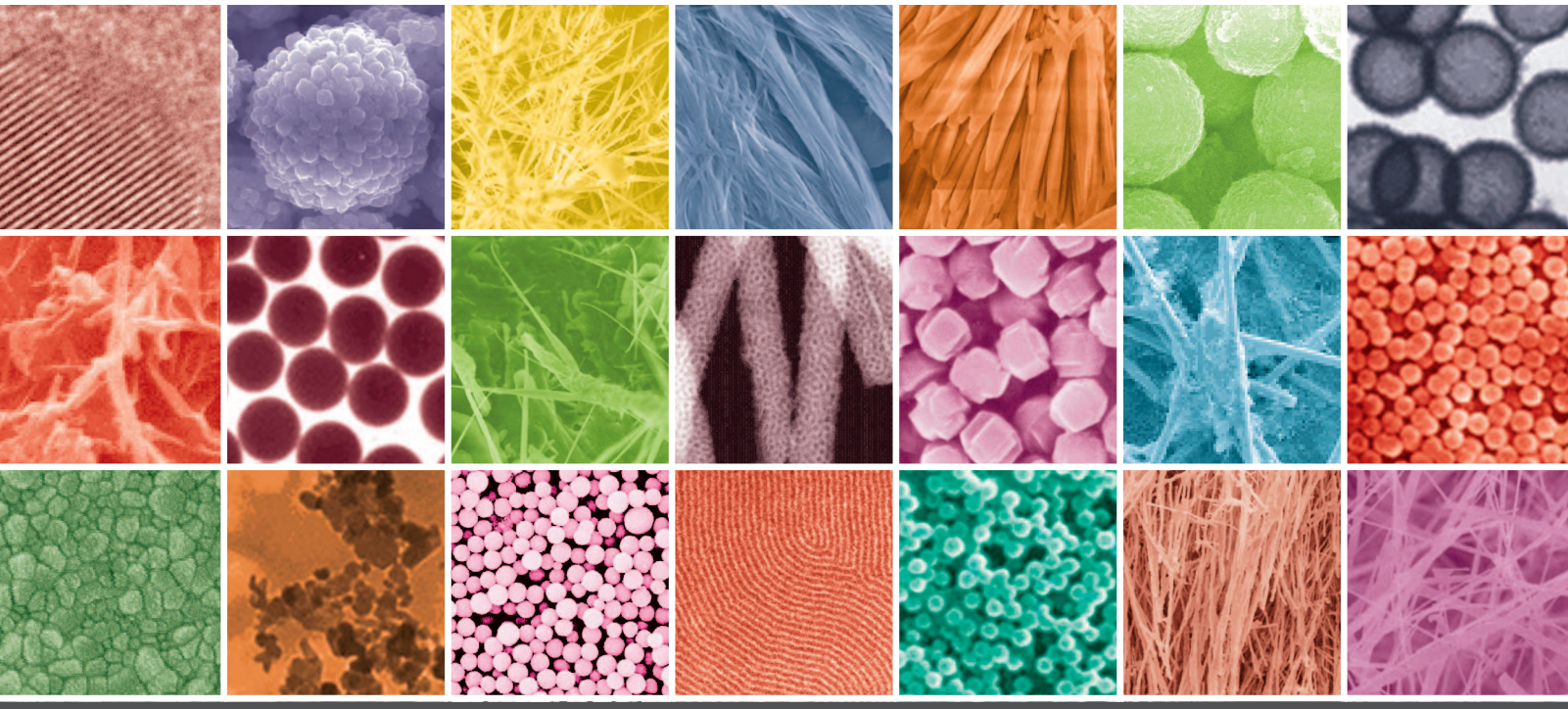

Nanocomposites

Journal of Nanomaterials

Nanocomposites

Guest Editor: Chunxiang Cui

Contents

Hindawi Publishing Corporation
Journal of Nanomaterials
Volume 2006, Article ID 32803, Pages 1–7
DOI 10.1155/JNM/2006/32803

Damping Augmentation of Nanocomposites Using Carbon Nanofiber Paper

Jihua Gou,[1] Scott O'Braint,[1] Haichang Gu,[2] and Gangbing Song[2]

[1] *Department of Mechanical Engineering, University of South Alabama, Mobile, AL 36688-0002, USA*
[2] *Department of Mechanical Engineering, University of Houston, Houston, TX 77204-4006, USA*

Received 11 January 2006; Accepted 4 May 2006

Vacuum-assisted resin transfer molding (VARTM) process was used to fabricate the nanocomposites through integrating carbon nanofiber paper into traditional glass fiber reinforced composites. The carbon nanofiber paper had a porous structure with highly entangled carbon nanofibers and short glass fibers. In this study, the carbon nanofiber paper was employed as an interlayer and surface layer of composite laminates to enhance the damping properties. Experiments conducted using the nanocomposite beam indicated up to 200–700% increase of the damping ratios at higher frequencies. The scanning electron microscopy (SEM) characterization of the carbon nanofiber paper and the nanocomposites was also conducted to investigate the impregnation of carbon nanofiber paper by the resin during the VARTM process and the mechanics of damping augmentation. The study showed a complete penetration of the resin through the carbon nanofiber paper. The connectivities between carbon nanofibers and short glass fibers within the carbon nanofiber paper were responsible for the significant energy dissipation in the nanocomposites during the damping tests.

1. INTRODUCTION

In recent years, nanoparticles have been attracting increasing attention in the composite community as they are capable of improving the mechanical and physical properties of traditional fiber reinforced composites [1–4]. Their nanometer size, leading to high specific surface areas of up to more than 1000 m^2/g and extraordinary mechanical, electrical, and thermal properties make them unique nano-fillers for structural and multifunctional composites. Commonly used nanoparticles in nanocomposites include multiwalled nanotubes (MWNTs), single-walled nanotubes (SWNTs), carbon nanofibers (CNFs), montmorillonite (MMT) nanoclays, and polyhedral oligomeric silsesquioxanes (POSS). Other nanoparticles, such as SiO_2, Al_2O_3, TiO_2, and nanosilica are also used in the nanocomposites. Compared to other particulate additives, carbon nanotubes and carbon nanofibers offer more advantages. The addition of small size and low loading of carbon nanotubes and carbon nanofibers can enhance the matrix-dominated properties of composites, such as stiffness, fracture toughness, and interlaminar shear strength [5–9]. They have proven to be excellent additives to impart electrical conductivity in nanocomposites at lower loadings due to their high electrical conductivity and aspect ratio [10–12]. In addition, they have better performance as flame retardant by reducing the heat release rate of polymer and conducting heat away from the flame zone [13, 14].

While there are many reported benefits of carbon nanotubes and carbon nanofibers in composites, the potential of carbon nanotubes and carbon nanofibers to enhance the damping properties of composites has been less explored. Traditional damping enhancements of composites are based on viscoelastic polymer materials [15], carbon fiber prepregs [16], and magnetostrictive particles [17]. The major limitations of the viscoelastic polymer materials are the structural integrity issue, the sacrifice of stiffness and strength of the composite system due to the resin penetration, and poor thermal stability. Kishi et al. [16] evaluated the damping properties of composite laminates with/without the interleaved films. The effects of the lay-up arrangements of carbon fiber prepregs on the damping properties of the interleaved laminates were examined. The viscoelastic properties of interleaved polymer films were reflected in the damping properties of the corresponding interleaved laminates. Magnetostrictive particles have been used in a polymer matrix as active transducer and passive damper, providing stiffness and strength while incorporating damping capabilities. Pulliam et al. [17] developed a novel manufacturing technique based on magnetic fields to distribute magnetostrictive

particles in polymer resins and applied them in thin-layer on the surfaces for vibration damping. Recently, carbon nanotubes have been used in the composite system for structural damping and stiffness augmentation. Suhr et al. [18] conducted direct shear testing of epoxy thin films containing multiwalled carbon nanotubes and reported strong viscoelastic behavior with up to 1400% increase in loss factor (damping ratio) of the baseline epoxy resin. The great improvement in damping was achieved without sacrificing the mechanical strength and stiffness of the polymer, and with minimal weight penalty. Koratkar et al. [19, 20] fabricated multiwalled nanotube thin films by using catalytic chemical vapor deposition of xylene-ferrocene mixture precursor. The nanotube films were employed as interlayers to reinforce the interfaces between composite plies, enhancing laminate stiffness and structural damping. The flatwise bending tests of a piezosilica composite beam with an embedded nano-film sublayer indicated up to 200% increase in the damping level and 30% increase in the baseline bending stiffness.

Traditionally, researchers fabricated composites by directly mixing carbon nanotubes and carbon nanofibers into polymers and then using casting and injection techniques to make nanocomposites. Gou et al. [21, 22] have developed a new technique approach to fabricate nanocomposites using single-walled carbon nanotube bucky papers. The experimental details of fabrication of single-walled carbon nanotube bucky paper can be found in reference [23]. The dynamic mechanical analysis (DMA) results indicated an enhancement of the thermomechanical properties of single-walled carbon nanotube bucky paper/epoxy resin nanocomposites. The present work describes the integration of carbon nanofiber paper as damping material into large structural level laminates-glass fiber reinforced composites. The very first time an example of carbon nanofiber paper-enabled nanocomposites in the dimension of a structural element is presented. The manufacturing via VARTM and the investigation of the damping properties and tensile properties of the fabricated nanocomposites are described.

2. EXPERIMENTAL DETAILS

2.1. Materials

The carbon nanofiber paper used in this study was obtained from Applied Sciences, Inc. The carbon nanofiber paper had good strength and flexibility to allow for handling like traditional glass fiber mat. The carbon nanofiber paper was composed of short glass fibers and vapor grown carbon nanofibers (Polygraf III) with diameter of 100–150 nm and length of 30–100 μm. The short glass fiber and carbon nanofibers appeared in an entangled and porous form within the paper. The unsaturated polyester resin (product code: 712–6117, Eastman Chemical Company) was used as matrix material for glass fiber reinforced composites. The polyester resin was used with the MEK peroxide hardener at a weight ratio of 100 : 1.

2.2. Manufacturing of carbon nanofiber paper-enabled nanocomposites

The VARTM process has been widely used to produce low-cost, high-quality, and geometrically complicated composite parts. In this study, the VARTM process was used to fabricate the carbon nanofiber paper-enabled nanocomposites, which was carried out in three steps. In the first step, glass fiber mats carbon nanofiber paper were placed on the bottom half of a mold. After the lay-up operation was completed, a peel ply, resin distribution media, and vacuum bag film were placed on the top of fiber mats. The vacuum film bag was then sealed around the perimeter of the mold and a vacuum pump was used to draw a vacuum within the mold cavity. The next step was the mold filling during which resin was sucked into the mold under atmospheric pressure. In the VARTM process, the distribution media provided a high permeability region in the mold cavity, which allowed the resin to quickly flow across the surface of the laminate and then wet the thickness of the laminate. Therefore, the dominant impregnation mechanism in the VARTM process was the through-thickness flow of resin. In the final step, the composite part was cured at room temperature for 24 hours and post-cured in the oven for another 2 hours at 100°C.

In this study, the test laminates consisted of six plies of fiberglass with a single layer of carbon nanofiber paper embedded at the surface or the midplane. In the manufacturing of composite laminates with carbon nanofiber as an interlayer, one layer of carbon nanofiber paper was placed between the fiber mats. The peel ply and resin distribution media were used on both top and bottom sides to facilitate the resin flow through the thickness.

2.3. Damping test of carbon nanofiber paper-enabled nanocomposites

The regular composite beam without carbon nanofiber paper and the nanocomposite beam with carbon nanofiber paper were used as the specimens for damping test. For each beam, a PZT (lead zirconate titanate, a type of piezoceramic material) patch (20 mm $\times$ 20 mm) was attached on one side as an actuator to excite the beam and a smaller PZT patch (10 mm $\times$ 8 mm) was attached on the other side of the beam as a sensor to detect the beam's vibration, as shown in Figure 1. A micro laser sensor (NAIS-LM10-ANR12151) was also used to detect the beam's tip displacement. The micro laser sensor had a resolution of 20 μm (0.0008 inch). The testing specimen was clamped on an aluminum stand as shown in Figure 2.

2.4. Tensile test of carbon nanofiber paper-enabled nanocomposites

The tensile tests were performed using the VARTM manufactured composite laminates with and without carbon nanofiber paper. The tensile tests on the composite beams were conducted according to ASTM test standards. All these tests were performed on a Qualitest testing machine.

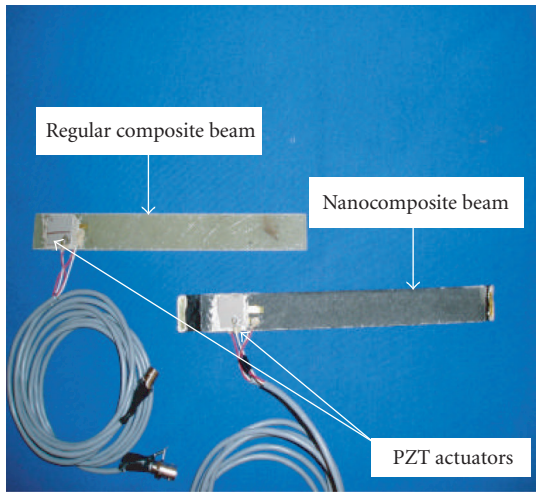

Figure 1: Regular composite beam and nanocomposite beam for damping test.

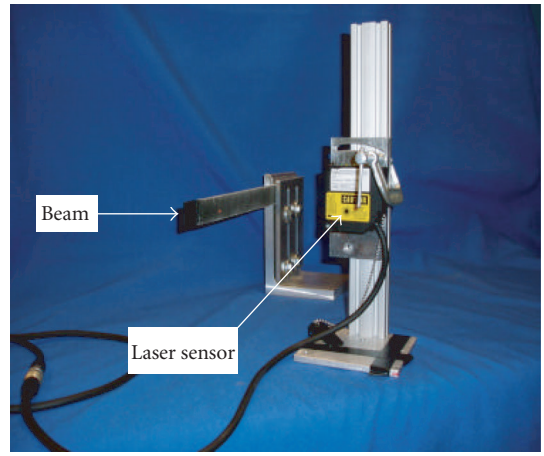

Figure 2: Experimental setup for damping test.

2.5. Electron microscopy

The SEM images were taken to study the porous structure of carbon nanofiber paper and the impregnation of carbon nanofiber paper by the resin. The interface between the carbon nanofiber paper and the resin was examined. The SEM specimens of the nanocomposites were obtained by the ultra microtome cutting.

3. RESULTS AND DISCUSSION

3.1. SEM observations of carbon nanofiber paper and nanocomposites

Figure 3(a) shows the carbon nanofiber paper used in this research, which can be handled like traditional glass fiber mats. The SEM images of carbon nanofiber paper are shown in Figures 3(b) and 3(c). These images show the multiscale porous structure of carbon nanofiber paper formed by short glass fibers and carbon nanofibers. The pore size formed by short glass fibers was in the range of 100–200 μm and the pores formed by carbon nanofibers had an average opening around 1 μm. The carbon nanofibers within the paper have an average diameter about 100–150 nm. Figure 3(d) shows the SEM image of the fracture surface of the nanocomposites embedded with carbon nanofiber paper. This sample was fractured under tensile force. It can be clearly seen that the resin had completely penetrated the carbon nanofiber paper through the thickness direction during the VARTM process.

3.2. Damping properties of carbon nanofiber-enabled composite laminates

The damping test was conducted on the composite laminates with carbon nanofiber paper as midlayer and surface layer. During the damping test, the sweep sinusoidal signals were used as excitation source for the PZT actuator to get the frequency response of the system. Two different sweep sine signals were used for the test. One sweep sine was from 0.1 Hz to 100 Hz to get detailed information about the first mode frequency. The other sweep sine was from 10 Hz to 1000 Hz to excite the first few modes. The sweeping period of both sweep sines was set as 20 seconds. The sampling frequency was set as 40 kHz. For the nanocomposite beam with carbon nanofiber paper as midlayer, the time responses of both sweep sine excitations are shown in Figures 4 and 5, respectively. The peak value in the sweep sine response represents resonance at a certain natural frequency. From the sweep sine responses, it can be clearly seen that the peaks of first mode, second mode, and third mode are significantly reduced for the nanocomposite beam, which indicates that the nanocomposite beam has improved damping property.

To further demonstrate the improved damping for the nanocomposite beam, the frequency responses of the regular composite beam and the nanocomposite beam are compared in Figure 6, which clearly shows that the peak magnitude of the first three modes has dropped dramatically. This means that the damping ratio values of the nanocomposite beam at these three natural frequencies are much larger than those of the regular composite beam.

To estimate the damping ratio for each mode, the half-power bandwidth method was used. Corresponding to each natural frequency, there is a peak in the magnitude-frequency plot of the system. 3 dB down from the peak, there are two points corresponding to half-power point. A larger frequency range between these two points means a larger damping ratio value. The damping ratio is calculated by using the following equation:

$$2\zeta = \frac{\omega_2 - \omega_1}{\omega_n}, \tag{1}$$

where ω_1, ω_1 are the frequencies corresponding to the half-power point, ω_n is the natural frequency corresponding to the peak value, and ζ is the damping ratio. Table 1 shows the first three modal frequencies and associated damping ratio of the two beams. From the damping ratio comparison, it is

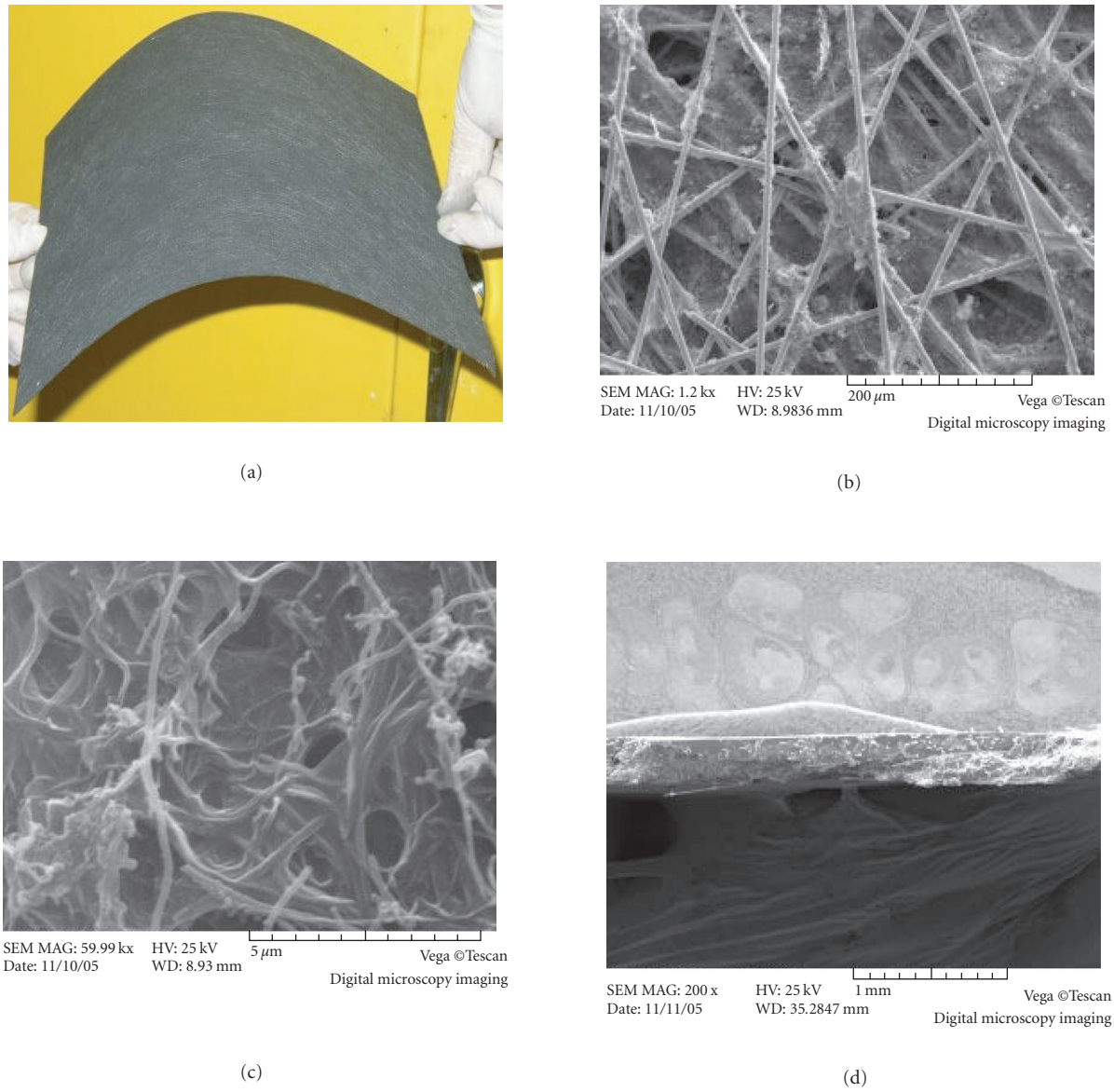

(a) (b) (c) (d)

Figure 3: Carbon nanofiber paper and nanocomposites: (a) carbon nanofiber paper in the dimension of a structural element, (b) the porous structure formed by short glass fiber within the paper, (c) the porous structure formed by carbon nanofibers within the paper, and (d) the fracture surface of the nanocomposites.

clear that the damping ratio of the nanocomposite beam has increased up to 200–700% at the 2nd mode and 3rd mode frequencies. However, there is little change in mode frequencies, which means that there is slight change in the stiffness of the composites. This demonstrates an advantage of nanocomposite over regular composite with viscoelastic layers. The regular composites with viscoelastic layers will sacrifice in reduced stiffness, though damping is improved.

For the nanocomposite beam with carbon nanofiber paper as surface layer, the analysis shows good agreement with the test data for the nanocomposite beam with carbon nanofiber paper as midlayer, as shown in Figure 7. Therefore, it is concluded that the incorporation of carbon nanofiber paper could result in a significant increase in structural damping of conventional fiber reinforced composites.

3.3. *Tensile properties of carbon nanofiber paper-enabled nanocomposites*

As stated earlier, the tensile properties of the composite laminates with and without carbon nanofiber paper were investigated. Table 2 shows the results from the tensile tests performed on the two sets of tensile specimens. It can be seen that the incorporation of carbon nanofiber paper had slight effects on the modulus and the strength of the composite laminates.

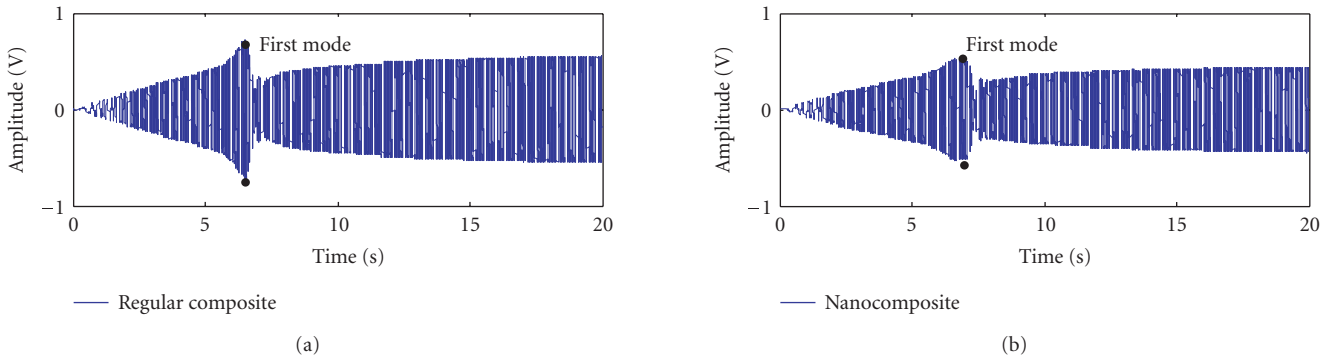

Figure 4: Sweep sine response (0.1 Hz to 100 Hz) of the composite beam without carbon nanofiber paper and the nanocomposite beam with carbon nanofiber paper as midlayer.

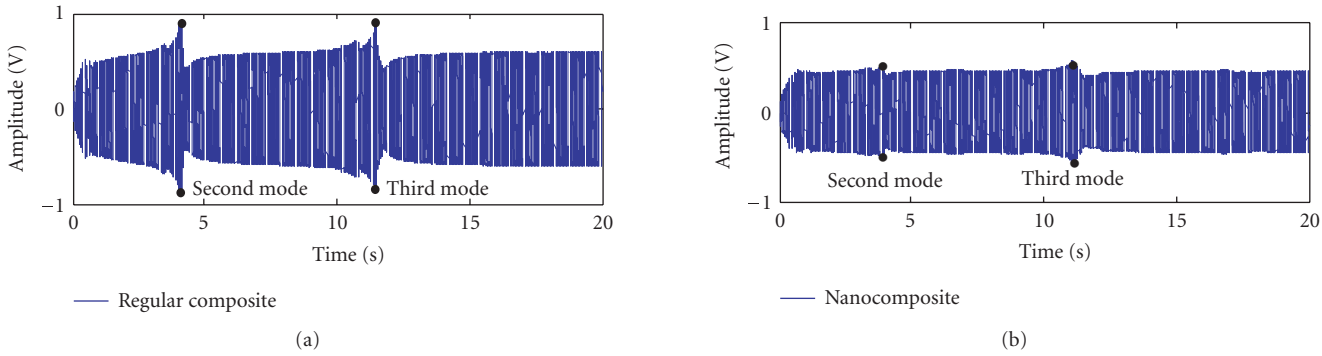

Figure 5: Sweep sine response (10 to 1000 Hz) of the composite beam without carbon nanofiber paper and the nanocomposite beam with carbon nanofiber paper as midlayer.

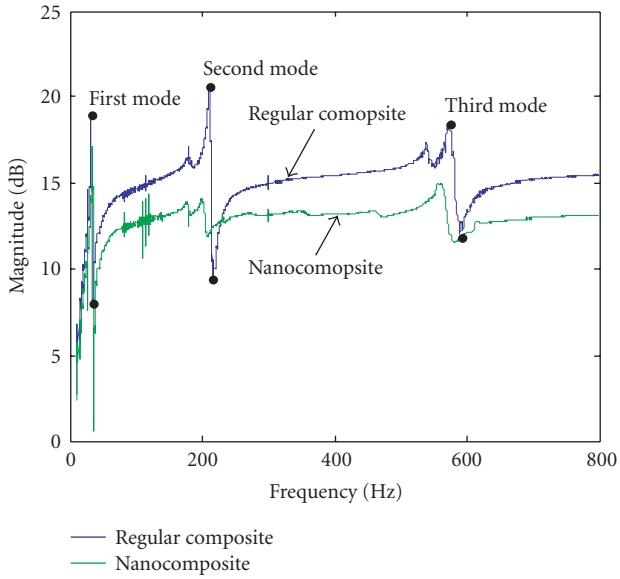

Figure 6: Frequency response of the first three modes for the composite beam without carbon nanofiber paper and the nanocomposite beam with carbon nanofiber paper as midlayer.

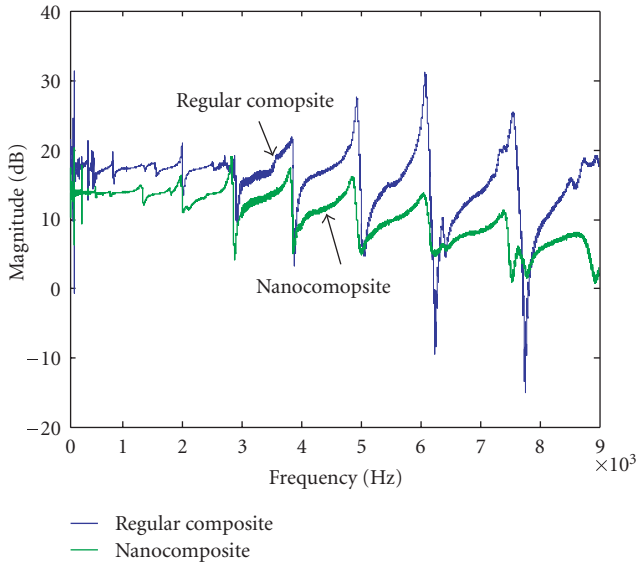

Figure 7: Frequency response of the first three modes for the composite beam without carbon nanofiber paper and the nanocomposite beam with carbon nanofiber paper as surface layer.

Table 1: Damping ratio calculated by half-power bandwidth method.

	1st mode frequency (Hz)	1st mode damping ratio	2nd mode frequency (Hz)	2nd mode damping ratio	3rd mode frequency (Hz)	3rd mode damping ratio
Regular composite beam	31.93	0.0278	210.8	0.0251	572.5	0.0349
Nanocomposite beam	34.60	0.0373	198.5	0.1985	558	0.1104

Table 2: Results from the tensile tests performed on the laminates with/without carbon nanofiber paper.

	Test specimens	Average thickness (inch)	Average width (inch)	Average length (inch)	Tensile modulus (ksi)	Tensile strength (ksi)
1	Laminates without carbon nanofiber paper	0.10	0.75	5.75	1,220	25.7
2	Laminates with carbon nanofiber paper as midlayer	0.15	0.96	5.75	1,120	24.5
3	Laminates with carbon nanofiber paper as surface layer	0.10	0.75	6.25	1,300	24.1

4. CONCLUSIONS

This paper presented the damping tests conducted using the nanocomposite beams with an embedded carbon nanofiber paper as interlayer or surface layer. The composite laminates without carbon nanofiber paper were also tested. The tests indicated up to 200–700% increase of the damping ratios at higher frequencies and slight change in tensile strength and Young's modulus of composite laminates due to the incorporation of carbon nanofiber paper. The SEM characterization of the carbon nanofiber paper and the nanocomposites showed the entanglement of carbon nanofibers and short glass fibers within the carbon nanofiber paper and the complete penetration of the resin through the carbon nanofiber paper. These cross-linkages within the carbon nanofiber paper are expected to be responsible for the energy dissipation in the nanocomposites due to the strong bonding and nonbonding interactions between carbon nanofibers and short glass fibers.

ACKNOWLEDGMENTS

The authors would like to acknowledge the financial support provided by the University of South Alabama Research Council (USARC Grant no. 3–61619) and National Science Foundation (CAREER Grant no. 0093737). The assistance by Dr. Kendall Clarke and Mr. Steven Sumerlin is gratefully acknowledged.

REFERENCES

[1] O. Breuer and U. Sundararaj, "Big returns from small fibers: a review of polymer/carbon nanotube composites," *Polymer Composites*, vol. 25, no. 6, pp. 630–645, 2004.

[2] E. T. Thostenson, Z. Ren, and T.-W. Chou, "Advances in the science and technology of carbon nanotubes and their composites: a review," *Composites Science and Technology*, vol. 61, no. 13, pp. 1899–1912, 2001.

[3] K.-T. Lau and D. Hui, "The revolutionary creation of new advanced materials—carbon nanotube composites," *Composites Part B: Engineering*, vol. 33, no. 4, pp. 263–277, 2002.

[4] F. H. Gojny, M. H. G. Wichmann, B. Fiedler, W. Bauhofer, and K. Schulte, "Influence of nano-modification on the mechanical and electrical properties of conventional fibre-reinforced composites," *Composites Part A: Applied Science and Manufacturing*, vol. 36, no. 11, pp. 1525–1535, 2005.

[5] F. H. Gojny, M. H. G. Wichmann, U. Köpke, B. Fiedler, and K. Schulte, "Carbon nanotube-reinforced epoxy-composites: enhanced stiffness and fracture toughness at low nanotube content," *Composites Science and Technology*, vol. 64, no. 15, pp. 2363–2371, 2004.

[6] D. Qian, E. C. Dickey, R. Andrews, and T. Rantell, "Load transfer and deformation mechanisms in carbon nanotube-polystyrene composites," *Applied Physics Letters*, vol. 76, no. 20, pp. 2868–2870, 2000.

[7] L. S. Schadler, S. C. Giannaris, and P. M. Ajayan, "Load transfer in carbon nanotube epoxy composites," *Applied Physics Letters*, vol. 73, no. 26, pp. 3842–3844, 1998.

[8] H. Ma, J. Zeng, M. L. Realff, S. Kumar, and D. A. Schiraldi, "Processing, structure, and properties of fibers from polyester/carbon nanofiber composites," *Composites Science and Technology*, vol. 63, no. 11, pp. 1617–1628, 2003.

[9] C. Bower, R. Rosen, L. Jin, J. Han, and O. Zhou, "Deformation of carbon nanotubes in nanotube-polymer composites," *Applied Physics Letters*, vol. 74, no. 22, pp. 3317–3319, 1999.

[10] Z. Ounaies, C. Park, K. E. Wise, E. J. Siochi, and J. S. Harrison, "Electrical properties of single wall carbon nanotube reinforced polyimide composites," *Composites Science and Technology*, vol. 63, no. 11, pp. 1637–1646, 2003.

[11] J. Sandler, M. S. P. Shaffer, T. Prasse, W. Bauhofer, K. Schulte, and A. H. Windle, "Development of a dispersion process for carbon nanotubes in an epoxy matrix and the resulting electrical properties," *Polymer*, vol. 40, no. 21, pp. 5967–5971, 1999.

[12] S. J. Park, S. T. Lim, M. S. Cho, H. M. Kim, J. Joo, and H. J. Choi, "Electrical properties of multi-walled carbon nanotube/poly(methyl methacrylate) nanocomposite," *Current Applied Physics*, vol. 5, no. 4, pp. 302–304, 2005.

[13] T. Kashiwagi, E. Grulke, J. Hilding, et al., "Thermal and flammability properties of polypropylene/carbon nanotube nanocomposites," *Polymer*, vol. 45, no. 12, pp. 4227–4239, 2004.

[14] S. Peeterbroeck, M. Alexandre, J. B. Nagy, et al., "Polymer-layered silicate-carbon nanotube nanocomposites: unique nanofiller synergistic effect," *Composites Science and Technology*, vol. 64, no. 15, pp. 2317–2323, 2004.

[15] W. H. Liao and K. W. Wang, "On the analysis of viscoelastic materials for active constrained layer damping treatments," *Journal of Sound and Vibration*, vol. 207, no. 3, pp. 319–334, 1997.

[16] H. Kishi, M. Kuwata, S. Matsuda, T. Asami, and A. Murakami, "Damping properties of thermoplastic-elastomer interleaved carbon fiber-reinforced epoxy composites," *Composites Science and Technology*, vol. 64, no. 16, pp. 2517–2523, 2004.

[17] W. Pulliam, D. Lee, G. Carman, and G. McKnight, "Thin-layer magnetostrictive composite films for turbomachinery fan blade damping," in *Smart Structures and Materials 2003: Industrial and Commercial Applications of Smart Structures Technologies*, vol. 5054 of *Proceedings of SPIE - The International Society for Optical Engineering*, pp. 360–371, San Diego, Calif, USA, March 2003.

[18] J. Suhr, N. A. Koratkar, P. Keblinski, and P. Ajayan, "Viscoelasticity in carbon nanotube composites," *Nature Materials*, vol. 4, no. 2, pp. 134–137, 2005.

[19] N. A. Koratkar, B. Wei, and P. M. Ajayan, "Multifunctional structural reinforcement featuring carbon nanotube films," *Composites Science and Technology*, vol. 63, no. 11, pp. 1525–1531, 2003.

[20] N. A. Koratkar, B. Wei, and P. M. Ajayan, "Carbon nanotube films for damping applications," *Advanced Materials*, vol. 14, no. 13-14, pp. 997–1000, 2002.

[21] J. Gou, B. Minaie, B. Wang, Z. Liang, and C. Zhang, "Computational and experimental study of interfacial bonding of single-walled nanotube reinforced composites," *Computational Materials Science*, vol. 31, no. 3-4, pp. 225–236, 2004.

[22] Z. Wang, Z. Liang, B. Wang, C. Zhang, and L. Kramer, "Processing and property investigation of single-walled carbon nanotube (SWNT) buckypaper/epoxy resin matrix nanocomposites," *Composites Part A: Applied Science and Manufacturing*, vol. 35, no. 10, pp. 1225–1232, 2004.

[23] J. Gou, Z. Liang, and B. Wang, "Experimental design and optimization of dispersion process for single-walled carbon nanotube bucky paper," *International Journal of Nanoscience*, vol. 3, no. 3, pp. 293–307, 2004.

Hindawi Publishing Corporation
Journal of Nanomaterials
Volume 2006, Article ID 29139, Pages 1–2
DOI 10.1155/JNM/2006/29139

Control Effect of Nanometer SiO_2 Hydrosol on Alloy Impurity in CMP Process of ULSI

Liu Yuling, Li Weiwei, Zhang Xihui, and Liu Changyu

School of Information and Engineering, Hebei University of Technology, 8 Guangrong Road, Hongqiao District, Tianjin 300130, China

Received 26 December 2005; Accepted 12 November 2006

This article analyzed and studied the concentration mechanism of metal impurities of ULSI multilayered wiring CMP in the special-purpose nanometer SiO_2 grinding compound in the substrate chip surface and the process of purification with chelating agent; we also obtained the remarkable effect and the effective application in the microelectron component preparation.

1. INTRODUCTION

With the development of microelectronic technology, the characteristic size entered the 65 nm and wiring layer already achieved above ten, in the really large-scale integrated circuit (ULSI). Each layer has to carry on globle planarization for photoetching effect and product rate. The only best method of planarization is chemical mechanic planarization (CMP) [1–4], whose mechanical effects depend on some fixed factors such as polishing pad, rotary speed, and polishing pressure. The key is the abrasive in polishing process; SiO_2 colloid is the best abrasive among existing abrasives because of its high purification and broad appliance. The increasing sensitivity of devices is affected by the metal impurities that would cause big leakage electric current, low penetration, soft penetration, reliability deterioration, and undesirable influence. It has suppressed the development of microelectronic technology and the widespread application. Therefore, to obtain the high performance devices, the superficial impurity must fall below the harmful value. Substrate surface metal reduces a magnitude every ten years, along with the microelectron development. The ULSI substrate surface metal relies intensely on the metal impurities density in the solution environment. At present, the metal impurities degree must be cut down behind ppt level (m/Si = 10–12). This research has analyzed the gathering process of copper contaminations. Meanwhile, the control of adsorption states using chelant has also been studied deeply.

2. EXPERIMENT

2.1. Experiment of metal impurity adsorption on ULSI substrate

In new processing surface of the ULSI substrate chip and the multilayered wiring CMP, there are a lot of hanging bonds that cause strong superficial field. Metal impurities have a very strong adsorption function on surface. Copper that has harmful effect on device is an example.

2.1.1. Experiment and result

Respectively, we use the polishing slurry to carry on CMP on the substrate chip under the condition that copper content is 60 ppb and 23 ppb, particle size is 30–40 nm, the density is 20 wt%, PH value is 10.3. After the DI water cleans polishing the chip, it is examined with the graphite stove atom absorption spectrum (GFAAS). And the results are in Table 1.

Seen from Table 1, Cu content of the new processing ULSI surface with CMP is dozens of times more than the metallic ion of the SiO_2 colloid. From that it can be seen that the new processed surface has strong function of enrichment function to metallic ions.

2.2. The adsorption experiment of control copper after joining the chelating agent to the ULSI special-purpose SiO_2 polishing slurry

Experiments have indicated that the content of copper on wafer surface has been improved greatly after CMP using

Table 1

Sort	Number			
	250902	250904	250803	250807
Cu (ppb) SiO_2colloid	23	61	23	62
Cu (ppb) in ULSI substrate surface	1800	2060	1780	2070

Table 2

The chelating agent	PPA	AMPS	DTPMP	DTMPA
Cu (ppb) after CMP	15.35	9.67	1.44	8.39

purified SiO_2 as abrasive. Only reduction of metal content in slurry is far from satisfactory if metal impurity must be removed from wafer surface, because it cannot realize purification of metal impurities in polishing slurry through present technology and the vanishment of the micrometal impurities absolutely. Moreover, the processing procedure and the environment can cause contamination. We will adopt a kind of chelant to transform the metal impurities to stable complexants. So easily cleaning can be kept because chemisorption cannot form on new surface [4–10].

2.2.1. Experiment and result

(1) Silicon wafer (100) N-type, electronic resistivity 8–14 $\Omega \cdot$ cm.
(2) SiO_2 polishing slurry: particle size 30–40 nm, the density 20 wt%, and PH = 10.3 Cu content 100 ppb.
(3) In the above polishing fluid joining 0.1 wt% chelating agent, respectively: polyacrylic acid (PPA), acrylic amides sulfonate copolymer (AMPS), divinyl three amines five methylenes phosphoric acid (DTPMP), and second grade two-alkene three amines four methylenes phosphoric acid (DTMPA).

The silicon wafer was carried on CMP for 20 min; the result was examined by graphite stove atom absorption spectrum (GFAAS) to determine. The results are in Table 2.

Results show that metal impurities are reduced remarkably by adding polishing fluid with the chelating agent after CMP.

2.2.2. Experimental result and analysis

In the ULSI preparation, controlling of metal impurities on substrate and ULSI multilayered wiring CMP wafer is the essential microelectronic technology that needs further resolve. A large number of coppers enriched because there are a lot of hanging bonds on new processing surface. Moreover, the copper is behind the silicon in chemistry activity sequence chart; thus the copper in the silicon substrate surface can get up the redox reaction:

$$2Cu^{2+} + Si \longrightarrow Si^{4+} + 2Cu \downarrow, \quad (1)$$

copper atoms resulting from chemical reaction absorbed on silicon substrate. Density balance is destroyed because of the reduction of copper ions on solid surface, which causes the copper diffusion from liquid to surface. The diffusion causes the superficial cupric ion to respond with the silicon; after response, the ion reduces again in the surface, and the liquid diffuses to the surface, goes round and round; the copper density on new surface is more than that in the polishing slurry; in this environment, the copper ion gathers on the silicon substrate surface. If joining the chelant, after the copper ion and the chelant form the extremely stable chelate, the redox reaction is hard to carry on. The chelant ion is very big after complex. There is only the very weak vander waal strength to physisorption in the silicon substrate surface; the cupric ion is cleaned easily from the surface. Therefore, in order to meet with the electronic technology rapid development, chelant can be used to reduce metal contamination besides purifying of polishing slurry. In the substrate and in the multilayered wiring CMP processing process, besides effectively purifying the density of the CMP polishing fluid, at the same time, joining the chelating agent to the polishing fluid is a extremely effective method of reducing the surface metal impurities in the ULSI preparation process.

REFERENCES

[1] J. J. Vlassak, "A model for chemical-mechanical polishing of a material surface based on contact mechanics," *Journal of the Mechanics and Physics of Solids*, vol. 52, no. 4, pp. 847–873, 2004.

[2] L. Yuling, T. Baimei, and Z. Kailiang, *Performance and Test Technical Engineer of ULSI Substrate*, Metallurgical Industry Press, Beijing, China, 2002.

[3] L. Yuling, T. Baimei, and Z. Kailiang, *Microelectronics Technical Engineer, Material, Technology, and Test*, Electronics Industry Press, Beijing, China, 2004.

[4] L. Yuling, L. Weiwei, and Z. Jianwei, *Microelectronics Chemical Technology*, Chemical Industry Press, Beijing, China, 2005.

[5] X. G. Zhang, *Electrochemistry of Silicon and Its Oxide*, Kluwer Academic/Plenum, New York, NY, USA, 2001.

[6] V. Gorodokin and D. Zemlyanov, "Metallic contamination in silicon processing," in *Proceedings of the 23rd IEEE Convention of Electrical and Electronics Engineers in Israel*, pp. 157–160, Tel-Aviv, Israel, September 2004.

[7] E. Hsu, H. G. Parks, R. Craigin, S. Tomooka, J. S. Ramberg, and R. K. Lowry, "Deposition characteristics of metal cintaminants from HF-dased process solutions onto solicon wafer suiface," *Journal of the Electrochemical Society*, vol. 139, no. 12, pp. 3659–3664, 1992.

[8] S. W. Lim, R. T. Mo, P. A. Pianetta, and C. E. D. Chidsey, "Effect of silicon surface termination on copper deposition in deionized water," *Journal of the Electrochemical Society*, vol. 148, no. 1, pp. C16–C20, 2001.

[9] L. Yuling, L. Na, and C. Yang, "Investigation on adsorption state of surface adsorbate on silicon wafer," *Rare Metals*, vol. 18, no. 2, pp. 106–112, 1999.

[10] L. Yuling, G. Haiyun, and T. Baimei, "Present situations and prospects of cleaning in ULSI," *Chinese Journal of Rare Metals*, vol. 25, no. 2, pp. 134–138, 2001.

Hindawi Publishing Corporation
Journal of Nanomaterials
Volume 2006, Article ID 76371, Pages 1–10
DOI 10.1155/JNM/2006/76371

Silica-Polystyrene Nanocomposite Particles Synthesized by Nitroxide-Mediated Polymerization and Their Encapsulation through Miniemulsion Polymerization

Bérangère Bailly,[1,2] Anne-Carole Donnenwirth,[1,2] Christèle Bartholome,[1,2] Emmanuel Beyou,[1] and Elodie Bourgeat-Lami[2]

[1] *Ingénierie des Matériaux Polymères (IMP), Laboratoire des Matériaux Polymères et des Biomatériaux (LMPB), Université de Lyon 1, Université de Lyon, 69003 Villeurbanne Cedex, France*
[2] *Laboratoire de Chimie et Procédés de Polymérisation (LCPP), École Supérieure Chimie Physique Electronique de Lyon (CPE), Université de Lyon 1, Université de Lyon, Bâtiment F308, BP 2077, 43 Boulevard du 11 Novembre 1918, 69616 Villeurbanne Cedex, France*

Received 2 February 2006; Revised 9 November 2006; Accepted 21 November 2006

Polystyrene (PS) chains with molecular weights comprised between 8000 and 64000 $g \cdot mol^{-1}$ and narrow polydispersities were grown from the surface of silica nanoparticles (Aerosil A200 fumed silica and Stöber silica, resp.) through nitroxide-mediated polymerization (NMP). Alkoxyamine initiators based on N-tert-butyl-1-diethylphosphono-2,2-dimethylpropyl nitroxide (DEPN) and carrying a terminal functional group have been synthesized in situ and grafted to the silica surface. The resulting grafted alkoxyamines have been employed to initiate the growth of polystyrene chains from the inorganic surface. The maximum grafting density of the surface-tethered PS chains was estimated and seemed to be limited by initiator confinement at the interface. Then, the PS-grafted Stöber silica nanoparticles were entrapped inside latex particles via miniemulsion polymerization. Transmission electron microscopy indicated the successful formation of silica-polystyrene core-shell particles.

1. INTRODUCTION

A key issue in the elaboration of organic/inorganic hybrids and nanocomposites is the creation of specific interactions at the interface of the organic and inorganic components. Among the large palette of existing techniques, living polymerizations offer versatile ways to engineer inorganic particle surfaces. Controlled radical polymerization allows the synthesis of polymers with various architectures (statistical copolymers, block copolymers, star polymers, etc.) with good control over the molecular weight and molecular weight distribution (polydispersities are typically less than 1.2-1.3). This chemistry was recently extrapolated to nanoparticles functionalization in order to elaborate well-defined nanocomposites which can be grown with the desired thickness and composition [1–12]. Recently, Parvole et al. [9], Kasseh et al. [7], and the authors et al. [10–12] have demonstrated that NMP is well adapted to the grafting of polymers from the surface of silica either in bulk or in solution. In these papers, various surface-immobilized initiators have been investigated to control the polymerization reaction. These initiators were based either on unimolecular alkoxyamines carrying trichlorosilyl or triethoxysilyl endgroups for further attachment on the silica surface [10–13] or on bimolecular systems based on the strategy of Rühe in which the NMP process is initiated from surface-immobilized azo or peroxide initiators [7, 9]. In most of these works, the resulting polymer-grafted silica particles were dispersed further into a polymer matrix by mechanical blending at high temperature or by lyophilization of the suspension mixture. However, to date, very little work has been devoted to the incorporation of polymer-grafted mineral particles into water borne polymers using for instance the miniemulsion polymerization technique although the later has found an increasing interest in recent literature [14–17]. Indeed, in miniemulsion, polymerization mainly occurs into small monomer droplets stabilized by the addition of a surfactant and a costabilizer. The polymer particles are thus the copy of the miniemulsion droplets. Therefore, if mineral particles can be successfully dispersed into the nanodroplets,

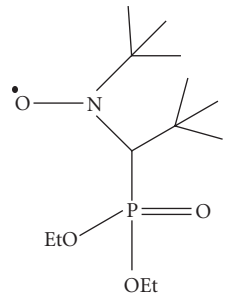

Structure 1: DEPN.

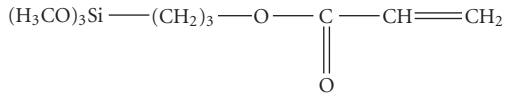

Structure 2: APTMS.

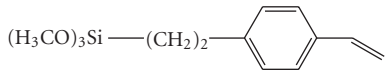

Structure 3: VETMSB.

composite particles made of for instance silica particles surrounded by a polymer shell will be obtained after polymerization.

Herein, we report two synthetic strategies in order to grow polystyrene chains from the surface of fumed silica (route I) and Stöber silica particles (route II), respectively using nitroxide-mediated polymerization. In the first route, the surface-alkoxyamine initiator was produced in a one step process by reacting simultaneously DEPN (Structure 1), AIBN, and acryloxy propyl trimethoxy silane (APTMS, Structure 2). The alkoxyamine was formed *in situ* by trapping of the acryloxy radicals produced by reaction of AIBN with APTMS and grafting of the resulting product onto silica according to the procedure previously described [12]. In the second route, a styrenic silane coupling agent (VETMSB, Structure 3) was first grafted onto the silica particles in a mixture of ethanol and water. Grafting of the alkoxyamine initiator was then performed by reacting styryl-DEPN (Structure 4) with the VETMSB-grafted silica in dimethylformamide (Scheme 1). The NMP of styrene from the grafted alkoxyamine silicas was performed in toluene for route I and in DMF for route II as this last solvent enabled us to maintain the silica particles colloidally stable all along during polymerization. In order to attest for the livingness of the free radical polymerization process, the monomer conversion, the polymer molecular weights and molecular weight distributions were analyzed as a function of

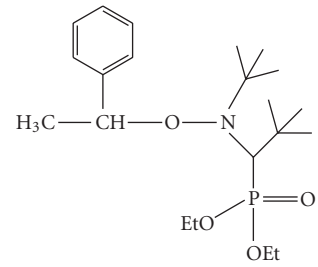

Structure 4: Styryl-DEPN.

time. The amount of grafted polymer chains was quantified and the bulk and surface compositions were compared for the two systems. In addition, dynamic light scattering (DLS) measurements and transmission electron microscopy (TEM) analysis were performed on the PS-grafted silica suspensions in order to examine the influence of the polymer molecular weight and the extent of grafting on the properties of the composite particles. At last, the polystyrene-grafted colloidal silicas were suspended into styrene and the resulting organic suspension was poured into water, emulsified and polymerized through miniemulsion in order to examine whether the silica particles could be encapsulated by polystyrene following this strategy.

2. EXPERIMENTAL PART

2.1. Materials

Fumed silica (Aerosil A200V, Degussa) with an average diameter of 13 nm and a specific surface area of 228 m^2/g was dried four hours at 150°C under a vacuum before use. Styrene (99%, Aldrich), dimethylformamide (99%, Aldrich) and toluene (99.3%, Aldrich) were vacuum distilled on molecular sieve before use. Azobisisobutyronitrile (AIBN, 98%, Acros Organics) was recrystallized from methanol. Tetraethoxysilane (TEOS, Acros Organics), ethyl alcohol (Acros Organics), ammonia (29% in water, Carlo Erba), acryloxy propyl trimethoxy silane (APTMS, 95%, Gelest), and *p*-vinyl(ethyltrimethoxysilane) benzene (VETMSB, Structure 3, Acros Organics, 99%) were used as supplied. DEPN (88%) was kindly supplied by Atofina, and used as received. The free initiator, a DEPN-based alkoxyamine (styryl-DEPN, Structure 4), was prepared using a procedure described in the literature [18]. The initiator, potassium persulfate (KPS, Aldrich), cetyl alcohol (Aldrich), and sodium dodecyl sulfate (SDS, Aldrich) were of analytical grade and used as received.

2.2. Synthesis of the Stöber colloidal silica suspension

Monodisperse silica particles were synthesized in two steps. First, a silica seed suspension was prepared by introducing

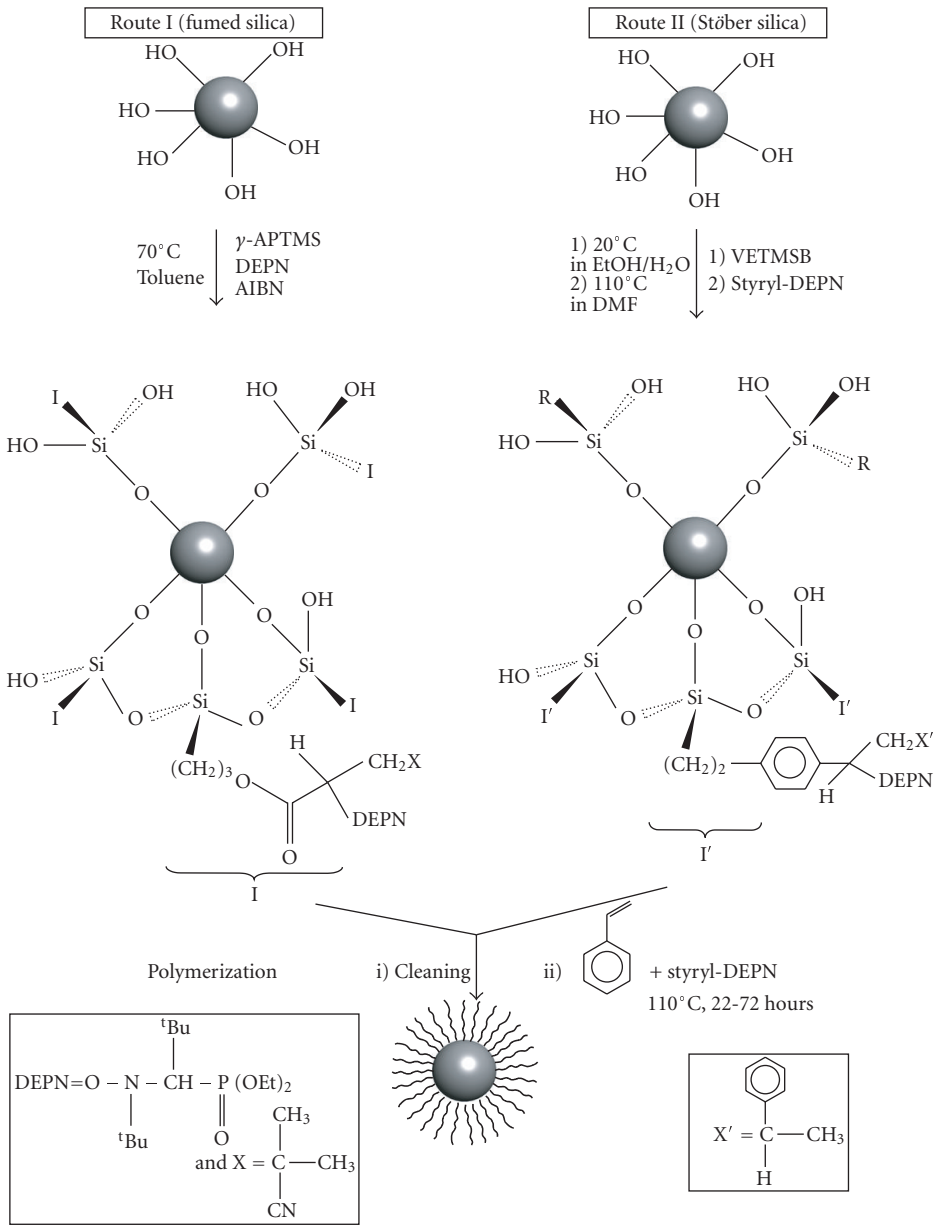

Scheme 1: Chemical routes to polystyrene-decorated silica nanoparticles by nitroxide-mediated polymerization of styrene. Fumed silica are involved in the first route while Stöber silica particles have been employed in the second route.

41.6 g of TEOS in a mixture of absolute ethanol (667.8 g), water (101.3 g) and ammonia (8.4 g) according to the procedure first described by Stöber et al. [19]. The mixture was stirred for 24 hours at room temperature and yielded silica particles with an average diameter of 61.3 nm and a 1.8 wt% solid content. Seeded growth of the silica suspension was then performed by the addition of a solution of TEOS (96 g) in ethanol (113.5 g) at the rate of 20 mL per hour and stirring for 48 hours. The final suspension had an average particle diameter of 79.7 nm determined by DLS and a solid content of 5.4 wt%. Figure 1 shows the TEM image of the thus produced silica particles.

2.3. *Initiator attachment on the silica surface and stable free radical polymerization of styrene from the functionalized silica surface*

The graft polymerization of styrene from the surface of silica involves two steps (Scheme 1): (i) in situ grafting of a triethoxysilyl-terminated alkoxyamine initiator [12], and (ii) controlled growth of polystyrene chains from the silica surface in the presence of free alkoxyamine initiator. In the first route, 1.22 g of the APTMS coupling agent (5.2 mmoles corresponding to 12 μmol/m^2 of silica) was added to a suspension of silica (1.9 g) in toluene (93 g) and stirred for 30

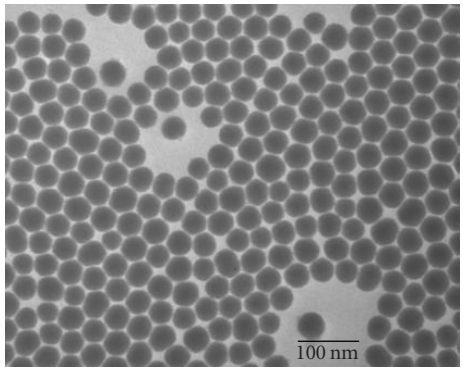

Figure 1: TEM image of the Stöber silica sample. Scale bar=100 nm.

minutes at room temperature. Then, 1.1 g of **3** (corresponding to 3.65 mmoles) and 0.4 g of AIBN (2.6 mmoles) were introduced in the reaction flask. The suspension was degassed by 4 freeze-pump-thaws, and the mixture was heated to 70°C for 26 hours. The grafted silica was extensively washed by successive centrifugation/redispersions in toluene in order to remove the excess reagents before characterization. The nitroxide-mediated polymerization experiments were then conducted as follows. The alkoxyamine-functionalized silica (0.3 g), toluene (57.3 g, 0.62 mol), styrene (60.4 g, 0.58 mol), and 0.2 g (0.68 mmol) of the "free" alkoxyamine initiator (styryl-DEPN, Structure 4), corresponding to a total styrene-to-initiator molar ratio of 800, were introduced in a predried Schlenk flask under an argon atmosphere. After stirring for a few minutes, the suspension was degassed by 4 freeze-pump-thaw cycles, and the polymerization mixture was heated to 110°C for 5 to 30 hours. The conversions were determined gravimetrically by precipitation in methanol. The free nongrafted polystyrene was removed from the silica suspension by successive centrifugation/redispersion cycles in toluene. The polymer grafting density was then determined by carbon elemental analysis as described in our previous work [10–12].

In the second route, 2.8 g of VETMSB (11 mmoles or 5.5 μmoles/m^2) was first added to a suspension of silica (48.2 g) in EtOH/H_2O 50/50 v/v (1058 g) and stirred for 78 hours at room temperature. The free nongrafted VETMSB was discarded by successive centrifugation/redispersion cycles. A small part of the grafted silica powder was dried in a vacuum oven at 50°C before characterization while the remaining part (2.24 g) was redispersed in DMF (80.6 g, 1.1 mol). The surface alkoxyamine was then formed *in situ* by introducing 0.32 g (0.80 mmol, 8.5 μmol/m^2) of styryl-DEPN (Structure 4) in a predried Schlenk flask under an argon atmosphere. The suspension was degassed by 4 freeze-pump-thaw cycles and heated to 110°C for 72 hours. The graft-from polymerization was pursued in the same reactor by adding 66.5 g of styrene (0.64 mol) corresponding to a total styrene-to-initiator molar ratio of 800. After stirring for a few minutes, the suspension was degassed by 4 freeze-pump-thaw cycles, and the polymerization mixture was heated to 110°C for 5 to 30 hours. The conversions were determined as described above for route I while the free nongrafted polystyrene was removed from the silica suspension by successive centrifugation/redispersion cycles in DMF.

2.3.1. Synthesis of silica-polystyrene core-shell particles through miniemulsion polymerization

The PS-grafted Stöber silica (1.5 g) was dispersed into 15 g of styrene and the resulting suspension was introduced into 150 g of an aqueous solution containing the surfactant (SDS, 0.45 g) and the hydrophobe (cetyl alcohol, 1.2 g). The overall mixture was finally sonified for 1 minute (90% output power) to create the silica-loaded miniemulsion droplets. The polymerization was carried out in a double-wall thermostated reactor at 70°C for 5 hours. The reactor was first purged with nitrogen for 1 hour and potassium persulfate (0.15 g) was used as initiator to start polymerization. The silica, droplet, and composite particles number per unit volume of water was calculated by the following equation:

$$\frac{N_p}{L} = \frac{M/\rho}{(\pi/6)Dp^3 \cdot V} \times 10^{19}, \tag{1}$$

where M (g) is the total mass of silica or silica plus monomer, ρ(g·cm^{-3}) is the particles or droplets density, Dp (nm) is, respectively, the diameter of the silica, the monomer droplets or the composite latex particles determined by DLS, and V (in liter) is the total volume of water.

2.3.2. Characterizations

SEC analysis was performed using a 410 Waters differential refractometer, a 996 Waters photodiode array detector, a 717 Waters autosampler, and a 515 Waters HPLC pump. THF was used as eluent. Polymer molecular weights were derived from a calibration curve based on polystyrene standards. The initiators and polymer grafting densities were determined by elemental analysis from the difference of carbon content (ΔC, wt%) after and before grafting, using (2) below:

$$\text{Grafting density } (\mu\text{mol/m}^2) = \frac{10^6 \Delta C}{[(1200Nc\text{-}\Delta C(M\text{-}1)) \times S_{spec}]}, \tag{2}$$

where Nc and M designate, respectively, the number of carbon atoms and the molecular weight of the grafted molecule, and S_{spec}(m^2·g^{-1}) is the specific surface area of silica.

TEM analysis was performed on a Philips CM10 electron microscope operating at 80 kV. In a typical experiment, one drop of the colloidal dispersion was put on a carbon film supported by a copper grid and allowed to air dry before observation. The particle and droplet sizes were determined by DLS using a Malvern autosizer Lo-c apparatus with a detection angle of 90°. The measurements were carried out at 23°C on highly diluted samples in order to rule out interaction and multiple scattering effects. The intensity average diameter was computed from the intensity autocorrelation data using the cumulant analysis method.

Table 1: Polymer grafting densities for a series of "graft-from" polymerization reactions performed in the presence of fumed silica (route I) and Stöber silica (route II), respectively.

Route	Run	Styrene/Initiator (molar ratio)[(b)]	Time (h)	Conversion (%)	Mn_{th} (g/mol)[(c)]	Grafting density[(d)]	Free polymer in solution	
							Mn (g/mol)	Mw/Mn
I[(a)]	**1**	800	22	33	27490	0.33	30700	1.22
	2	800	54	63	52416	0.32	55500	1.20
II[(a)]	**3**	800	30	38	31616	0.10	64000	1.45
	4	400	30	68	28288	0.14	37000	1.34

[(a)]The alkoxyamine grafting density is of approximately 0.75 μmol/m^2 for route I and 2 μmol/m^2 for route II.
[(b)]Initiator = surface-grafted initiator + free initiator.
[(c)]$Mn_{th} = ([M]_0/[I]_0) \times$ Mw of styrene $\times$ conv/100.
[(d)]Determined by carbon elemental analysis using (2) and the molecular weight of the free polymer in solution.

3. RESULTS AND DISCUSSION

3.1. Initiator immobilization

Grafting of the alkoxyamine initiators on the silica surface was qualitatively evidenced by FTIR and solid state NMR spectroscopies which attested for covalent attachment of the silane coupling agents [11, 12]. The density of the initiator units, determined by carbon elemental analysis, was around 0.75 μmol/m^2 in the case of route I [12] which value is from two to three times lower than the values given in the literature for the grafting of a series of organotrialkoxysilane and chlorosilane molecules [5]. In our experiments, approximately 12.5% of the original amount of silanol groups had reacted, which suggests the occurrence of steric hindrance limitations and physisorption of the DEPN moiety onto the silanol groups of silica during the grafting reaction. In the second route, the grafting density of VETMSB on the Stöber silica surface was also calculated from carbon elemental analysis using (2). It was found that around 5 μmol/m^2 of the silane coupling agent were grafted onto silica which value excluded the possibility of the formation of a single monolayer. Indeed, VETMSB molecules can condense with one another before condensing on the silica surface and form multilayers of VETMSB molecules as described in the literature for trimethoxysilyl-terminated silane coupling agents [8, 20–22]. After the grafting of VETMSB on the silica surface, we performed the insertion of Styryl-DEPN to create an alkoxyamine by *in situ* trapping of carbon radicals. This reaction was conducted in dimethylformamide at 110°C. The amount of the resulting grafted alkoxyamine was determined again by carbon elemental analysis. The grafting density calculated from (2) is around 2 μmol/m^2. This result is in good agreement with the grafting density (2.4 μmol/m^2) reported by Von Werne and Patten [2] for the grafting of an ATRP initiator but is twice higher than the value given in the literature for *in situ* grafting of alkoxyamine initiators [8, 9]. It is likely that some physisorption may also occur here together with the coupling reaction. In addition, DLS measurements revealed that the initiator-coated silica particles were perfectly dispersed in DMF as their diameter remained almost unchanged after grafting.

3.2. Surface initiated polymerization

The polymerizations were conducted in a 50/50 (v/v) styrene/toluene solution for route I and in a 50/50 (v/v) styrene/DMF solution for route II in the presence of 1 wt% of silica and a known amount of "free" sacrificial initiator. The addition of "free" alkoxyamine creates an overall concentration of nitroxide in the polymerization mixture, which controls the chain growth of both the immobilized and soluble initiators, and allows one to achieve a good molecular weight control. According to previous studies [1, 2, 8, 10–12, 23–25], it can be reasonably assumed that the molecular weight of the free polymer chains is similar to that of the grafted polymer. Thus, the "living" character of the polymerization reaction can be assessed by following the molar mass and the polydispersity indexes of the free polymer only.

For route I, the data in Table 1 indicates a good agreement between the experimental molecular weights and the theoretical ones as expected for a controlled polymerization reaction. This result suggests that steric constraints around silica particles have no influence on the livingness of the free radical process. Moreover, a maximum polymer grafting density (determined from the molecular weight, Mn, of the free polymer in solution) of around 0.32 μmol/m^2 was achieved under optimal conditions whatever the polymer molecular weight comprised between 30000 and 60000 g·mol^{-1}. From this data, we can calculate that approximately 40% of the grafted alkoxyamine underwent polymerization which value is in close agreement with the data reported by Böttcher et al. [5] or Kasseh et al. [7] on silica nanoparticles. However, this value is inconsistent with the observed agreement between the theoretical and the experimental molecular weights (runs 1 and 2 in Table 1). This discrepancy can be reasonably attributed to the desorption of physically adsorbed initiator molecules during polymer chain growth as stated in a previous report [12]. Indeed, some alkoxyamine molecules are suspected to be only physically attached to the silica surface. Therefore, these physisorbed molecules could progressively desorb from the surface during polymerization as the growing polymer chains are becoming more and more hydrophobic and displays consequently less affinity for the inorganic surface.

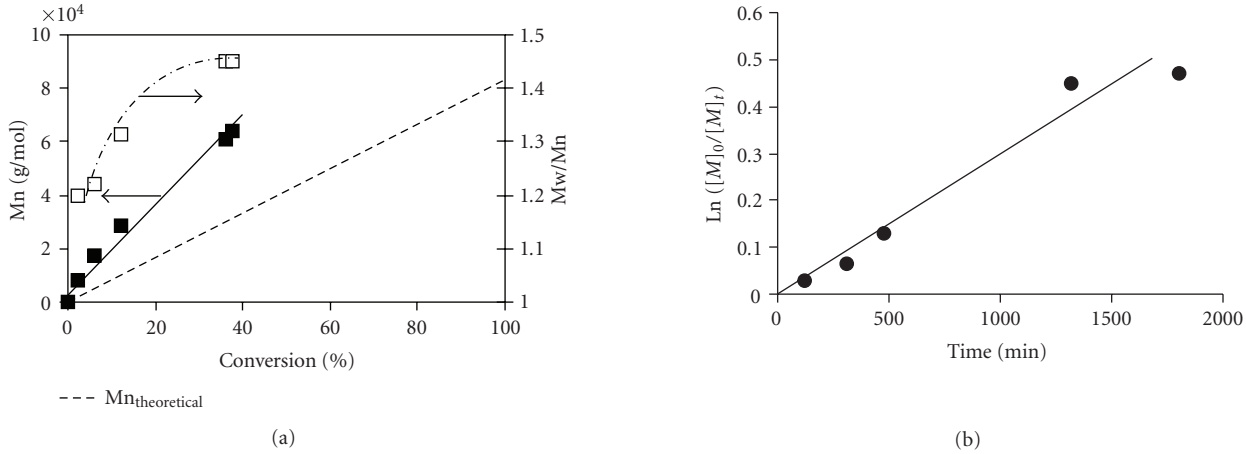

Figure 2: (a) Variation of Mn with conversion and (b) first-order kinetic plot for the DEPN-mediated stable free radical polymerization of styrene in the presence of alkoxyamine-grafted Stöber silica particles (route II). *Initiator-to-styrene molar ratio* = 800.

In route II, the polymerization was conducted in DMF in order to keep a colloidally stable system all along during the growth process. As shown in Figure 2(b), the polymerization exhibited first-order kinetics with respect to total monomer conversion. In addition, Mn evolved linearly with conversion while the polydispersity was lower than 1.5 and increased with increasing conversion. All these results confirm that the graft polymerization of styrene from the Stöber silica surface exhibits all the characteristics of a controlled/"living" polymerization.

However, it can be seen in Figure 2 and in Table 1 that the experimental molecular weights are higher than the theoretical values, Mn_{theo}, determined from the polymerization conversion and the monomer to initiator ratio. The discrepancy between the experimental and theoretical molecular weights may have different origins. First, it may be argued that the steric hindrance of the grafted alkoxyamine is responsible for a loss of initiator efficiency by blocking the access of monomer to all the initiator sites as already observed by Von Werne and Patten [2] and El Harrak et al. [24] for the ATRP of styrene from the surface of Stöber silica particles. But, according to Böttcher et al. [5], this can most likely be ascribed to chain termination reactions promoted on the silica surface by the close proximity of the propagating "living" radicals or by the termination between a free chain formed in solution and a surface-bound polymer at the initial stage of the radical polymerization. However, in the present system, this can be mostly attributed to undesirable side reactions occuring during the formation of the surface alkoxyamine initiator by the reaction of styryl-DEPN with the VETMSB-grafted silica. Indeed, part of the styryl-DEPN molecules could be lost during this coupling step. In order to check if our hypothesis is correct, we doubled the styryl-DEPN concentration into the polymerization medium (run 4 in Table 1). The styrene-to-initiator molar ratio was thus decreased from 800 to 400. The data in Table 1 and the kinetics plots of Figure 3 show

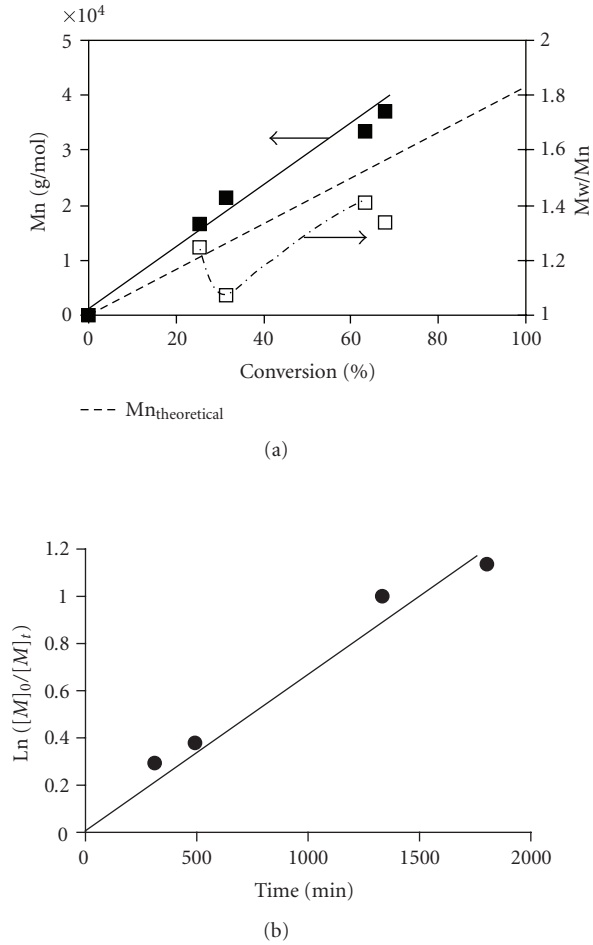

Figure 3: (a) Variation of Mn with conversion and (b) first-order kinetic plot for the DEPN-mediated stable free radical polymerization of styrene in the presence of alkoxyamine-grafted Stöber silica particles (route II). *Initiator-to-styrene molar ratio* = 400.

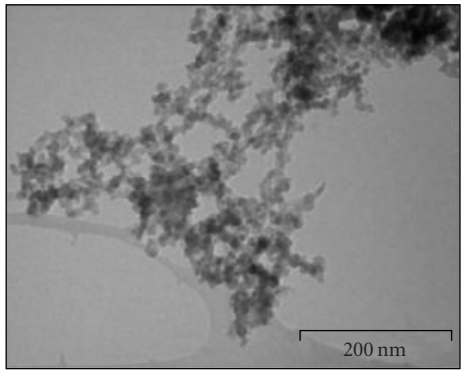

(a)

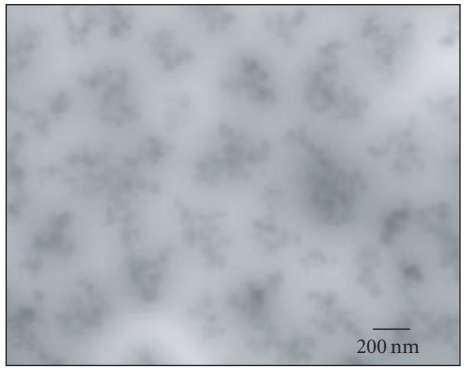

(b)

Figure 4: TEM images of (a) bare fumed silica particles and (b) PS-grafted silica particles cast from dilute toluene suspensions (route I). Mn of free PS = 55500 g·mol^{-1} (sample 2 in Table 1).

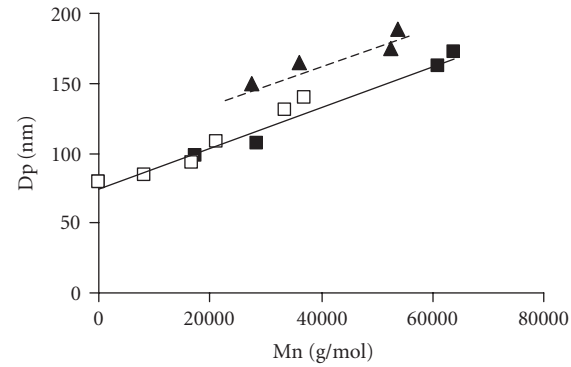

Figure 5: Hydrodynamic diameter of the polystyrene-grafted silica particles as a function of the molecular weight of the grafted polystyrene chains. □ route II, Table 1, *Initiator-to-styrene molar ratio* = 400, ■ route II, *Initiator-to-styrene molar ratio* = 800, ▲ route I, *Initiator-to-styrene molar ratio* = 800.

that the experimental molecular weight, Mn, is closer to the theoretical one in agreement with the above arguments.

Further insight into the grafting mechanism was obtained by determining the polymer chains grafting density. The data in Table 1 indicate that the polystyrene grafting densities estimated from carbon analysis are close to 0.1 μmol/m^2 independently of the styrene-to-initiator molar ratio (runs 3 and 4 in Table 1). This value is three times lower than the polystyrene grafting densities obtained for fumed silica (0.3 μmol/m^2) and confirms the hypothesis according to which termination reactions are promoted on the silica surface due to confinement of the initiator radicals.

3.3. Characterization of the PS-grafted silica suspensions

TEM images of starting silica gel particles and PS-grafted silicas are shown in Figure 4. According to manufacturer's specifications, the diameter of the aerosil silica particles is around 13 nm. However, TEM clearly indicates that the particles form micrometer-sized domains of stringy-shaped aggregates when cast from diluted toluene suspensions (Figure 4(a)). After grafting of the polystyrene chains (Figure 4(b)), the silica particles appear regularly distributed within the polymer film which indicates that the agglomerates have been partly destroyed. It is then clear from these results that the formation of a hairy polymer layer around silica provides a steric barrier against particles aggregation in organic medium.

The above observations were confirmed by DLS measurements which indicated that the dispersability of the silica gel particles in toluene was greatly improved after grafting. The hydrodynamic diameter of the PS-grafted silica increased from 150 nm to 190 nm with increasing the molecular weight of the grafted polymer from 27500 to 55500 g·mol^{-1} (Figure 5) as expected for spherical particles coated with a layer of densely grafted polymer chains [26]. A similar behavior was observed in route II for which the hydrodynamic diameter of the polystyrene-grafted silica particles increased from 80 nm to 170 nm with increasing the polymer molecular weight from 0 to 64000 g·mol^{-1} (Figure 5). It is worthwhile to notice that the two lines have identical slopes.

The linear increase of particles size with the polymer molecular weight indicates the formation of a densely grafted polymer brush on the silica surface. Indeed, as recently argued by Zhao and Brittain [26], the fact that the polymer thickness varies linearly with the degree of polymerization constitutes a strong argument in favor of a polymer brush conformation at the mineral surface. Let us consider for instance PS-grafted silica particles with a hydrodynamic diameter of 98 nm (Figure 5, route II), the average thickness of the polymer shell (whose number average molecular weight is around 17450 g·mol^{-1}) is thus of around 9 nm. Considering that the radius of gyration of polystyrene chains with a molecular weight of 14300 g·mol^{-1} in THF is about 4 nm [2], the thickness of the hairy polymer layer is more than twice the radius of gyration of the polystyrene chains indicating that the later has adopted an extended brush conformation at the silica surface.

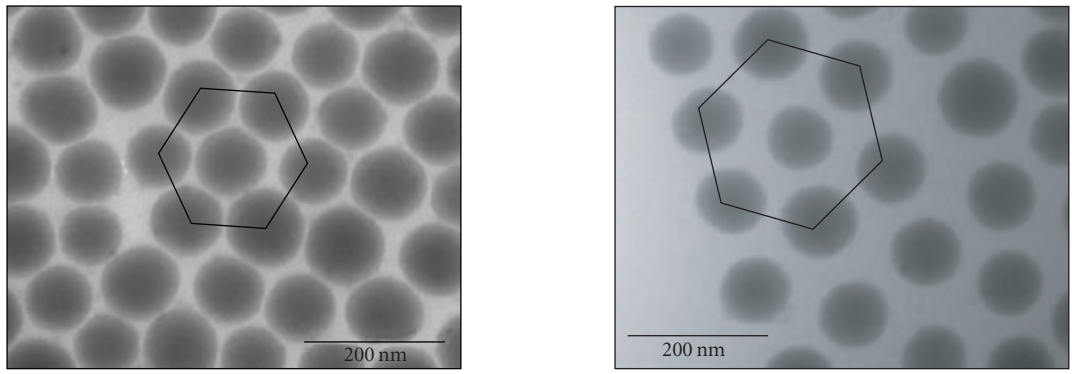

(a) (b)

Figure 6: TEM images of PS-grafted colloidal silica. (a) Mn = 8340 g·mol^{-1} (b) Mn = 61000 g·mol^{-1}.

The TEM images of the PS-grafted Stöber silica with different molecular weights are shown in Figure 6. The silica nanoparticles core appears as dark spheres uniformly dispersed throughout the polymer film (in gray). It can be seen that the interparticle distance increases with increasing the polymer molecular weight as already demonstrated by several authors [2, 22, 27]. This indicates that the film characteristics can be readily manipulated by varying the degree of polymerization of the grafted polymer chains and the silica particles diameter. The regular arrangement of the silica spheres within the film is again in favor of the formation of a well-defined high density polymer brush at the silica surface.

3.4. Miniemulsion polymerization

Although there have been many reports in recent literature on the incorporation of surface-functionalized mineral particles in miniemulsion recipes including clay [17], ZnO, and silica colloids [16], to the best of our knowledge, there are no reports mentioning the utilization of polymer-coated mineral particles. Therefore, in the following, we aim to demonstrate that PS-grafted silica particles can be successfully encapsulated by polystyrene through miniemulsion polymerization according to the procedure detailed in the experimental section. Indeed, as shown in the previous paragraphs, grafting of polystyrene chains to the silica surface is an effective way to enhance their hydrophobicity, prevent particles floculation, and make them compatible with most organic media. As expected, the PS-grafted Stöber particles could be thus successfully dispersed into styrene without particles aggregation which constitutes a key issue of the miniemulsion polymerization process as schematically represented in Figure 7(a). Figure 7(b) displays TEM images of the resulting composite latex particles. The top image shows the formation of a large number of unfilled polystyrene spheres with only one encapsulated silica particle. The ratio between the number of empty and filled latex spheres can be estimated to be around 400 by manually counting directly on the TEM micrograph. The bottom image of Figure 7(b) shows a selected enlarged region on the copper grid. The PS-grafted silica particles appears as dark spheres surrounded by a polystyrene shell in an excentered core-shell morphology. A careful examination of a large number of particles allows us to testify that there are no composite particles containing more than one silica bead. This is presumably due to the diameter of the PS-grafted silica spheres (e.g., around 173 nm) which is close to that of the monomer droplets (see Table 2). It is thus hardly conceivable to have two silica spheres dispersed in a single droplet. In addition, the fact that we did not observe more than one silica particle per composite particle strongly suggests the absence of coalescence during polymerization. It is worth mentioning also that there are no free silica beads in the suspension medium as all the silica particles are surrounded by polymers. Quantitative information on the respective population numbers (e.g., the silica, the silica-loaded monomer droplets, and the composite particles) can be obtained from their respective diameters determined by DLS. The data are shown in Table 2. It can be seen from Table 2 that the number of droplets is two orders of magnitude higher than the silica particles number which is mainly due to the low silica concentration used in this particular experiment. Increasing the silica concentration should allow us to generate a higher proportion of silica-filled particles. In addition, it should be mentioned also that the composite particles number is one order of magnitude higher than the number of droplets which indicates the occurrence of renucleation. The ratio between the number of composite and silica particles is therefore of around 700 in agreement with the above TEM analysis.

In summary, although the experimental conditions need to be optimized in order to get a better agreement between the droplet and particle sizes (by changing, e.g., the nature and/or concentration of the costabilizer) and improve the efficiency of the encapsulation reaction (by increasing the silica particles concentration), the above preliminary experiment has opened a new route to polymer-encapsulated minerals. As a matter of fact, this method should be in principle applicable to various polymer-grafted minerals and thus

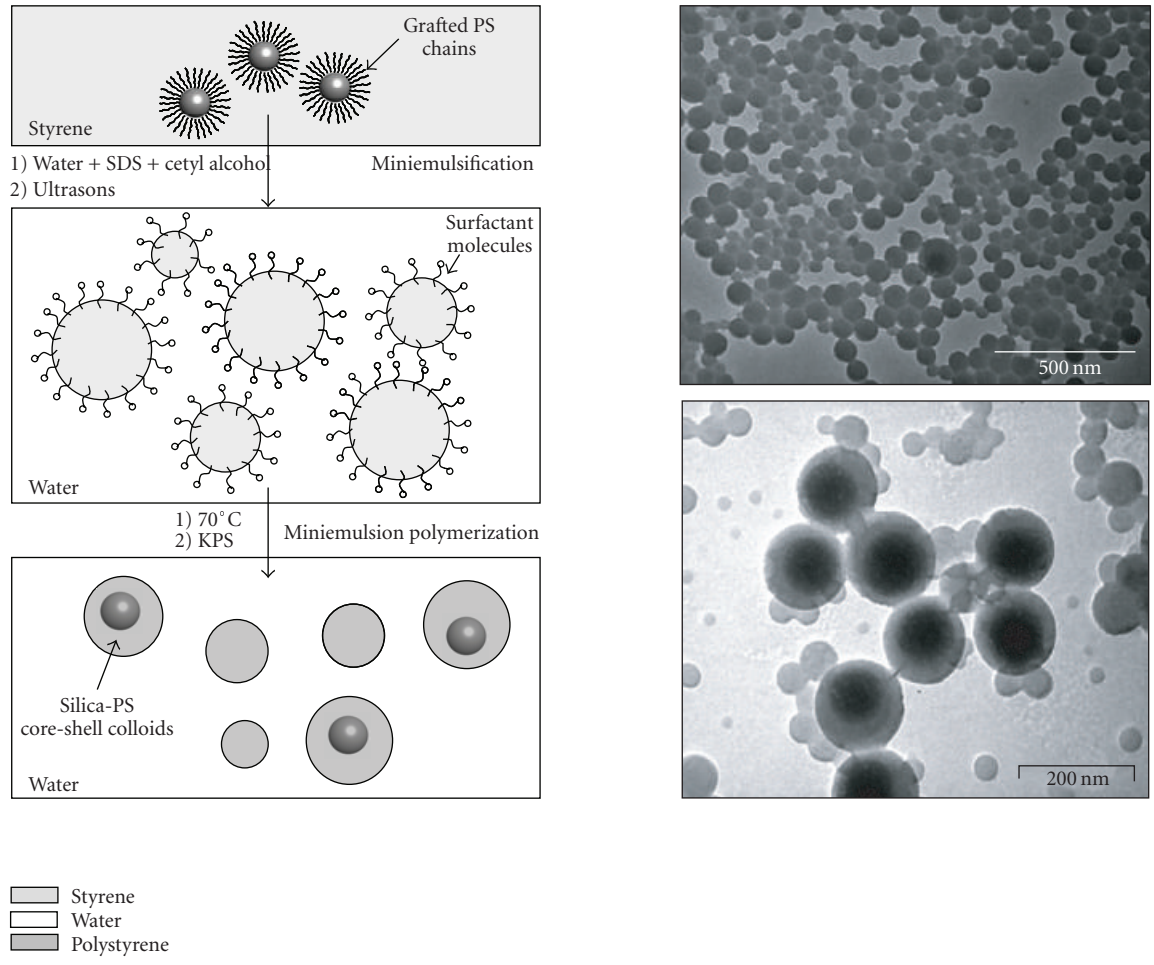

Figure 7: (a) Scheme illustrating the principle of PS-grafted silica particles encapsulation through miniemulsion polymerization and (b) transmission electron micrographs of the thus-produced silica-polystyrene core-shell latex particles. Mn of the grafted polymer chains is around 64000 g·mol^{-1} (run 3 in Table 1); the arrow points out one encapsulated silica particle within unfilled polystyrene spheres.

Table 2: Silica, droplets, and composite particle sizes and numbers during the encapsulation reaction of PS-grafted Stöber silica colloids through miniemulsion polymerization. The molecular weight of the grafted polymer chain is around 64000 g·mol^{-1}, while the diameter of the PS-grafted silica is around 173 nm in DMF.

Particles diameter (nm)[a]			Particles number (per liter of water)		
Silica	Droplets	Composite particles	Silica[b]	Droplets[c]	Composite particles
70.7	212	114.2	$5.2\ 10^{14}$	$6.6\ 10^{16}$	$4.2\ 10^{17}$

[a] Determined by DLS.
[b] Determined using (1) with $[SiO_2] = 10\ g \cdot L^{-1}$.
[c] Determined from the droplet size by considering the overall amount of silica plus monomer.

extendable to other miniemulsion formulations including polar acrylic monomers by correctly defining the nature of the grafted polymer chains. Indeed, polymer-encapsulated minerals are of potential interest in coating applications. The inorganic particles are incorporated into the composite material to improve the mechanical properties of the coating while a good dispersion of the mineral into the polymer matrix ensures the obtention of transparent films.

4. CONCLUSION

Polystyrene chains with molecular weights comprised between 8000 and 64000 g·mol^{-1} and narrow polydispersities were successfully grown from the surface of silica nanoparticles. TEM analysis showed that it was possible to control nanoparticles ordering, interparticles distance, and spatial organization of the inorganic particles within the polymer

matrix by varying the polymer molecular weight. In addition, the PS-grafted silica particles could be successfully redispersed into styrene to generate silica-loaded monomer droplets by miniemulsification. The resulting nanodroplets were polymerized in miniemulsion giving rise to the formation of silica-polystyrene core-shell particles.

REFERENCES

[1] T. Von Werne and T. E. Patten, "Preparation of structurally well-defined polymer-nanoparticle hybrids with controlled/living radical polymerizations [3]," *Journal of the American Chemical Society*, vol. 121, no. 32, pp. 7409–7410, 1999.

[2] T. Von Werne and T. E. Patten, "Atom transfer radical polymerization from nanoparticles: a tool for the preparation of well-defined hybrid nanostructures and for understanding the chemistry of controlled/"living" radical polymerizations from surfaces," *Journal of the American Chemical Society*, vol. 123, no. 31, pp. 7497–7505, 2001.

[3] T. Von Werne, S. Farmer, I. M. Suehiro, and T. E. Patten, "Composite films of polymer-inorganic hybrid nanoparticles prepared using controlled/"living" radical polymerization," *Polymeric Materials: Science and Engineering*, vol. 82, pp. 294–295, 2000.

[4] C. Perruchot, M. A. Khan, A. Kamitsi, S. P. Armes, T. Von Werne, and T. E. Patten, "Synthesis of well-defined, polymer-grafted silica particles by aqueous ATRP," *Langmuir*, vol. 17, no. 15, pp. 4479–4481, 2001.

[5] H. Böttcher, M. L. Hallensleben, S. Nuss, and H. Wurm, "ATRP grafting from silica surface to create first and second generation of grafts," *Polymer Bulletin*, vol. 44, no. 2, pp. 223–229, 2000.

[6] J. Parvole, L. Billon, and J. P. Montfort, "Formation of polyacrylate brushes on silica surfaces," *Polymer International*, vol. 51, no. 10, pp. 1111–1116, 2002.

[7] A. Kasseh, A. Ait-Kadi, B. Riedl, and J. F. Pierson, "Organic/inorganic hybrid composites prepared by polymerization compounding and controlled free radical polymerization," *Polymer*, vol. 44, no. 5, pp. 1367–1375, 2003.

[8] R. Inoubli, S. Dagréou, A. Khoukh, F. Roby, J. Peyrelasse, and L. Billon, "'Graft from' polymerization on colloidal silica particles: elaboration of alkoxyamine grafted surface by in situ trapping of carbon radicals," *Polymer*, vol. 46, no. 8, pp. 2486–2496, 2005.

[9] J. Parvole, G. Laruelle, A. Khoukh, and L. Billon, "Surface initiated polymerization of poly(butyl acrylate) by nitroxide mediated polymerization: first comparative polymerization of a bimolecular and a unimolecular initiator-grafted silica particles," *Macromolecular Chemistry and Physics*, vol. 206, no. 3, pp. 372–382, 2005.

[10] C. Bartholome, E. Beyou, E. Bourgeat-Lami, P. Chaumont, and N. Zydowicz, "Nitroxide-mediated polymerizations from silica nanoparticle surfaces: "graft from" polymerization of styrene using a triethoxysilyl-terminated alkoxyamine initiator," *Macromolecules*, vol. 36, no. 21, pp. 7946–7952, 2003.

[11] C. Bartholome, E. Beyou, E. Bourgeat-Lami, P. Chaumont, F. Lefebvre, and N. Zydowicz, "Nitroxide-mediated polymerization of styrene initiated from the surface of silica nanoparticles. In situ generation and grafting of alkoxyamine initiators," *Macromolecules*, vol. 38, no. 4, pp. 1099–1106, 2005.

[12] C. Bartholome, E. Beyou, E. Bourgeat-Lami, P. Chaumont, and N. Zydowicz, "Nitroxide-mediated polymerization of styrene initiated from the surface of fumed silica. Comparison of two synthetic routes," *Polymer*, vol. 46, no. 19, pp. 8502–8510, 2005.

[13] S. Blomberg, S. Ostberg, E. Harth, A. W. Bosman, B. Van Horn, and C. J. Hawker, "Production of crosslinked, hollow nanoparticles by surface-initiated living free-radical polymerization," *Journal of Polymer Science, Part A: Polymer Chemistry*, vol. 40, no. 9, pp. 1309–1320, 2002.

[14] F. Tiarks, K. Landfester, and M. Antonietti, "Encapsulation of carbon black by miniemulsion polymerization," *Macromolecular Chemistry and Physics*, vol. 202, no. 1, pp. 51–60, 2001.

[15] L. P. Ramírez and K. Landfester, "Magnetic polystyrene nanoparticles with a high magnetite content obtained by miniemulsion processes," *Macromolecular Chemistry and Physics*, vol. 204, no. 1, pp. 22–31, 2003.

[16] S.-W. Zhang, S.-X. Zhou, Y.-M. Weng, and L.-M. Wu, "Synthesis of SiO_2/polystyrene nanocomposite particles via miniemulsion polymerization," *Langmuir*, vol. 21, no. 6, pp. 2124–2128, 2005.

[17] Q. Sun, Y. Deng, and Z. L. Wang, "Synthesis and characterization of polystyrene-encapsulated laponite composites via miniemulsion polymerization," *Macromolecular Materials and Engineering*, vol. 289, no. 3, pp. 288–295, 2004.

[18] J. L. Couturier and O. Guerret, WO 0212149, 2002.

[19] W. Stöber, A. Fink, and E. Bohn, "Controlled growth of monodisperse silica spheres in the micron size range," *Journal of Colloid and Interface Science*, vol. 26, no. 1, pp. 62–69, 1968.

[20] A. P. Philipse and A. Vrij, "Preparation and properties of nonaqueous model dispersions of chemically modified, charged silica spheres," *Journal of Colloid and Interface Science*, vol. 128, no. 1, pp. 121–136, 1989.

[21] E. Bourgeat-Lami and J. Lang, "Encapsulation of inorganic particles by dispersion polymerization in polar media 1. Silica nanoparticles encapsulated by polystyrene," *Journal of Colloid and Interface Science*, vol. 197, no. 2, pp. 293–308, 1998.

[22] A. El Harrak, G. Carrot, J. Oberdisse, C. Eychenne-Baron, and F. Boué, "Surface-atom transfer radical polymerization from silica nanoparticles with controlled colloidal stability," *Macromolecules*, vol. 37, no. 17, pp. 6376–6384, 2004.

[23] C. Perruchot, M. A. Khan, A. Kamitsi, et al., "XPS characterisation of core-shell silica-polymer composite particles synthesised by atom transfer radical polymerisation in aqueous media," *European Polymer Journal*, vol. 40, no. 9, pp. 2129–2141, 2004.

[24] A. El Harrak, G. Carrot, J. Oberdisse, J. Jestin, and F. Boué, "Control of the colloidal stability of polymer-grafted-silica nanoparticles obtained by atom transfer radical polymerization," *Macromolecular Symposia*, vol. 226, no. 1, pp. 263–278, 2005.

[25] K. Ohno, T. Morinaga, K. Koh, Y. Tsujii, and T. Fukuda, "Synthesis of monodisperse silica particles coated with well-defined, high-density polymer brushes by surface-initiated atom transfer radical polymerization," *Macromolecules*, vol. 38, no. 6, pp. 2137–2142, 2005.

[26] B. Zhao and W. J. Brittain, "Polymer brushes: surface-immobilized macromolecules," *Progress in Polymer Science (Oxford)*, vol. 25, no. 5, pp. 677–710, 2000.

[27] K. Ohno, K. Koh, Y. Tsujii, and T. Fukuda, "Synthesis of gold nanoparticles coated with well-defined, high-density polymer brushes by surface-initiated living radical polymerization," *Macromolecules*, vol. 35, no. 24, pp. 8989–8993, 2002.

Hindawi Publishing Corporation
Journal of Nanomaterials
Volume 2006, Article ID 21656, Pages 1–7
DOI 10.1155/JNM/2006/21656

Preparation and Properties of Polyester-Based Nanocomposite Gel Coat System

P. Jawahar and M. Balasubramanian

Composites Technology Center and Department of Metallurgical and Materials Engineering, Indian Institute of Technology, Madras, Chennai 600036, India

Received 30 January 2006; Revised 19 July 2006; Accepted 13 December 2006

Nanocomposite gel coat system is prepared using unsaturated polyester resin with aerosil powder, $CaCO_3$, and organoclay. The influence of organoclay addition on mechanical and water barrier properties of gel coat system is studied for different amount (1, 2, and 3 wt %) of organoclay. The nanolevel incorporation of organoclay improves the mechanical and water barrier properties of nanocomposite gel coat system. The nanocomposite gel coat system exhibits 55% improvement in tensile modulus and 25% improvement in flexural modulus. There is a 30% improvement in impact property of nanocomposite gel coat system. The dynamic mechanical analysis shows a slight increase in glass transition temperature for nanocomposite gel coat system.

1. INTRODUCTION

At present, the research attention has been focused on a new class of material called "clay polymer nanocomposites" after the discovery that polymer properties can be significantly improved by the presence of nanosize clay particles [1–3]. Lots of research works have been carried out in different polymer systems [4–8] based on this concept. Smectite group clays are normally used as a basic reinforcing element in nanocomposites, because of the high aspect ratio and platy morphology [9–11].

The montmorillonite clay belongs to the family of Smectite clays. It is a crystalline material consisting of 1 nm thick sheets. These silicate sheets consist of alumina octahedra sandwiched by two silica tetrahedra. The length of the individual sheets can range from 30 to 100 nm. Isomorphic substitution of alumina by magnesium results in net negative charge on the surface of the sheets which is balanced by exchangeable cations like Na^+ or Ca^+. These cations can be readily exchanged with alkyl-ammonium ions on organomodification. These alkyl-ammonium ions lowers the surface energy of the inorganic host and improve the wetting characteristics with the polymer [12].

Incorporation of nanosize clay platelets to the polymer matrix increases modulus and strength [13]. Nanosize clay platelets decrease permeability [14, 15], shrinkage [16, 17], and increase resistance to heat and flammability [18, 19]. The fracture energy of the clay-polyester nanocomposite could be doubled even at low concentration (1.5 wt %) of clay [20]. The formation mechanism based on fabrication methods has been reported for unsaturated polyester-layered silicate nanocomposites [21]. The method of mixing clay in polyester resin, curing agents, and curing conditions influence the properties of nanocomposites [22, 23]. The effect of nanoclay on the cure kinetics of unsaturated polyester resin in the range of 35 to 65°C was investigated by Xu and Lee [24]. The clay-polyester nanocomposites produced using reactive organoclay had better dynamic modulus [25].

Composites with gel coats are an essential part of many aspects of life today; from bathroom units to boats; from cultured marble to airplane structures; from windmills to automotive parts. Gel coat imparts good surface finish and bears better hardness, scratch resistance, and resistance to corrosion and water absorption to the composites. It is expected that the incorporation of nanoclay in gel coat would lead to an improvement in the properties, which will make the material viable in high-loading environment.

In the present work, nanocomposite gel coat system was prepared using unsaturated polyester resin with aerosil and $CaCO_3$ powders and organoclay. The influence of organoclay addition on mechanical, thermal, and water barrier properties of gel coat system has been studied.

2. EXPERIMENTAL PROCEDURE

The resin used for gel coat is isophthalic polyester resin (PE), procured from Vasavibala resins (P) Ltd., Chennai. The organo-modified clay (OMC) used is dodecylamine treated montmorillonite clay processed in the laboratory as reported elsewhere [26]. Fillers used are $CaCO_3$ powders of average size 48 μm and aerosil powder of average size 6 μm procured from Jain Industrial chemicals, Chennai.

300 ml of isophthalic polyester resin was taken in a container. Organoclay of definite proportion (1, 2, and 3 wt %) was added to produce nanoclay dispersed polyester mix. It was stirred well using a mechanical stirrer at 1000 rpm for 1 h. To produce nanocomposite gel coat system, 2 wt % of aerosil powder was added to the clay dispersed resin and mixed manually using glass rod and then 10 wt % of calcium carbonate was added and mixed well. Similarly, conventional gel coat system was also prepared with the same procedure without the addition of nanoclay to the polyester resin. Methyl ethyl ketone peroxide catalyst (1.5 wt %) and cobalt napthanate accelerator (1.5 wt %) were added to the mixture to initiate the curing reaction. Sheets of size 300 $\times$ 300 $\times$ 3 mm^3 were cast in a glass mold and allowed to cure for 24 h at room temperature followed by post curing at 70°C for 3 h.

X-ray diffraction (XRD) was carried out for organoclay-filled polyester to study the state of clay dispersion. It was carried out with a scanning rate of 2°/min with Cu-Kα radiation using SHIMADZU, XD-DI X-ray diffractometer. Transmission electron microscopic characterization was carried out using JEOL JEM 1200EX electron microscope. The density of gel coat systems was measured using Archimedes principle.

Tensile tests (ASTM D-638) were performed at room temperature using Instron 4301 universal testing machine (UTM), with a crosshead speed of 2 mm/min. Mechanically fractured tensile samples were analyzed using JEOL JSM-840 A scanning electron microscope (SEM) with EDAX. Flexural properties were evaluated using Instron 4301 UTM as per ASTM D-790 standard. Izod impact strength was determined using Frank impact testing machine following ASTM D-256 standard. A 7.5 joules izod impact hammer was used. Dynamic mechanical analysis (DMA) was performed using Netzsch (DMA 242C) dynamic-mechanical analyzer in the three-point bending mode at a frequency of 10 Hz and amplitude of 120 μm over the temperature range of 30–180°C at the heating rate of 5°C/min. Water barrier properties were determined according to ASTM D-570.

3. RESULTS AND DISCUSSION

XRD patterns of organoclay (OMC) and polyester filled with OMC are shown in Figure 1. The 001 basal plane diffraction peak of OMC is absent in composites filled with organoclay (1, 2, and 3 wt %). This reveals that the interlayer distance of OMC is more than 70 Å or the layers are randomly dispersed in the polymer matrix.

Figure 2 shows the TEM micrograph of polyester filled with 1, 2, and 3 wt % organoclay. The clay platelets are well exfoliated and spacing between the clay platelets is more than 70 Å. This confirms the formation of well-exfoliated structure on addition of 1, 2, and 3 wt % organoclay and also supports the XRD data.

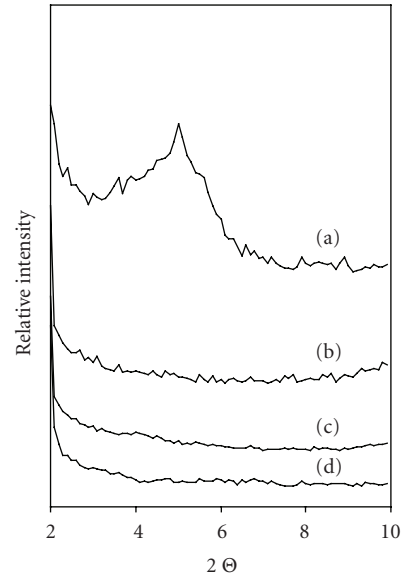

Figure 1: XRD patterns for (a) organoclay and polyester with (b) 1 wt % OMC, (c) 2 wt % OMC, (d) 3 wt % OMC.

Density values of conventional gel coat and nanocomposite gel coat are shown in Figure 3. The density of conventional gel coat system is 1.41 g/cm^3. It remains almost same with the addition of organoclay up to 2 wt %. The density decreases to 1.32 g/cm^3 for the organoclay content of 3 wt %. The decrease in density of nanocomposite gel coat with 3 wt % may be due to the presence of pores. During mixing of organoclay with polyester resin, the viscosity increases and it is high for the organoclay content of 3 wt %. So the entrapped air during mixing finds it difficult to escape out of polyester matrix and remains as pores.

The tensile properties of gel coat system with and without clay are shown in Figures 4 and 5. The tensile strength of conventional gel coat is 38 MPa (Figure 4). Tensile strength increases with increase in organoclay content. It increases to the value of 46 MPa for the organoclay content of 2 wt %. Thereafter, it decreases to the value of 33 MPa. The tensile modulus follows an increasing trend (Figure 5). It increases from the value of 4.5 GPa for conventional gel coat to the value of 7 GPa for the organoclay content of 3 wt %.

Figure 6 shows the fracture surface of conventional gel coat system and nanocomposite gel coat systems with 1, 2, and 3 wt % organoclay. The mode of failure is brittle in both the gel coats. The facets on fracture surface of conventional gel coat appear glassy. It indicates that the material is highly brittle and the mode of failure is highly catastrophic. In the case of nanoclay dispersed gel coat system, the fracture surface seems to be rough with fine facets. This indicates the formation of strong bonding between nanoclay and polyester resin and due to this, the nanocomposite gel coat

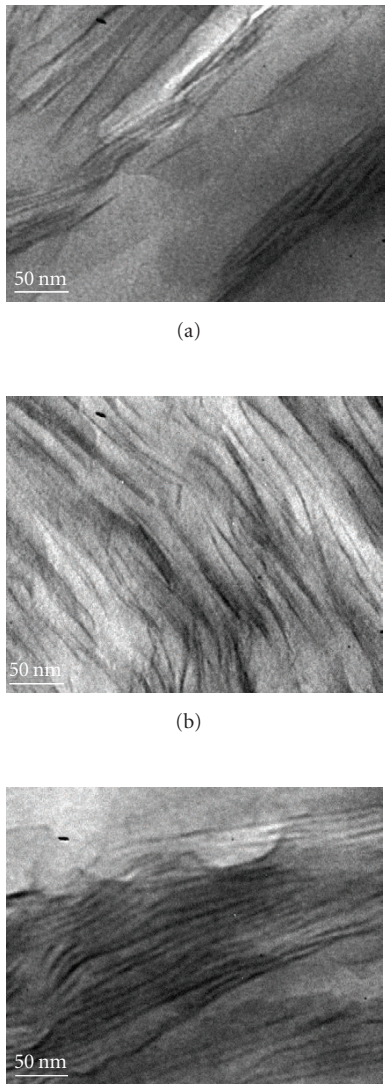

Figure 2: TEM micrographs of polyester filled with (a) 1 wt % OMC, (b) 2 wt % OMC, and (c) 3 wt % OMC.

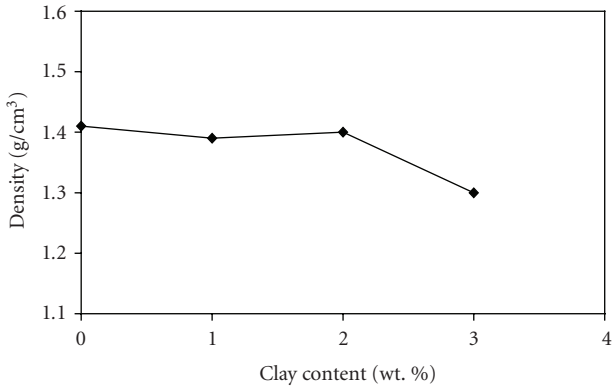

Figure 3: Density of gel coat systems.

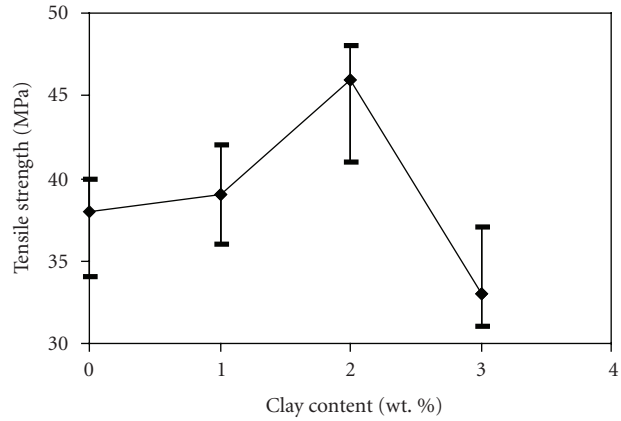

Figure 4: Tensile strength of gel coat systems.

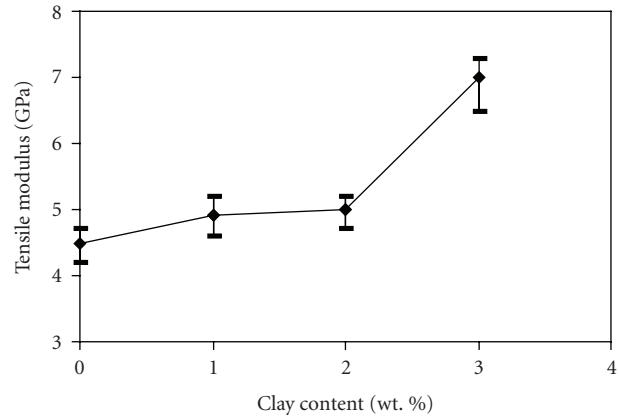

Figure 5: Tensile modulus of gel coat systems.

system with 1 and 2 wt % organoclay has better strength. For nanocomposite gel coats with 3 wt % organoclay, the facets are large compared to the gel coat system with 1 and 2 wt % organoclay. This indicates that the nanocomposite gel coat with 3 wt % organoclay has less load bearing capacity. The tensile fracture surface of conventional gel coat shows agglomerates of $CaCO_3$ and aerosil powder. EDAX analysis (Figure 7) of agglomerates shows more calcium content (Figure 7(a)). The amount of calcium found in the agglomerates region is 25.24 wt %, whereas the analysis carried out on the entire region shows a nominal value of 9.05 wt % Ca (Figure 7(b)). EDAX analysis confirms the presence of agglomerated $CaCO_3$ fillers in the conventional gel coat system. Surprisingly no agglomerates are found for nanocomposite gel coat system. This suggests that the exfoliated clay platelets present in the polyester matrix might be inducing some mechanism to prevent agglomeration of fillers.

Flexural strength of conventional gel coat system is 95 MPa (Figure 8). It increases to the value of 105 MPa for the nanocomposite gel coat system with 2 wt %. Thereafter, it decreases to the value of 91 MPa for the clay content of 3 wt %. The flexural modulus increases from the value of 3.9 GPa for

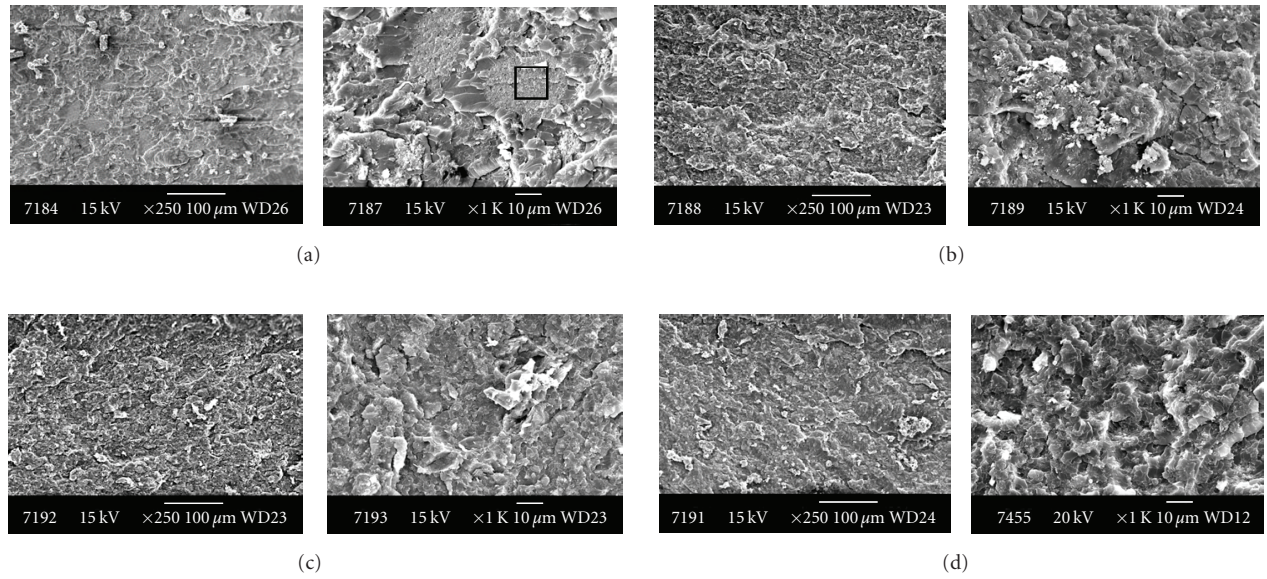

Figure 6: SEM micrographs of tensile fracture surface for (a) conventional gel coat and nanocomposite gel coats with (b) 1 wt % OMC, (c) 2 wt % OMC, (d) 3 wt % OMC.

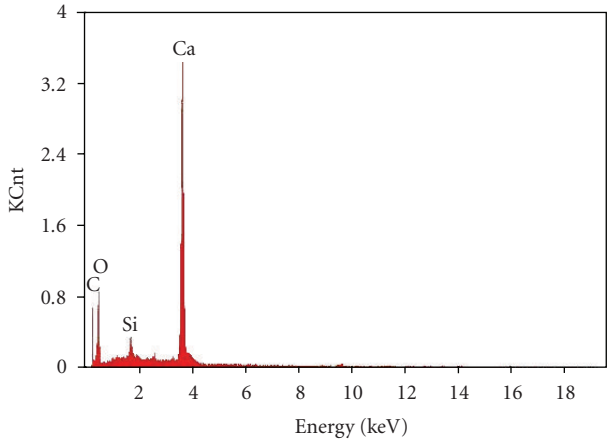

(a)

Element	*wt %*	*at %*
CK	25.71	37.00
OK	47.13	50.93
SiK	01.92	01.18
CaK	25.24	10.89

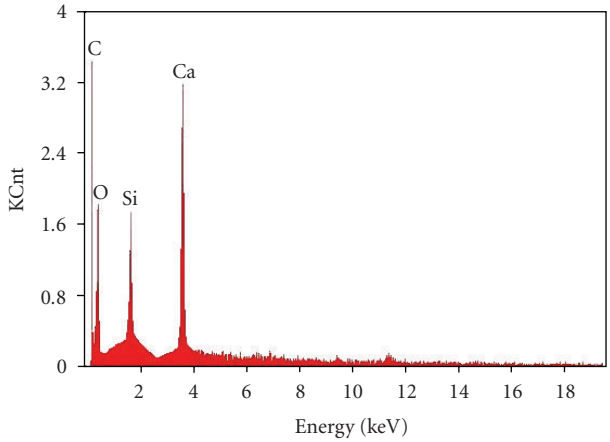

(b)

Element	*wt %*	*at %*
CK	49.25	57.91
OK	40.06	36.86
SiK	01.64	01.91
CaK	09.05	03.32

Figure 7: EDAX on conventional gel coat (a) agglomerated region (marked in Figure 6(a)), (b) entire region.

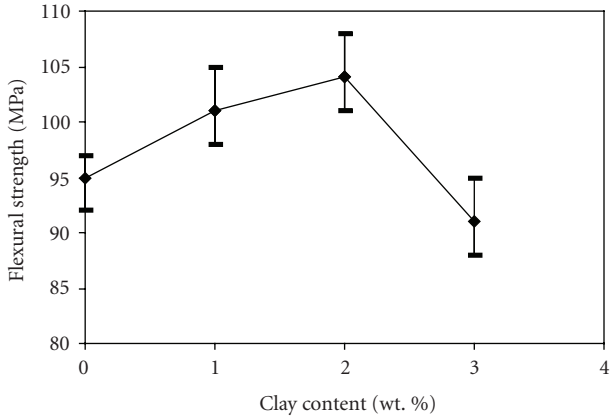

Figure 8: Flexural strength of gel coat systems.

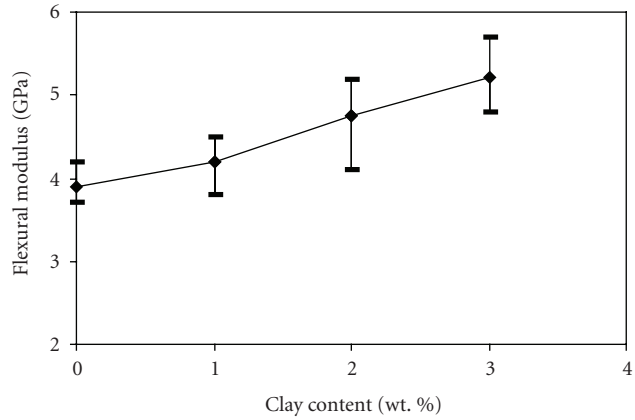

Figure 9: Flexural modulus of gel coat systems.

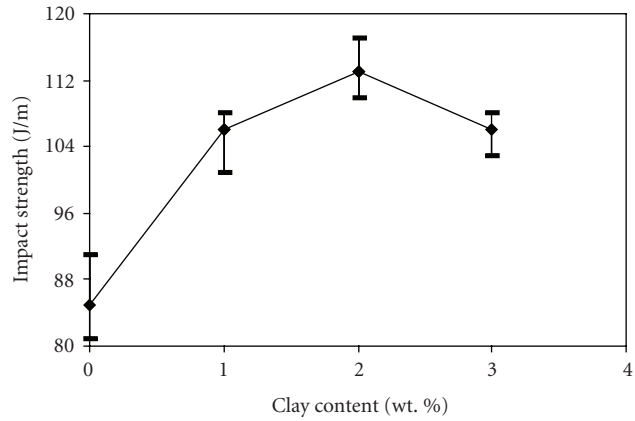

Figure 10: Impact strength of gel coat systems.

conventional gel coat system to the value of 5.2 GPa for the nanocomposite gel coat system with a clay content of 3 wt % (Figure 9).

The improvement in mechanical properties is due to the presence of well-exfoliated nanoclay and interaction of nanosize clay layers with the polymer matrix, as well as on the rigid nature of the clay layers [27]. Crack pinning and crack bifurcation are some of the strengthening mechanisms responsible for the increase in strength of nanocomposites [20, 28, 29].

Improvement in tensile strength and flexural strength is not significant for nanocomposite gel coat system with 3 wt % organoclay. Even though the nanosize clay acts as load bearing component, the dispersion of exfoliated clay platelets might have hindered the crosslinking of the polymer chains [30]. The decrease in strength at higher clay content (3 wt %) may also be due to the increase in viscosity of the polyester resin. The increase in viscosity may lead to improper mixing of $CaCO_3$ and aerosil powders. Moreover, the air entrapped during shear mixing may not escape out of the system and remains as micropore in the nanocomposite gel coats, which leads to a decrease in strength.

Impact strength of the conventional gel coat system is 85 J/m (Figure 10). It increases to 106 J/m and 113 J/m for the organoclay contents of 1 and 2 wt %, respectively. It decreases to the value of 96 J/m for the organoclay content of 3 wt %. The nanosize clay platelets play a vital role for the improvement in impact strength. The nanoclay acts as crack stoppers with increase in organoclay content and form a tortuous pathway for crack propagation resulting in higher impact energy [31].

Storage modulus is higher for the gel coat system with organoclay (Figure 11). At 40°C the conventional gel coat system has a storage modulus of 7432 MPa. The storage modulus for nanocomposite gel coat systems are 7794 MPa, 8435 MPa, and 7557 MPa for the organoclay content of 1, 2, and 3 wt %, respectively. The improvement in storage modulus is due to the presence of exfoliated clay platelets in the polyester matrix. The deterioration in properties for 3 wt % organoclay may be due to the presence of pores, which is confirmed by the decrease in density (Figure 3).

Figure 12 shows the variation of damping factor (tan δ) for conventional and nanocomposite gel coat systems. The damping factor increases on addition of organoclay. The stiffness variation between the nanoclay and polymer matrix might have caused internal damping, resulting in increased damping factor for nanocomposite gel coats [32].

Glass transition temperature (T_g) corresponds to the peak tan δ value in the dynamic mechanical analysis curve (Figure 12). T_g increases slightly on addition of organoclay from the value of 117°C for conventional gel coat system to the value of 123°C for the nanocomposite gel coat system containing 1 wt % organoclay and it decreases to the value of 121°C for the nanocomposite gel coat system containing 3 wt % organoclay. The decrease in T_g for the nanocomposite gel coat system with 3 wt % clay indicates that there is reduction in crosslink density. This improvement in T_g suggests that the clay nanofillers stiffens the polymer matrix at high temperatures. Due to the large surface area of the nanoclay platelets, large amount of polymer chains have strong contact with the clay surfaces and prevents segmental motion of the polymeric chains [27]. At increased temperature, many

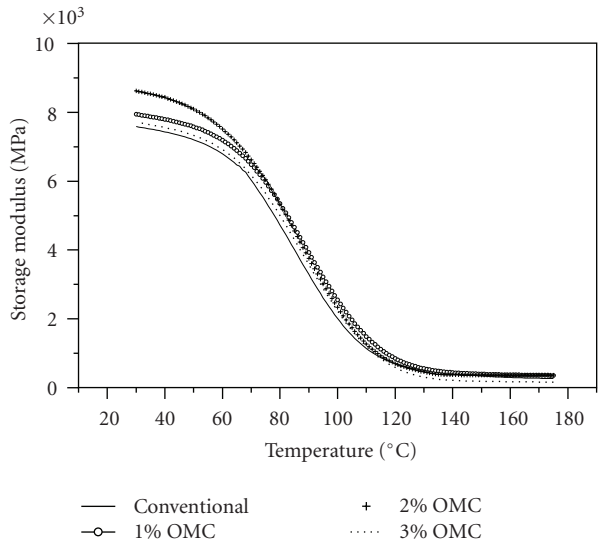

Figure 11: Storage modulus of gel coat systems.

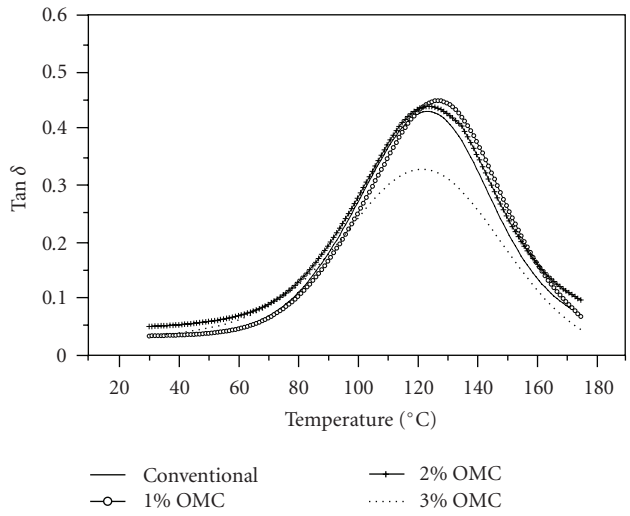

Figure 12: Loss factor (tan δ) of gel coat systems.

polymeric chains will not experience softness due to the hard barrier phase.

Water absorption of conventional and nanocomposite gel coat systems are shown in Figure 13. The water absorption resistance for nanocomposite gel coat system is better compared to the conventional gel coat. Water absorption resistance increases with the addition of organoclay up to 2 wt %. It decreases on further clay addition, but it is well above the limit compared to the conventional gel coat. The exfoliated clay platelets present in the polyester matrix act as barrier and increases the mean effective path for the water molecules to travel, and also lead to an increase in water absorption resistance [33].

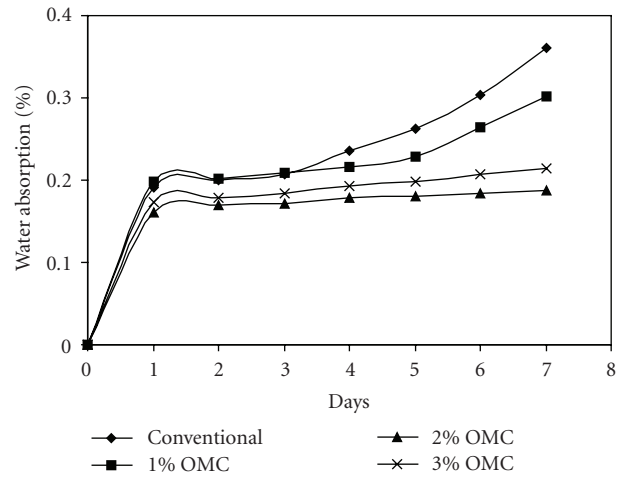

Figure 13: Water absorption of gel coat systems.

4. CONCLUSIONS

Nanocomposite gel coat systems were prepared using unsaturated polyester resin as matrix with aerosil and $CaCO_3$ powders and organoclay. The nanolevel incorporation of organoclay improves the mechanical and water barrier properties of nanocomposite gel coat systems. The dynamic mechanical analysis shows a slight improvement in storage modulus and glass transition temperature for nanocomposite gel coat systems.

REFERENCES

[1] A. Usuki, M. Kawasumi, Y. Kojima, A. Okada, T. Kurauchi, and O. Kamigaito, "Swelling behavior of montmorillonite cation exchanged for ω-amino acids by ϵ-caprolactam," *Journal of Materials Research*, vol. 8, no. 5, pp. 1174–1178, 1993.

[2] A. Usuki, Y. Kojima, M. Kawasumi, et al., "Synthesis of nylon 6-clay hybrid," *Journal of Materials Research*, vol. 8, no. 5, pp. 1179–1184, 1993.

[3] Y. Kojima, A. Usuki, M. Kawasumi, A. Okada, T. Kurauchi, and O. Kamigaito, "Synthesis of nylon 6-clay hybrid by montmorillonite intercalated with ϵ-caprolactam," *Journal of Polymer Science Part A: Polymer Chemistry*, vol. 31, no. 4, pp. 983–986, 1993.

[4] X. Kornmann, H. Lindberg, and L. A. Berglund, "Synthesis of epoxy-clay nanocomposites: influence of the nature of the clay on structure," *Polymer*, vol. 42, no. 4, pp. 1303–1310, 2001.

[5] M. Krook, A.-C. Albertsson, U. W. Gedde, and M. S. Hedenqvist, "Barrier and mechanical properties of montmorillonite/polyesteramide nanocomposites," *Polymer Engineering & Science*, vol. 42, no. 6, pp. 1238–1246, 2002.

[6] D. M. Delozier, R. A. Orwoll, J. F. Cahoon, J. S. Ladislaw, J. G. Smith Jr., and J. W. Connell, "Polyimide nanocomposites prepared from high-temperature, reduced charge organoclays," *Polymer*, vol. 44, no. 8, pp. 2231–2241, 2003.

[7] B. K. Kim, J. W. Seo, and H. M. Jeong, "Morphology and properties of waterborne polyurethane/clay nanocomposites," *European Polymer Journal*, vol. 39, no. 1, pp. 85–91, 2003.

[8] A. Usoki, M. Kato, A. Okada, and T. Kurauchi, "Synthesis of polypropylene-clay hybrid," *Journal of Applied Polymer Science*, vol. 63, no. 1, pp. 137–139, 1997.

[9] P. D. Kaviratna, T. Lan, and T. J. Pinnavaia, "Synthesis of polyether-clay nanocomposites: kinetics of epoxide self-polymerization in acidic smectite clay," *Polymer Preprints*, vol. 35, no. 1, pp. 788–793, 1994.

[10] T. J. Pinnavaia, "Intercalated clay catalysts," *Science*, vol. 220, no. 4595, pp. 365–371, 1983.

[11] T. Lan and T. J. Pinnavaia, "Clay-reinforced epoxy nanocomposites," *Chemistry of Materials*, vol. 6, no. 12, pp. 2216–2219, 1994.

[12] E. P. Giannelis, R. Krishnamoorti, and E. Manias, "Polymer-silicate nanocomposites: model systems for confined polymers and polymer brushes," in *Polymers in Confined Environments*, vol. 138 of *Advances in Polymer Science*, pp. 107–147, Springer, New York, NY, USA, 1999.

[13] Y. Kojima, A. Usuki, M. Kawasumi, et al., "Mechanical properties of nylon 6-clay hybrid," *Journal of Materials Research*, vol. 8, no. 5, pp. 1185–1189, 1993.

[14] K. Yano, A. Usuki, A. Okada, T. Kurauchi, and O. Kamigaito, "Synthesis and properties of polymide-clay hybrid," *Journal of Polymer Science Part A: Polymer Chemistry*, vol. 31, no. 10, pp. 2493–2498, 1993.

[15] Y. Kojima, K. Fukumori, A. Usuki, A. Okada, and T. Kurauchi, "Gas permeabilities in rubber-clay hybrid," *Journal of Materials Science Letters*, vol. 12, no. 12, pp. 889–890, 1993.

[16] P. Kelly, A. Akelah, S. Qutubuddin, and A. Moet, "Reduction of residual stress in montmorillonite/epoxy compounds," *Journal of Materials Science*, vol. 29, no. 9, pp. 2274–2280, 1994.

[17] E. Haque and C. D. Armeniades, "Montmorillonite polymer concrete: zero-shrinkage and expanding polymer concrete with enhanced strength," *Polymer Engineering & Science*, vol. 26, no. 21, pp. 1524–1530, 1986.

[18] E. P. Giannelis, "Polymer layered silicate nanocomposites," *Advanced Materials*, vol. 8, no. 1, pp. 29–35, 1996.

[19] J. D. Lee, T. Takekoshi, and E. P. Giannelis, "Fire retardant polyetherimide nanocomposites," in *Proceedings of the Materials Research Society Symposium*, vol. 457, pp. 513–518, Pittsburgh, Pa, USA, December 1997.

[20] X. Kornmann, L. A. Berglund, J. Sterte, and E. P. Giannelis, "Nanocomposites based on montmorillonite and unsaturated polyester," *Polymer Engineering & Science*, vol. 38, no. 8, pp. 1351–1358, 1998.

[21] B. Lepoittevin, N. Pantoustier, M. Devalckenaere, et al., "Polymer/layered silicate nanocomposites by combined intercalative polymerization and melt intercalation: a masterbatch process," *Polymer*, vol. 44, no. 7, pp. 2033–2040, 2003.

[22] D. J. Suh, Y. J. Lim, and O. O. Park, "The property and formation mechanism of unsaturated polyester-layered silicate nanocomposite depending on the fabrication methods," *Polymer*, vol. 41, no. 24, pp. 8557–8563, 2000.

[23] I. Mironi-Harpaz, M. Narkis, and A. Siegmann, "Nanocomposite systems based on unsaturated polyester and organoclay," *Polymer Engineering & Science*, vol. 45, no. 2, pp. 174–186, 2005.

[24] L. Xu and L. J. Lee, "Kinetic analysis and mechanical properties of nanoclay reinforced unsaturated polyester (UP) resins cured at low temperatures," *Polymer Engineering & Science*, vol. 45, no. 4, pp. 496–509, 2005.

[25] A. F. Xiao and Q. Syed, "Synthesis of unsaturated polyester-clay nanocomposites using reactive organoclays," *Polymer Engineering & Science*, vol. 44, no. 2, pp. 345–351, 2004.

[26] R. Magaraphan, W. Lilayuthalert, A. Sirivat, and J. W. Schwank, "Preparation, structure, properties and thermal behavior of rigid-rod polyimide/montmorillonite nanocomposites," *Composites Science and Technology*, vol. 61, no. 9, pp. 1253–1264, 2001.

[27] J.-H. Chang, B.-S. Seo, and D.-H. Hwang, "An exfoliation of organoclay in thermotropic liquid crystalline polyester nanocomposites," *Polymer*, vol. 43, no. 10, pp. 2969–2974, 2002.

[28] W. Bernd, H. Frank, and Q. Z. Ming, "Epoxy nanocomposites with high mechanical and tribological performance," *Composites Science and Technology*, vol. 63, no. 14, pp. 2055–2067, 2003.

[29] J. H. Park and S. C. Jana, "The relationship between nano- and micro-structures and mechanical properties in PMMA-epoxy-nanoclay composites," *Polymer*, vol. 44, no. 7, pp. 2091–2100, 2003.

[30] R. K. Bharadwaj, A. R. Mehrabi, C. Hamilton, et al., "Structure-property relationships in cross-linked polyester-clay nanocomposites," *Polymer*, vol. 43, no. 13, pp. 3699–3705, 2002.

[31] A. B. Inceoglu and U. Yilmazer, "Synthesis and mechanical properties of unsaturated polyester based nanocomposites," *Polymer Engineering & Science*, vol. 43, no. 3, pp. 661–669, 2003.

[32] C. T. Sun, S. K. Chaturvedi, and R. F. Gibson, "Internal damping of short-fiber reinforced polymer matrix composites," *Computers & Structures*, vol. 20, no. 1–3, pp. 391–400, 1985.

[33] T. Lan, P. D. Kaviratna, and T. J. Pinnavaia, "On the nature of polyimide-clay hybrid composites," *Chemistry of Materials*, vol. 6, no. 5, pp. 573–575, 1994.

Hindawi Publishing Corporation
Journal of Nanomaterials
Volume 2006, Article ID 25467, Pages 1–4
DOI 10.1155/JNM/2006/25467

Study on the Effect of Nano-SiO_2 in ULSI Silicon Substrate Chemical Mechanical Polishing Process

Liu Yuling, Wang Juan, Sun Ming, and Liu Chenglin

Institute of Microelectronic Technique and Material, Hebei University of Technology, Tianjin 300130, China

Received 25 December 2005; Revised 7 September 2006; Accepted 21 November 2006

Both process and mechanical of silicon substrate chemical mechanical polishing (CMP) are studied in detail, and the effects of experiments designed indicate that nano-SiO_2 grinding particles seem to be acted as catalyzer besides the grinding action during the CMP process. This is different from the traditional function. As a result, in the condition of low pH, the nano-SiO_2 slurry can be recycled. In the meanwhile, the removal rate can gain stability and pH value does not change obviously.

1. INTRODUCTION

ULSI manufacturing technology develops rapidly to the higher integration, higher reliability, higher efficiency, and lower cost. Substrate area has been increasing. The wafers of 300-mm diameter have been produced in large scale. The development trend is 400 mm. Technical advances inspired the development of chemical mechanical polishing (CMP) for IC fabrication.

However, CMP has been widely recognized as the most promising technology for the planarization of multilayer structures in semiconductor manufacturing. In a typical CMP process, a wafer is rotated on its axis while being pressed face down by a carrier against a rotating polishing pad that is covered with slurry (Figure 1). A carrier film attaches the wafer to the carrier during the polishing. The relative motion of the wafer and pad, combined with the applied down force and chemical activity of the slurry, erodes features on the wafer. It is generally known that several process parameters including equipment and consumables (pad, backing film and slurry, etc.) can optimize and improve the CMP performance [1].

At present, for microelectronics development, it is key that the technology of lower roughness and lower cost in CMP processing. Chemical mechanical polishing process becomes the essential technique to achieve the sufficiently global and local planarization.

Chemical mechanical polishing (CMP) of single crystalline silicon (SCS) has been used for a long time in wafer manufacturing. At beginning, CMP of SCS is applied in thinning and it can create bondable surfaces in the manufacturing of bonded silicon-oninsulator (SOI) materials. Recently, the use of SCS CMP for other applications has emerged. CMP of SCS has been used for thinning in the formation of vertical integrated circuits and in realization of high aspect ratio silicon microstructures. Now, in ULSI manufacturing, silicon substrate is chosen for using more than 80%. CMP has shown the ability to planarize selectively grown collectors in processing bipolar transistors. CMP has been employed to remove epitaxially overgrown silicon in order to create fully isolated SOI islands. These new applications clearly motivate a further understanding of the process. Even though CMP of SCS has been used for a long time, not that many investigations on the process have been published [2].

To fabricate devices with high integration, high reliability, the CMP under alkaline condition must be used [3–8]. Up to now, the function of nano-SiO_2 is generally regarded as machinery grind function [9–13]. But as a matter of fact, during the CMP, the chemical combination reaction exists between nano-SiO_2 and silicon substrate [14]. That reaction must be studied deeply, which is helpful to obtain silicon substrate with high DP, low roughness, and high efficiency.

2. EXPERIMENT

2.1. Experimental object and experiment

In this experiment, we used ϕ 15 mm N-type $\langle 111 \rangle$ and $\langle 100 \rangle$ orientation silica wafer ($\rho = 8 \sim 14\,\Omega \cdot$ cm).

Firstly, silicon wafers must be grinded and cleaned before polishing, and then put the wafers on the carriers of the

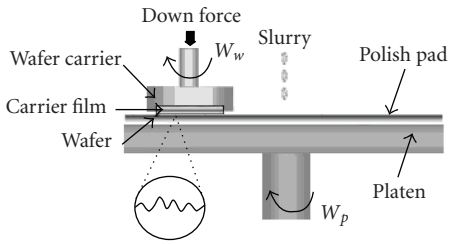

Figure 1: Typical CMP model.

SpeedFam I polisher. The polishing slurry used in the experiment is prepared with nano-SiO_2 colloid and kinds of chemical additives. Finally, the proper polishing pad and processing parameters are chosen to control polish process.

The slurry is silica sols contained oxidant, pH regulator, and other matters. The microtumble of SiO_2 particles acts on the wafer surface as mechanical grind, and the oxidant acts as chemical escharotics. Figure 2 shows the SEM of nano-SiO_2.

The CMP pad is made of a flexible microporous polyurethane material, which has elasticity and can be compressed. This peculiarity allows pad to absorb the slurry to contact with wafer sufficiently. In the experiment, Rodel CMP pad with groove is used.

Experiment

Measure the before-CMP thickness of wafers prepared above. With the same polisher and pad the wafer is polished. After polishing, the wafer should be cleaned, and then measure the post-CMP thickness.

Removal Rate (Rr/μm/h) = (before-CMP thickness—post-CMP thickness)/time.

2.2. Result and discussions

By the related CMP experiments containing the processing of same slurry ingredients, pad, and other parameters, changing the concentration of SiO_2, we achieved the relation curve of Rr versus concentration about Si⟨111⟩, N-type material. Figure 3 shows the removal rate (Rr) of different SiO_2 concentration for polishing slurry.

From Figure 3, it is known that the removal rate is extremely low, just to be less than 1 μm per hour, when the alkaline aqueous solution without silica sols is used. But when we add 4/10000 silica sols to alkaline aqueous solution, CMP removal rate is improved quickly. When the concentration of SiO_2 rises to 20 wt%, namely, its concentration increases by 500 times, to our surprise, its removal rate has not obviously increased.

It is well known that SiO_2 plays a mechanical abrasive role during the silicon substrate CMP with alkali slurry. The reaction is [15]

$$\mathrm{Si} + 2\mathrm{MOH} + \mathrm{H_2O} \longrightarrow \mathrm{M_2SiO_3} + 2\mathrm{H_2}\uparrow. \quad (1)$$

That does not accord with the experiment fact. The presence of the silica sols influences the removal rate greatly. The

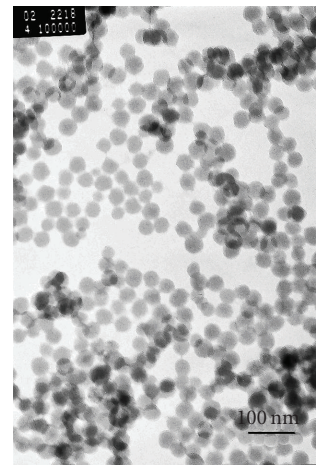

Figure 2: SiO_2 SEM.

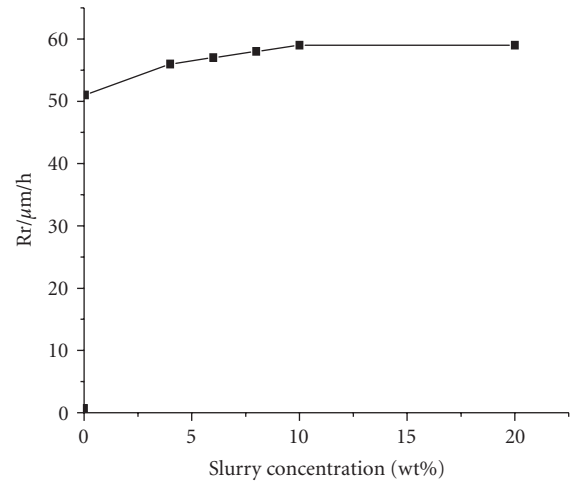

Figure 3: Rr versus concentration.

adding of 1/10000 silica sols can make the removal rate improve to 60–80 μm/h. Obviously, it is not only because silica sols improve the machinery effect of grind, but also the other influence.

To investigate further and to know the function of silica sols, we polish silicon wafer (N-type ⟨100⟩ and ⟨111⟩) circularly at the same condition, and the effects are shown in Figures 4–7.

Figures 4–7 show that as slurry recycles for polishing,

(1) pH drops to about 9.5 and reduces more than 1 pH value slowly from 10.90,
(2) the removal rates of ⟨111⟩ and ⟨100⟩ wafer keep stable in 1.1 μm/min and 1.4 μm/min.

But if its chemical reaction is followed (1) in the course of CMP, it will consume a large amount of alkali, which makes pH reduce quickly. For example, in the condition of pH = 10, pH should reduce rapidly during CMP and the removal

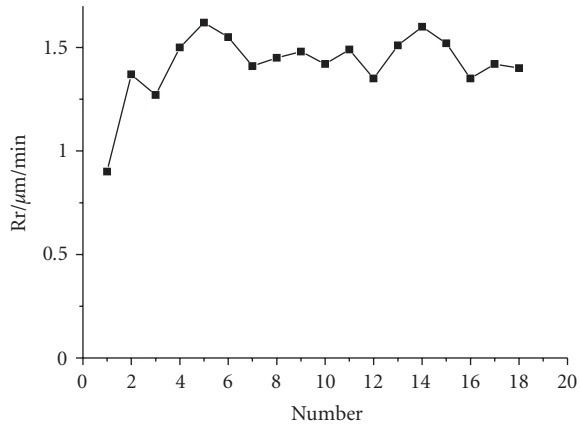

Figure 4: ⟨100⟩ Rr versus number.

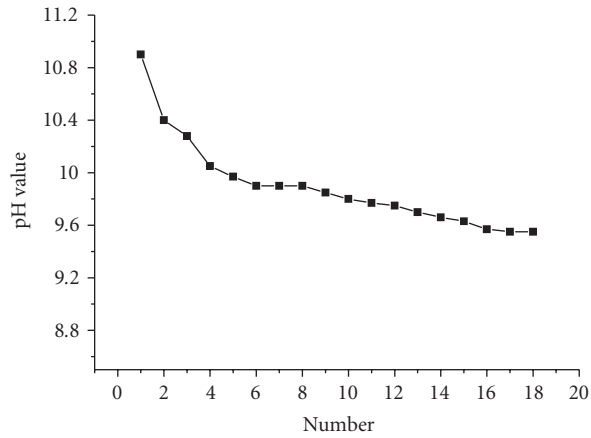

Figure 5: ⟨100⟩ pH versus number.

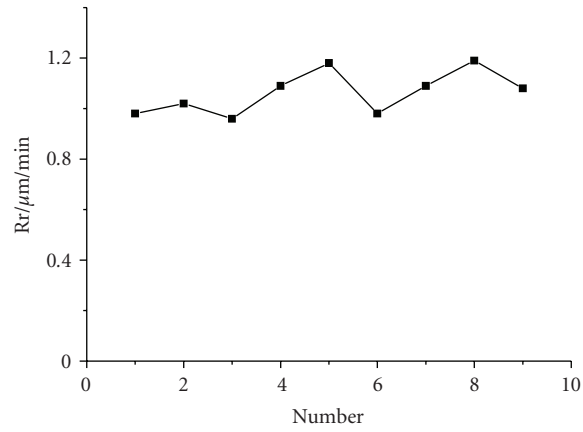

Figure 6: ⟨111⟩ Rr versus number.

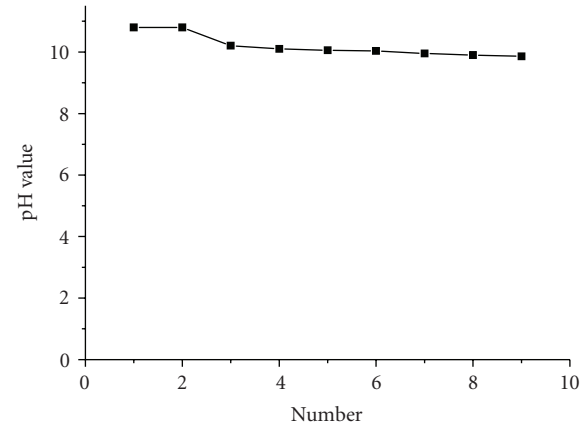

Figure 7: ⟨111⟩ pH versus number.

rate should be reduced rapidly. However, the fact is that pH changes slightly. So the reaction equation (1) is not the main reaction in experiment. There must be other reactions that be presumed as follows:

$$\mathrm{Si} + \mathrm{SiO_2} \xrightarrow{\text{high pressure } \mathrm{OH^-}} 2\mathrm{SiO}, \quad (2)$$

$$2\mathrm{SiO} + \mathrm{O_2} \longrightarrow 2\mathrm{SiO_2}. \quad (3)$$

General reaction ((2) + (3)) is

$$\mathrm{SiO_2} + \mathrm{Si} + \mathrm{O_2} \xrightarrow{\text{high pressure } \mathrm{OH^-}} 2\mathrm{SiO_2}. \quad (4)$$

Reaction (2) goes on the force and relative movement between the surfaces of the abrasive and the substrate. Thus, the chemical reaction produces SiO that seems to be extremely unstable and can be oxidized by oxygen of environment rapidly. Then SiO turns into steady SiO_2, and SiO_2 is grown into SiO_2 micelle, some SiO_2 or SiO_2 micelle top layer form a layer, which attracts some OH^- [16, 17] and makes pH reduce to some extent. Reactions (2) and (3) show the essence that SiO_2 accelerate chemical reaction and pH changes little but reaction rate keep high for a long time. But the general reaction (4) shows that Si is oxidized to SiO_2. A large amount of SiO_2 in the slurry does catalysis at the beginning stage. The discovery of the reaction law above has meaningful guidance to CMP process. According to it, in Hebei University of technology, professor Liu Yuling invents a series of CMP polishing slurries with little particle size, fast removal rate, low roughness, and scale application.

3. CONCLUSIONS

This study is to investigate and verify the function of silica sols in the CMP processing. By the analysis of experiments, we draw the conclusion that SiO_2 gel particles take on effect as mechanical abrasive agent and as catalytic effect as well, and the subsurface damage of silicon wafer has not yet been found in experimental results and therefore the CMP process of silicon wafers by soft abrasives has great potential to be developed into a green or environment-friendly technology in IC fabrication.

REFERENCES

[1] N.-H. Kim, P.-J. Ko, G.-W. Choi, Y.-J. Seo, and W.-S. Lee, "Chemical mechanical polishing (CMP) mechanisms of thermal SiO_2 film after high-temperature pad conditioning," *Thin Solid Films*, vol. 504, no. 1-2, pp. 166–169, 2006.

[2] M. Forsberg, "Effect of process parameters on material removal rate in chemical mechanical polishing of Si(1 0 0)," *Microelectronic Engineering*, vol. 77, no. 3-4, pp. 319–326, 2005.

[3] L. Yuling, et al., "Micro-Electronics Tech-Engineering—Materials,Technics, Test. Electronics," Industry Publishing, 2004.

[4] T. Zhiyi, "CMP Technology Actuality and development trend," Semi-conductor transaction. 2002.

[5] J. J. Vlassak, "A model for chemical-mechanical polishing of a material surface based on contact mechanics," *Journal of the Mechanics and Physics of Solids*, vol. 52, no. 4, pp. 847–873, 2004.

[6] Y.-J. Seo, S.-Y. Kim, Y.-O. Choi, Y.-T. Oh, and W.-S. Lee, "Effects of slurry filter size on the chemical mechanical polishing (CMP) defect density," *Materials Letters*, vol. 58, no. 15, pp. 2091–2095, 2004.

[7] L. Yuling, K. Zhang, F. Wang, and W. Di, "Investigation on the final polishing slurry and technique of silicon substrate in ULSI," *Microelectronic Engineering*, vol. 66, no. 1–4, pp. 438–444, 2003.

[8] W. Di, Y. Ming, and L. Yuling, "Study on polishing slurry for silicon substrate in ULSI," *Journal of Shijiazhuang Railway Institute*, vol. 16, no. 4, pp. 38–41, 2003.

[9] T. Baimei, L. Yuling, and L. Jun, "Chemical mechanical polishing of silica dielectric in ULSI manufacturing," *Journal of Hebei University of Technology*, vol. 30, no. 3, pp. 32–36, 2001.

[10] W. Hongying, L. Yuling, and Z. Dechen, "A new type of copper CMP slurry in ULSI," *Chinese Journal of Semiconductors*, vol. 23, no. 2, pp. 217–221, 2002.

[11] L. Ren, "Semi-conductor cleaning technology," *Semi-Conductor Technology*, vol. 9, pp. 44–47, 2003.

[12] T. Baimei, L. Yuling, and L. Weiwei, "Analysing and researching on ULSI Silicon Substrate Cleaning technology," 2000.

[13] C. Zhou, L. Shan, J. R. Hight, S. Danyluk, S. H. Ng, and A. J. Paszkowski, "Influence of colloidal abrasive size on material removal rate and surface finish in SiO_2 chemical mechanical polishing," *Lubrication Engineering*, vol. 58, no. 8, pp. 35–41, 2002.

[14] E. Taran, B. C. Donose, I. U. Vakarelski, and K. Higashitani, "pH dependence of friction forces between silica surfaces in solutions," *Journal of Colloid and Interface Science*, vol. 297, no. 1, pp. 199–203, 2006.

[15] Y. Chen, Z. Chen, X. Li, and A. Chen, "Material removal mechanism and model in chemical mechanical polishing of silicon wafers," *Lubrication Engineering*, no. 4, pp. 119–122, 2006.

[16] K.-L. Zhang, Z.-T. Song, J.-X. Zhang, B.-M. Tan, and L. Yuling, "Study on preparation and application of silica sol nano-abrasive with large particle for CMP of dielectric in ULSI," *Chinese Journal of Electron Devices*, vol. 27, no. 4, pp. 556–558, 563, 2004.

[17] L. Yuling, K. Zhang, F. Wang, and Y. Han, "Study on the cleaning of silicon after CMP in ULSI," *Microelectronic Engineering*, vol. 66, no. 1–4, pp. 433–437, 2003.

Hindawi Publishing Corporation
Journal of Nanomaterials
Volume 2006, Article ID 58648, Pages 1–9
DOI 10.1155/JNM/2006/58648

Microstructure and Thermomechanical Properties of Polyimide-Silica Nanocomposites

A. Al Arbash, Z. Ahmad, F. Al-Sagheer, and A. A. M. Ali

Department of Chemistry, Faculty of Science, Kuwait University, P.O. Box 5969, Safat 13060, Kuwait

Received 13 February 2006; Revised 15 June 2006; Accepted 13 November 2006

Novel polyimide-silica nanocomposites with interphase chemical bonding have been prepared using the sol-gel process. The morphology, thermal and mechanical properties were studied as a function of silica content and compared with the similar composites having no interphase interaction. The polyimide precursors, polyamic acids (PAAs) with or without pendant hydroxyl groups were prepared from the reaction of pyromellitic dianhydride with a mixture of oxydianiline and 1,3 phenylenediamine or 2,4-diminophenol in dimethylacetamide. The PAA with pendant hydroxyl groups was reacted with isocyanatopropyltriethoxysilane to produce alkoxy groups on the chain. The reinforcement of PAA matrices with or without alkoxy groups on the chain was carried out by mixing appropriate amount of tetraethoxysilane (TEOS) and carrying out its hydrolysis and condensation in a sol-gel process. Thin hybrid films were imidized by successive heating up to 300°C. The presence of alkoxy groups on the polymer chain and their cocondensation with TEOS developed the silica network which was interconnected chemically with the polyimide matrix. SEM studies show a drastic decrease in the silica particle size in the chemically bonded system. Higher thermal stability and mechanical strength, improved transparency, and low values of thermal coefficient of expansion were observed in case of chemically bonded composites.

1. INTRODUCTION

Composites where nanoscale inclusions are imbedded within matrix material have attracted increasing research attention in recent years. Reviews on such composites using nanoclays [1, 2], nanotubes [3, 4], and inorganic networks [5–7] are available in literature. The inorganic networks are usually prepared by the sol-gel process [7, 8] to synergistically combine the properties of organic polymers (e.g., toughness, ductility, and processability) with that of ceramic materials (e.g., heat resistance, low thermal expansion, and retention of mechanical properties at high temperatures) [9, 10].

Polyimides (PIs) are extensively used in microelectronics and aerospace industries owing to their excellent thermal, mechanical, and dielectric properties [11]. However, PIs exhibit relatively high value of water absorption and the coefficient of thermal expansion, which can limit their application in the field of electronics. Composites from PIs and silica offering favorable properties of the both are therefore in great demand and further improvement in these can be achieved by bringing the dispersion of reinforced inorganic material to nanolevel in the matrix. The compatibility between PIs and silica generated in the sol-gel process using different tetraalkoxy silanes in the hybrids, however, is not as good as expected because of weak interactions between the pure organic and inorganic phases [12]. Tendency of the silica network to agglomerates into large particles at higher silica loading ultimately leads to phase separation. Since the morphology of two-phase systems affects the mechanical properties of polymer hybrids, attempts have been made to improve the compatibility between PIs and silica by increasing interfacial interactions. Wang et al. [13, 14], Schrotter et al. [15] Chen and Iroh [16], Xenopoulos et al. [17], Musto et al. [18], and Chang et al. [19] have used different organosilanes with tetraalkoxysilane to produce silica network in the PI matrix. The organic groups present on these silanes, for example, aminophenyl-trimethoxysilane, aminopropyltrimethoxysilane, diaminophenyltetramethyl-disiloxane, glycidyloxy-propyltrimethoxysilane, aminopropylmethyl-diethoxysilane, and diaminopropyltetramethyl-disiloxane, are supposed to interact with organic PAA chain and alkoxy groups during the sol-gel process become the part of the silica network.

Present authors [20, 21] have found that the introduction of hydroxyl groups on the backbone of polymer chain can have a positive effect through physical or chemical

interactions between organic and inorganic components. The morphology of silica particle produced in such matrices is totally different and particle size is much smaller for the same silica contents as compared to simple matrix without hydroxyl groups and this has a positive influence on the thermal and mechanical properties of the resulting hybrids.

The reaction of hydroxyl groups on the polymer chain, however, is very slow with the alkoxy groups of TEOS and in the sol-gel process usually a physical bonding between the matrix and the silica network can be achieved. Also the Si−O−C bonds formed by the reaction of hydroxyl groups on the polymer chain and the alkoxy groups from the silane during the sol-gel process are considered very weak. In the present work, the PAA chains containing pendant hydroxyl groups synthesized from the reaction of pyromellitic dianhydride (PMDA) with a mixture of oxydianiline (ODA) and 2,4-diminophenol (2,4-DAP) were reacted with isocyanatopropyltriethoxysilane (ICTEOS) to produce pendant alkoxy groups on the chain. The number of pendant alkoxy groups on PAA chain could be varied by changing the proportion of 2,4-DAP in the total diamine content in the reaction mixture. The reaction of isocyanato group with the −OH group leading to a polyurethane linkage is considered as very fast. On addition of an appropriate amount of TEOS, the sol-gel process was carried out to produce an extensively bonded silica network in the matrix. Phase compatabilization to reduce the agglomeration tendencies in the inorganic phase is thus achieved by chemical reaction between the matrix having alkoxy groups and those of TEOS. The PAA with no hydroxyl groups on the chain was prepared by the reaction of a mixture of 1,3-phenylenediamine (1,3-DAB) and oxydianiline (ODA) in dimethylacetamide (DMAc) with equimolar amount of pyromellitic dianhydride (PMDA) and this acts as control system. The resulting hybrid films in both cases were imidized. The morphology, thermal stability, visco-elastic and thermal mechanical properties of the PI-silica hybrid films were studied and related with the amount of silica and the extent of chemical bonding between the organic and inorganic phases.

2. EXPERIMENTAL

2.1. Materials

The monomers used to synthesize the polyimide were pyromellitic dianhydride (PMDA), 4,4′-oxydianiline (ODA), 1,3-diaminobenzene (1,3-DAB). These monomers and tetraethoxysilane (TEOS), triethylamine (TEA), were of ananlytical grade obtained from Aldrich. The solvent anhydrous DMAc (water contents ≥ 0.05 wt%) kept over molecular sieve was obtained from Aldrich. Diaminophenol-dihydrochloride (2, 4-DAP·2HCl) was obtained from Fluka and it was purified to remove HCl from the salt using TEA. The 2,4 DAP was copolymerized with ODA to produce PAA chain with hydroxyl groups. The isocyanatopropyltriethoxysilane (ICTEOS) 95% pure used as coupling agent was obtained from ABCR Germany and used as such. All other chemicals and regents were of AR grade and used without further purification except 2,4-DAP·2HCl.

2.2. Preparation of the hybrid films

2.2.1. Preparation of PAA solution

For the preparation of PAA without pendant hydroxy groups on the chain, a mixture of ODA and 1,3-DAB, (0.025 mol) in molar ratio 95 : 5; respectively, was placed into a 250 quickfit flask and dissolved by stirring in 170 g of anhydrous DMAc as solvent. PMDA, (0.025 mol) was added into it under complete anhydrous conditions. The viscosity increased quickly over the next one hour, and the reaction was allowed to proceed at room temperature for 24 hours to ensure a complete reaction.

2.2.2. Preparation of the PAA solution with pendant alkoxy groups

In order to prepare PAA with hydroxy groups on the chain, 1,3-DAB was replaced with 2,4-DAP in the PAA synthesis. As only the salt of this compound was available, it was purified as follows: in a 100 ml glass bottle, 0.254 g of 2,4-DAP·2HCl (1.25 milli mol) was taken. Stoichiometric amount of TEA was added to neutralize HCl completely. About 10 g DMAc was then added to the mixture. The mixture was stirred for few minutes and finally filtered under vacuum to remove the precipitates of triethyl ammonium hydrochloride. To this solution of 2,4-DAP, 4.853 g of ODA (23.75 milli mol) and 160 g of solvent were added and stirred thoroughly for complete dissolution. An equimolar amount of PMDA (5.622 g, 0.025 mol) was added to react with the diamines. The reaction mixture was stirred for additional 24 hours to ensure complete reaction. The inherent viscosities of the PI solutions at 25°C were in the range 2.1–2.33 dL/g. Two types of PAA solutions were prepared, one with 5 and other with 10 mole percent of hydroxy amine. The coupling agent ICTEOS was added to the prepared PAA solutions in equimolar amount with 2,4-DAP, that is 5% (or in double amount 10%) by mol and the mixture was stirred at 50°C for 2 hours.

2.2.3. Sol-gel processing and imidization reaction

Silica network was produced in the above polymer solutions by carrying out the sol-gel process. A measured amount of TEOS was added to the polymer precursor solution with continued stirring until the solution became homogenous. A stoichiometric amount of water as 10 wt% 0.1 N HCl solution in DMAc was then added. The stirring continued for 4 hours at 60°C. Hybrids with various silica contents ranging from 5–40 wt% were prepared and the films (thickness varying from 0.08 to 0.10 mm) were cast by solvent elution at 70°C. These hybrid films were heated for 1 hours at 100°C, 1 hours at 200°C, 0.5 hours at 270°C, and 1 hours at 300°C in sequence to carry out the imidization process [12]. The silica network formation simultaneously took place with the imidization process.

The hybrids from the PI matrix without hydroxyl groups are referred to as PISi-T and those with hydroxyl groups having 5% 2,4-DAP mixed with 5% by mol ICTEOS as PISi-P5-I-T while those hybrids containing 10% 2,4-DAP mixed

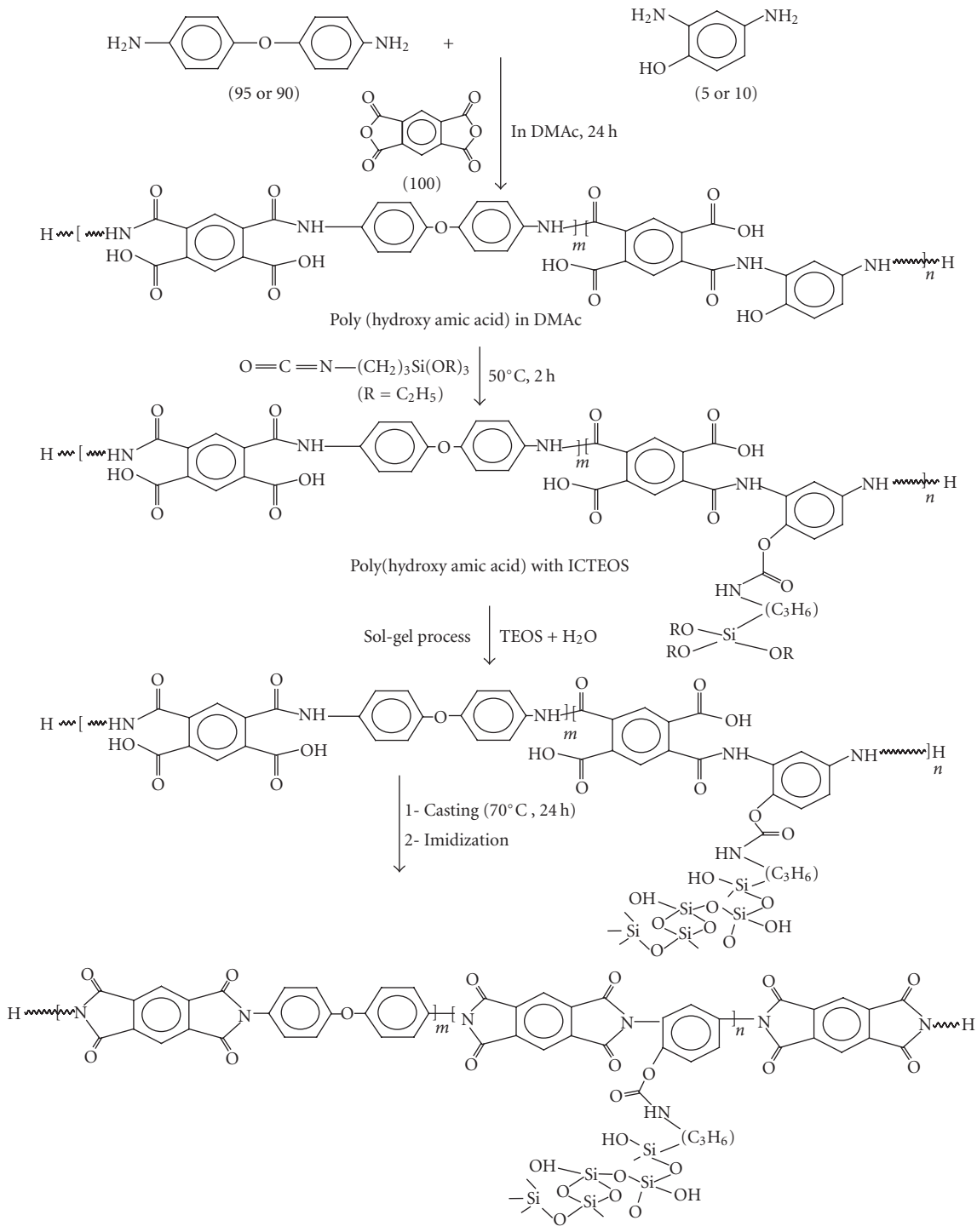

Figure 1: Synthesis of chemically bonded polyimide-silica hybrids.

with 10% by mol ICTEOS are referred to as PISi-P10-I-T. The flow sheet diagram describing the preparation of chemically bonded hybrids is given in Figure 1.

2.3. Measurements

The imidization process and the silica network formation in the hybrid films were monitored by the FTIR spectroscopy using a Perkin-Elmer FTIR 2000 spectrophotometer. FTIR analysis was also used to confirm the formation of chemical bonds between the organic matrix and the silica network. For scanning electron microscopy (SEM), the brittle-fractured films were sputter coated with gold by means of Balzer's SCD-50 sputter coater and then examined by JSM-630 Joel scanning electron microscope operated at 20 kV.

Dynamic mechanical analysis (DMA) was used to measure α-relaxation temperature associated with the glass

transition and the temperature variation of storage modulus of the hybrid material. These measurements were performed under tension mode in the temperature range 100–500°C at 5°C/min ramp using a frequency of 5 Hz under inert atmosphere on a DMA Q-800 (TA, USA).

Thermal mechanical analysis to measure the linear coefficient of thermal expansion was performed on Schimadzu TMA-50 at a heating rate of 10°C/min with an applied load of 4.00 g under nitrogen gas. Thermogravimetry (TG) was performed on approximately 10 mg of the sample from ambient to 800°C at a heating rate of 10°C/min in a dynamic synthetic air atmosphere (30 ml/min), using TGA-50 Shimadzu automatic analyzer.

3. RESULTS AND DISCUSSION

The solutions of the polyamic acid-silica mixtures after the sol-gel process and prior to the film casting were homogeneous in all cases. In the case of PISi-T system, the hybrids films up to 10 wt% silica were transparent and brownish yellow, and those with more than 20% silica were opaque and dark brown in color. In the case of PISi-P5-I-T and PISi-P10-I-T hybrids, films up to 20 wt% silica loading were transparent and dark brown in color. Those with 30–40 wt% silica were semi-transparent and dark brown in color. The optical transparency of the films thus increased as the chemical interaction between the phases reduced the tendency of silica particle to agglomerate. The hybrid films remain transparent so far as the size of these particles is less than the wavelength of light and become opaque when their size increases.

3.1. FTIR spectroscopy

The curing of PAA to PI and the reaction of the pendant hydroxyl groups with the ICTEOS were monitored by FTIR spectroscopy. In case of PAA, the broad band around 1660 cm^{-1}, called amide I mode, involves contributions from C=O stretching, C−N stretching, and C−N−C deformation vibrations. A band at 1570–1540 cm^{-1}, known as amide II mode, is a mixed contribution of N−H in plane bending, the C−N stretching, and C−C stretching vibrations. The amide I and amide II disappeared entirely after the thermal imidization, and new strong absorption bands at 1777–1782, 1722–1730, and 1377–1380 cm^{-1} due to the asymmetric stretching of C=O, symmetric stretching of C=O, and symmetric stretching of C−N, respectively, which are assigned to the imide ring [22]. Appearance of these characteristic absorption bands confirms the curing of PAA to PI. The appearance of absorption peaks at 1100 and 830 cm^{-1} in the IR spectra of PISi-P10-IT and PISi-T meant the formation of silicon-oxygen bonds, that is, the silica network. The FTIR absorption spectra have been explained elsewhere [23] and details are not provided in the present work.

In order to find whether the ICTEOS reacted with the hydroxyl groups on PAA, we subtracted the absorption spectrum obtained after imidization in case of films where ICTEOS was added to hydroxy PAA film (PI-P10-I) from the hydroxy PAA film (PI-P10). This spectrum is shown in Figure 2. The absence of absorption in the region 2250 cm^{-1} due to isocyanto groups and appearance of urethane linkage at 1743 cm^{-1} show that ICTEOS has reacted (see Figure 1) with the pendant hydroxyl groups on the polymer chain. The absorption in the region 2840–2920 cm^{-1} and at 1234 cm^{-1} due to $-CH_2-CH_2-$ linkage and Si−C bonds, respectively, further confirms that ICTEOS has become the part of polymer chain. The presence of small peaks at 1179 cm^{-1} and at 971 cm^{-1} shows the presence of Si−O−R linkages, that is, the alkoxy groups of the ICTEOS. As the sol-gel process was not carried out with these experimental systems, purely made for FTIR analysis, so these groups remain partially unhydrolyzed/uncondensed in the matrix. The above results clearly show the successful binding of ICTEOS on the polymer chain which could further link the silica network with the matrix.

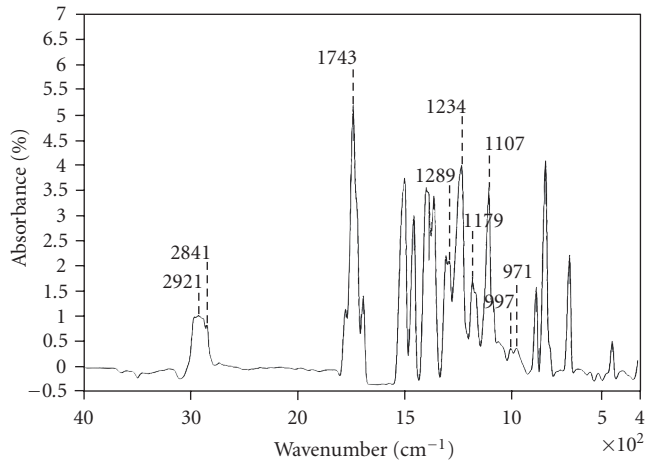

Figure 2: Normalized FTIR spectrum showing the absorption due to chemical linkages from ICTEOS with the matrix.

3.2. Morphological studies

The scanning electron micrographs showing the effect of silica loading and reinforcement binding with matrix on the morphology of the resulting hybrids are given in Figure 3. The micrographs in Figures 3(a) and 3(b) show the morphology of the unbonded hybrids with 20 and 40 wt% of silica, respectively, in the matrix. The silica particles are seen as white beads with round or oval shape and sharp boundaries. The average diameter of the particles increased from 0.2 to 8 micrometers as the silica contents were increased from 5 to 40 wt%. The sharp, clear boundaries of the silica particles with some interfacial spaces show that the pure organic and inorganic phases had poor interaction and as the silica loading increased the tendency towards phase separation increased. The micrographs in Figures 3(c) and 3(d) show the morphology of the PISi-P5-I-T hybrids with 20 and 40 wt% silica loading, respectively, in the matrix. Though with increased silica loading, the tendency of the particle size to increase remains there, however, there was a considerable

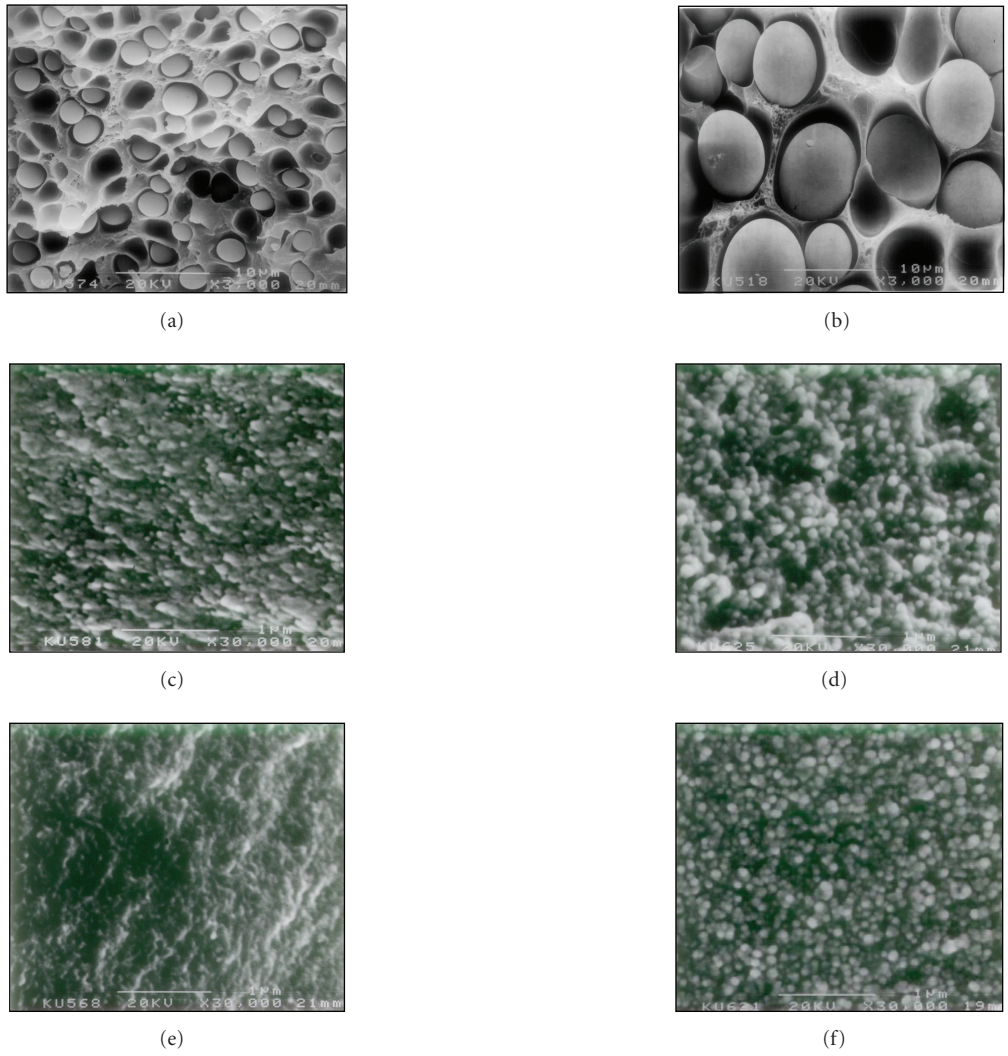

Figure 3: Scanning electron micrographs for the polyimide silica hybrids with 20 wt% silica loading; (a) PISi-T, (c) PISi-P5-I-T, (e) PISi-P10-I-T 40 wt% silica loading; (b) PISi-T, (d) PISi-P5-I-T, (f) PISi-P10-I-T.

decrease in the particle size as compared to the unbonded hybrids. The diameter of the silica particles varied from 10 nm to 200 nm in these hybrids for silica loading varying from 5 to 40 wt%, respectively. The bonded hybrid system displayed a more adhesive interface between enforcement and the matrix thus leading to a homogenous distribution of silica particles and retarding their phase separation from the matrix. The micrographs in Figures 3(e) and 3(f) show the morphology of PISi-P10-I-T hybrids. As seen from these graphs, the increased extent of binding between the phases has further reduced the particle diameter which varies from 5–100 nm for the similar silica loading as stated above. The presence of alkoxy groups on the PI matrix and their co-condensation with TEOS to produce silica network during the sol-gel process has retarded the tendency of silica network to agglomerate into large particles thus reducing their size to nanolevel and making the distribution of the inorganic network more homogenous. The finer silica particles in the matrix with enhanced adhesion between the phases which improved the transparency of the hybrid films can also have great influence on the thermal mechanical properties of the hybrid material.

3.3. Visco-elastic properties

The temperature variation of storage modulus (E′) and tan δ (where tan δ is the loss factor related to the ratio of loss modulus to storage modulus) for the three hybrid systems studied is shown in Figures 4–6. The visco-elastic data have been given in Table 1. Incorporating silica in the matrix increased the storage modulus and high temperature reliability of the PI. Table 1 gives the values of storage modulus for different silica contents at two different temperatures for the studied hybrid systems. The increase in the modulus values as compared to the pure polymer is more in case of bonded hybrids.

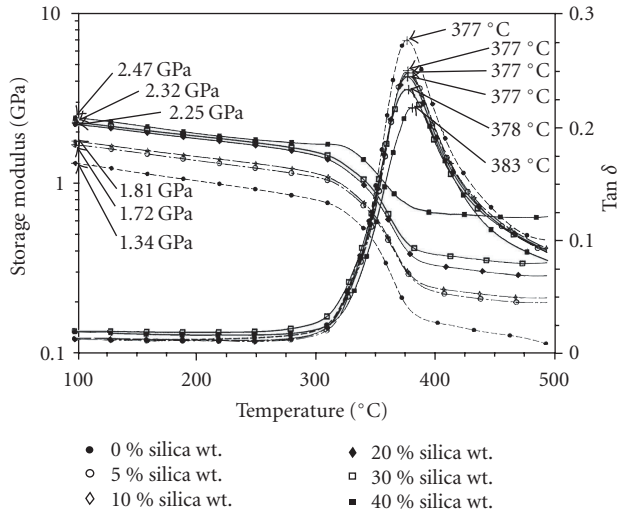

Figure 4: Temperature dependence of storage modulus and tan delta for the PISi-T hybrids; silica wt%: 0 (•), 5 (◦), 10 (◊), 20 (♦), 30 (□), 40 (■).

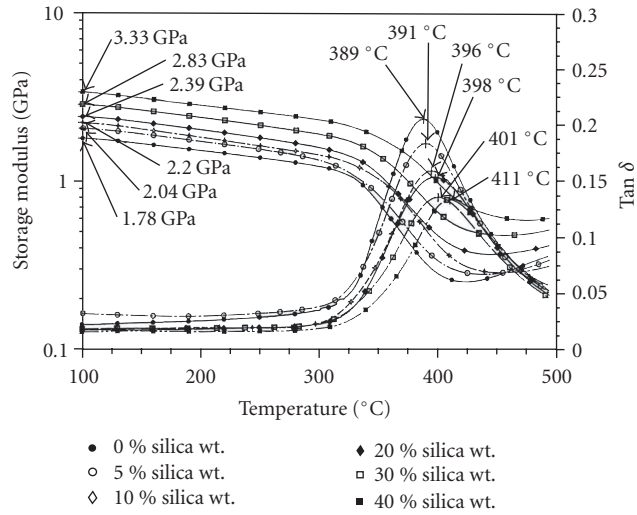

Figure 5: Temperature dependence of storage modulus and tan delta for the PISi-P5-I-T hybrids; silica wt%: 0 (•), 5 (◦), 10 (◊), 20 (♦), 30 (□), 40 (■).

It also depends on the degree of interphase bonding and the values obtained are higher in PISi-P10-I-T hybrids as compared to PISi-P5-I-T system (Table 1). As the temperature is increased, the modulus drops to about an order of magnitude in the rubbery region in case of pure PI. The modulus decreases linearly with temperature up to about 340°C and at T_g a rapid decrease in E′ is witnessed. The hybrid samples with different silica contents all have higher E′ values in the rubbery region as compared to the pure PI. The rate of decrease of E′, however, is considerably lower with large silica loading. The chemically bonded hybrids tend to retain the modulus values at higher temperature above 425°C than as compared to the unbonded system (Table 1).

The magnitude of the tan δ curves decreases with increasing the amount of silica (Figures 4–6). This suggests that the mobility of the polymer chains is restricted due to presence of silica in the matrix and the material show more elastic behavior as the tendency to viscous flow behavior is reduced. A comparison of the variation of tan δ with temperature for the unbonded and bonded hybrids shows that the bonded hybrids have much lower values of tan δ for the similar silica loading. The T_g associated with α-relaxation measured from the maxima of the tan δ curve (Table 1) for the unbonded hybrids with 40 wt% silica shows an increase of 5°C from the pure PI (Figure 4). The peak temperature of tan δ is shifted slightly to higher temperature with increasing silica. On the other hand, for the PISi-P5-I-T hybrids an increase of about 22°C in the T_g was observed with increasing silica contents from zero to 40 wt%. As the number of hydroxyl groups on the PI chains was increased, the T_g of the pure matrix was also shifted to the higher temperature. This is due to intermolecular bonding of the polymer chain due to presence of polar groups. The T_g recorded for the pure polymer used in case of PISI-P10-I-T hybrids was 403°C. The maximum value of 422°C was recorded in this case with 40% silica in-

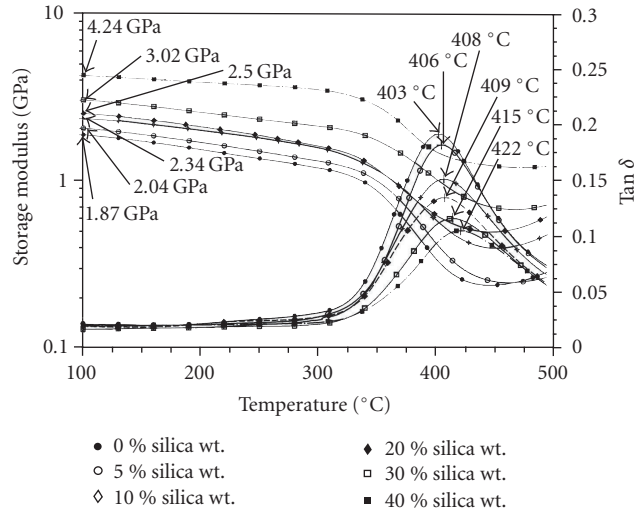

Figure 6: Temperature dependence of storage modulus and tan delta for the PISi-P10-I-T hybrids; silica wt%: 0 (•), 5 (◦), 10 (◊), 20 (♦), 30 (□), 40 (■).

clusion in the matrix (Figure 6). The large reduction in the tan δ curves and increase in T_g (Figure 7) for these hybrids can be attributed to the strong interaction/presence of covalent bonding between PI and silica. The Interfacial interaction also reduces the tendency of network structure to agglomerate into large silica particles which are reduced to almost nanolevel. These particles have high surface to volume ratio. More surface area available to bond/absorb the polymer chains for given silica content make the polymer chains stiffer. This also explains why the bonded hybrids with finer morphology had higher modulus values than that of the unbonded hybrids for the similar silica loading.

Table 1: Viscoelastic properties of polyimide-silica hybrids.

SiO_2 (wt %)	Storage modulus (GPa) at 100°C			Storage modulus at 425°C			T_g (°C)			Tan delta (δ)		
	PISi	PISi-P5-I-T	PISi-P10-I-T	PISi	PISi-P5-I-T	PISi-P10-I-T	PISi	PISi-P5-I-T	PISi-P10-I-T	PISi	PISi-P5-I-T	PISi-P10-I-T
0	1.34	1.83	1.87	0.13	0.25	0.25	376.60	388.98	403.29	0.28	0.21	0.19
5	1.72	2.04	2.04	0.20	0.28	0.29	377.38	390.64	405.09	0.25	0.18	0.16
10	1.81	2.20	2.34	0.23	0.31	0.43	377.77	395.52	407.80	0.25	0.16	0.15
20	2.25	2.39	2.50	0.31	0.38	0.51	377.28	398.17	408.51	0.25	0.15	0.13
30	2.32	2.83	3.02	0.32	0.51	0.78	378.16	401.41	415.46	0.23	0.13	0.11
40	2.48	3.33	4.24	0.33	0.72	1.28	383.45	411.47	422.15	0.23	0.13	0.10

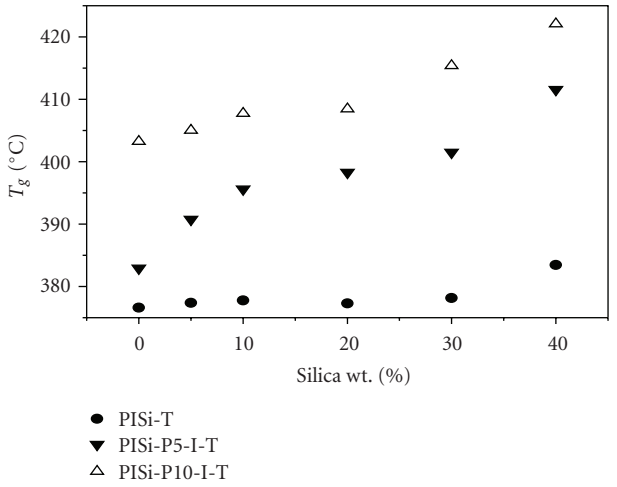

Figure 7: Variation of glass transition with silica content in polyimide-silica hybrids: PISi-T (•), PISi-P5-I-T (▼), PISi-P10-I-T (△).

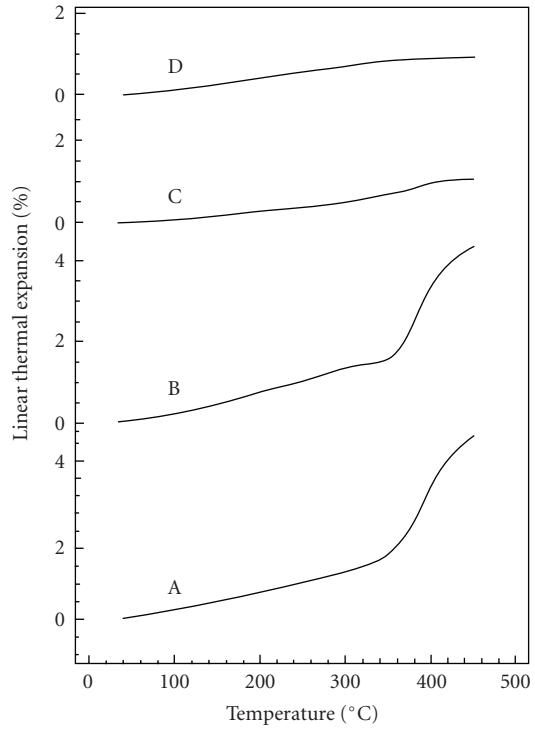

Figure 8: Variation of linear thermal expansion with temperature for (A) polyimide, (B) hydroxy-polyimide, (C) PISi-P5-I-T hybrids with 40 wt% silica, (D) PISi-P10-I-T hybrids with 40 wt% silica.

3.4. Thermal mechanical analysis

Figure 8 shows linear thermal expansion for pure PI, hydroxy PI and the chemically bonded PI-silica hybrids as function of temperature. The value of coefficient of thermal expansion for the pure PI is 52.1 ppm/°C at 50°C. The average value in the temperature range of 50–300°C was measured as 61.42 ppm/°C. Beyond this temperature softening of the polymer chain may be taking place. Our value is in agreement with the values of 55 ppm/°C reported by Yano et al. [24] at 150°C and 48.5 ppm/°C reported by Southward et al. [25] at 50°C. The reduction in the CTE value of PI was observed with the introduction of hydroxyl groups on the chain and the average value for the hydroxyl PI was 56.88 ppm/°C. In case of hybrid film PISi-P5-I-T with 40 wt% silica, the CTE values were reduced to 24.03 ppm/°C. Also the softening point is increased to higher temperature. The CTE of hybrid materials is dependent upon matrix, type of reinforcement, and volume fraction of the reinforcement and interaction between the phases. In case of PiSi-P10-I-T hybrids where there is more bonding between the matrix and the silica network, the average CTE value recorded was 20.46 ppm/°C. PIs are commonly used in microelectronic industry as interlayer dielectrics for thin film wiring in multichip packages. To meet the stringent demands of industry, the material properties such as CTE has to be controlled precisely. Most of the low dielectric PIs have undesirable high values of CTE which may result in fatal damage from thermal stresses generated due to the mismatch between the semiconductor chip and insulating PI. Such hybrids material therefore can be extremely useful in such applications requiring a controlled CTE.

3.5. Thermal stability

The TGA thermograms of the three hybrid systems, PISi-T, PISi-P5-I-T, and PISi-P10-I-T with various silica contents,

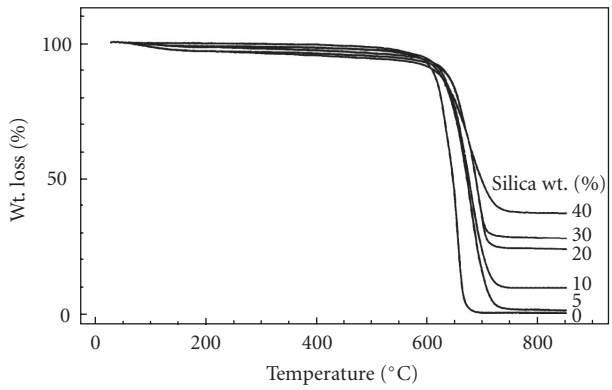

Figure 9: TGA thermograms for the PISi-T hybrids with various silica contents.

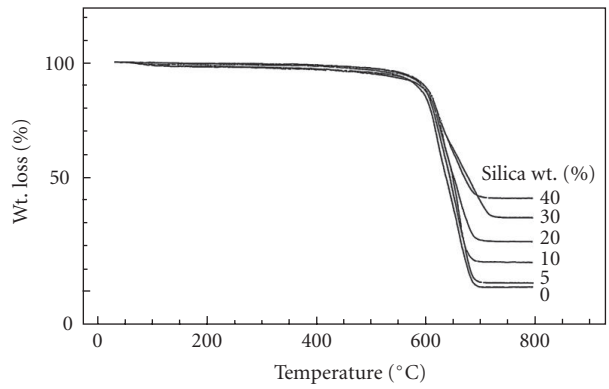

Figure 10: TGA thermograms for the PISi-P5-I-T hybrids with various silica contents.

are shown, respectively, in Figures 9, 10, and 11. The decomposition temperature of the pure PI was around 650°C. Slight decrease in the weight at lower temperature for the hybrids could be due to the loss of by-products (H_2O, EtOH) from the condensation reaction of the silica network. The hydroxy PI used for preparing the bonded hybrids show slightly higher thermal decomposition temperature than the PI used for the unbonded hybrids. It seems that the presence OH groups on the polymer chain act as free radical quencher during the oxidative degradation process. As the amount of silica is increased in the matrix, the thermal decomposition behavior shows a gradual weight loss with increasing temperature up to 770°C. The effect is more pronounced in the hybrids where higher silica loading have been used in the matrix. Since the formed silica network exhibits good thermal stability even at 800°C, the weight loss of the hybrids is resulting mainly from the PI matrices. It seems that the polymer chains absorbed or trapped in the network are protected from thermo-oxidative process and this hinders the process of degradation. The PI hybrids therefore show slightly better thermal stability as compared to the matrix. The weight retained above 770°C in all the hybrids was found proportional

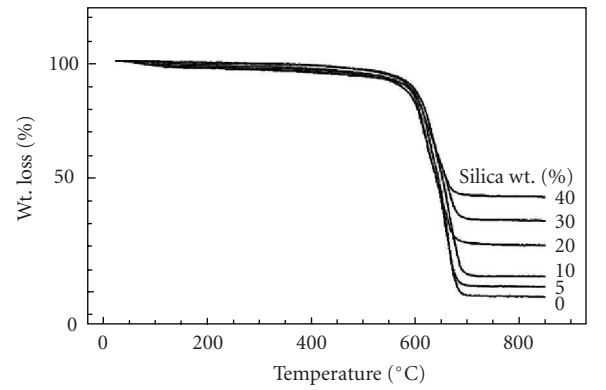

Figure 11: TGA thermograms for the PISi-P10-I-T hybrids with various silica contents.

to the silica contents used in the matrix, meaning thereby that the sol-gel process was carried out almost completely in the present studies.

4. CONCLUSIONS

The present studies on PI-Silica hybrids show that interphase chemical links between the silica network and the polymer chain prevent the agglomeration of silica particles, reduce the particle size to nanolevel thus making their distribution more homogenous in the matrix. The improved interfacial interaction between the phases enhances the mechanical strength particularly at high temperatures. The glass transition temperature of the polymer is increased more with addition of silica in these systems as compared to the one where no bonding exists between the phases. The values of coefficient thermal expansion are greatly reduced and thermal stability of the material is enhanced. Chemically bonded polyimide-silica nanocomposites thus show better mechanical and thermal properties.

ACKNOWLEDGMENTS

The authors express their appreciation to the Faculty of Graduate Studies, Kuwait University (KU) for providing financial support. The authors acknowledge the Research Administration of KU for the grant under Project SC 07/01. The technical support from the EM unit (Project GS 03/01) and the general facilities Project 01/01 under SAF program is also appreciated.

REFERENCES

[1] M. Biswas and S. S. Ray, "Recent progress in synthesis and evaluation of polymer-montmorrillonite nanocomposites," in *New Polymerization Techniques and Synthetic Methodologies*, vol. 155 of Advances in Polymer Science, pp. 167–221, Springer, Berlin, Germany, 2001.

[2] D. Schmidt, D. Shah, and E. P. Giannelis, "New advances in polymer/layered silicate nanocomposites," *Current Opinion in Solid State and Materials Science*, vol. 6, no. 3, pp. 205–212, 2002.

[3] E. T. Thostenson, Z. Ren, and T.-W. Chou, "Advances in the science and technology of carbon nanotubes and their composites: a review," *Composites Science and Technology*, vol. 61, no. 13, pp. 1899–1912, 2001.

[4] A. K.-T. Lau and D. Hui, "The revolutionary creation of new advanced materials—carbon nanotube composites," *Composites Part B: Engineering*, vol. 33, no. 4, pp. 263–277, 2002.

[5] U. Schubert, N. Hüsing, and A. Lorenz, "Hybrid inorganic-organic materials by sol-gel processing of organofunctional metal alkoxides," *Chemistry of Materials*, vol. 7, no. 11, pp. 2010–2027, 1995.

[6] Z. L. Wang, Y. Liu, and Z. Zhang, Eds., *Handbook of Nanophase and Nanostructured Materials Vol. 4: Materials Systems and Applications*, Kluwer Academic/Plenum, New York, NY, USA, 2003.

[7] C. J. Brinker, Ed., *Better Ceramics through Chemistry III*, Materials Research Society, Warrendale, Pa, USA, 1988.

[8] C. J. Brinker and G. W. Scherer, Eds., *Sol-Gel Science: The Physics and Chemistry of Sol-Gel Processing*, Academic Press, New York, NY, USA, 1990.

[9] Z. Ahmad, "Ceramic-modified high temperature polymers," in *The Encyclopedia of Materials; Science and Technology*, K. H. J. Buschow, Ed., pp. 1086–1090, Elsevier Science, New York, NY, USA, 2001.

[10] Z. Ahmad and J. E. Mark, "Biomimetic materials: recent developments in organic-inorganic hybrids," *Materials Science and Engineering C*, vol. 6, no. 2-3, pp. 183–196, 1998.

[11] K. L. Mittel, Ed., *Polyimides and Other High Temperature Polymers. Vol. 2*, VSP, Leiden, The Netherlands, 2003.

[12] Z. Ahmad and J. E. Mark, "Polyimide-ceramic hybrid composites by the sol-gel route," *Chemistry of Materials*, vol. 13, no. 10, pp. 3320–3330, 2001.

[13] S. Wang, Z. Ahmad, and J. E. Mark, "Polyimide-silica hybrid materials having interfacial bonding through use of a sol-gel technique," *Macromolecular Reports*, vol. A31, supplements 3&4, pp. 411–419, 1994.

[14] S. Wang, Z. Ahmad, and J. E. Mark, "Polyimide-silica hybrid materials modified by incorporation of an organically substituted alkoxysilane," *Chemistry of Materials*, vol. 6, no. 7, pp. 943–946, 1994.

[15] J. C. Schrotter, M. Smaïhi, and C. Guizard, "Polyimide-siloxane hybrid materials: influence of coupling agents addition on microstructure and properties," *Journal of Applied Polymer Science*, vol. 61, no. 12, pp. 2137–2149, 1996.

[16] Y. Chen and J. O. Iroh, "Synthesis and characterization of polyimide/silica hybrid composites," *Chemistry of Materials*, vol. 11, no. 5, pp. 1218–1222, 1999.

[17] C. Xenopoulos, L. Mascia, and S. J. Shaw, "Variables analysis in the gelation of alkoxysilane solutions for the production of polyimide-silica hybrids," *Materials Science and Engineering C*, vol. 6, no. 2-3, pp. 99–114, 1998.

[18] P. Musto, G. Ragosta, G. Scarinzi, and L. Mascia, "Polyimide-silica nanocomposites: spectroscopic, morphological and mechanical investigations," *Polymer*, vol. 45, no. 5, pp. 1697–1706, 2004.

[19] C.-C. Chang, K.-H. Wei, Y.-L. Chang, and W.-C. Chen, "Synthesis and optical properties of poly(BPDA-ODA)/silica hybrid thin films," *Journal of Polymer Research*, vol. 10, no. 1, pp. 1–6, 2003.

[20] A. Al Arbash, F. Al-Sagheer, A. A. M. Ali, and Z. Ahmad, "Thermal and mechanical properties of poly(hydroxy-imide)-silica nanocomposites," *International Journal of Polymeric Materials*, vol. 55, no. 2, pp. 103–120, 2006.

[21] F. Al-Sagheer, A. A. M. Ali, S. Muslim, and Z. Ahmad, "Thermal and mechanical properties of chemically bonded aramid-silica nano-composites," *Science and Technology of Advanced Materials*, vol. 7, no. 1, pp. 111–118, 2006.

[22] C.-P. Yang and J.-H. Lin, "Syntheses and properties of aromatic polyamides and polyimides based on *N*-phenyl-3,3-bis[4-(*p*-aminophenoxy)phenyl]phthalimidine," *Journal of Polymer Science, Part A: Polymer Chemistry*, vol. 32, no. 2, pp. 369–382, 1994.

[23] Sh. Al-Kandary, A. A. M. Ali, and Z. Ahmad, "Morphology and thermo-mechanical properties of compatibilized polyimide-silica nanocomposites," *Journal of Applied Polymer Science*, vol. 98, no. 6, pp. 2521–2531, 2005.

[24] K. Yano, A. Usuki, A. Okada, T. Kurauchi, and O. Kamigaito, "Synthesis and properties of polyimide-clay hybrid," *Journal of Polymer Science, Part A: Polymer Chemistry*, vol. 31, no. 10, pp. 2493–2498, 1993.

[25] R. E. Southward, D. S. Thompson, T. A. Thornton, D. W. Thompson, and A. K. St. Clair, "Enhancement of dimensional stability in soluble fluorinated polyimides via the in situ formation of lanthanum(III)-oxo-polyimide nanocomposites," *Chemistry of Materials*, vol. 10, no. 2, pp. 486–494, 1998.

Hindawi Publishing Corporation
Journal of Nanomaterials
Volume 2006, Article ID 63608, Pages 1–5
DOI 10.1155/JNM/2006/63608

Nonlinear Optical Study of Nano-Sized Effects in a-Si : H Thin Films Deposited by RF-Glow Discharge

J. Ebothé,[1] K. J. Plucinski,[2] K. Nouneh,[3] P. Roca i Cabarrocas,[4] and I. V. Kityk[5]

[1] *Laboratoire de Microscopies and d'Etude de Nanostructures, Equipe d'Accueil N3799, BP 138, Universite de Reims, 21 rue Clément Ader, 51685 Reims Cedex 02, France*
[2] *Electronic Department, MUT University, ul.Kaliskiego 2, 00-908 Warsaw, Poland*
[3] *Laboratoire GES 2M, Univesite de Montpellier, 34095 Montpellier, France*
[4] *Laboratoire de Physique des Interfaces et des Couches Minces (CNRS UMR 7647), Ecole Polytechnique, route de Saclay, 91128 Palaiseau Cedex, France*
[5] *Institute of Physics, J. Dlugosz University of Czestochowa, Al. Armii Krajowej 13/15, 42-201 Czestochowa, Poland*

Received 22 August 2005; Revised 14 June 2006; Accepted 13 November 2006

We have evidenced the high sensitivity of infrared-induced second harmonic generation (IR-ISHG) to the structural changes occurred in amorphous hydrogenated silicon films (a-Si : H) prepared by RF-glow discharge technique at different substrate temperatures and doping types. In every case, a maximal signal of the IR-induced SHG is achieved at temperature of about 110 K and pump-probe delaying time about 22–39 ps. It indicates a marked effect of doped subsystems in the observed nonlinear optical effects. A substantial effect of doping is established from a drastic change of the IR-induced SHG behavior presenting an anomaly at about 400 MW/cm^2 for a pumping power with wavelength 1.54 μm. A minimum of the SHG is observed in that case for standard nondoped films. Note here that the doping type does not affect the behavior of the second-order nonlinear optical susceptibility. The thermo annealing leads to a slight decrease of the effective second-order susceptibilities. Larger changes are observed with doped samples for the pump-probe delaying time from about 39 till 24 ps.

1. INTRODUCTION

Amorphous hydrogenated silicon (a-Si : H) films are promising optoelectronic materials used as solar cell or other optoelectronic devices requiring additional investigations for a rigorous control of defects in the subsystems formed. These defects are crucially dependent on the method used and the conditions applied in the sample elaboration. In [1, 2], dealing with films obtained by RF glow discharge, it is shown that the decrease of substrate temperature below 200°C reduces the defect concentration. Moreover, the reduction observed elsewhere below 100°C [3, 4] has been explained either by the decrease of the deposition rate giving enough time to manifold precursors SiH_3 radicals to find the most favorable sites for incorporation into the film [5] or by the reduction of the polymerization process [6]. Another important aspect to be considered is the film's doping. For that purpose, a very close relationship between the film's microstructure and the degree of doping is reported in [7]. Following ellipsometry measurements, we have established that the imaginary part of the dielectric susceptibility is affected by the doping (*n*- or *p*-type) conditions. However, the results obtained from dc-conductivity and IR spectra cannot provide information concerning the hyperfine influence of the trapping levels formed by interfaces.

From this point of view, nonlinear optical methods and particularly the second-order ones seem to be more appropriate due to their high sensitivity to the low charge density redistribution of disordered materials [8]. Second-order nonlinear methods are forbidden in disordered media and it is necessary to have an additional external field to create long-range ordered alignment. This one could be an electric field, an optical, or a transverse acoustical one [9]. Several works exist now on the nonlinear optical properties of silicon, particularly those devoted to the two-photon absorption spectroscopy [10] and optical second-order harmonic generation in nanocrystallites (NC) [11]. The investigations on the stress/strain effects in silicon wafers grown on insulating substrates by optical second-order harmonic generation (SHG) are also proposed [12].

Recently, these effects have been ascribed to NC incorporated into polycrystalline films. Following the currently

adopted technique, we previously investigated a-Si : H films using an additional induced noncentrosymmetry by means of an external polarized transverse acoustical field [13]. A high sensitivity of the field-induced nonlinear optical method to the silicon films morphology was revealed, which cannot be analyzed by other methods. Therefore, one can expect that the filed-induced optical second harmonic generation may be useful for detection of trapping localized states, which are crucial for transport properties of the material.

Simultaneously, existence of nano-confined effects in large-sized NC possessing long-range ordering is already well known [14]. Nano-confined effects are mainly observed at the borders separating the nanoparticles and the surrounding substrate background. The grain-background interfaces of nanometer sizes can serve as a source of nano-confined quantized levels that could contribute to transition dipole moments determining the hyperpolarizabilities affecting the nonlinear optical effects. In [13], we have shown that an appropriately noncentrosymmetry stimulation of electrons by an external acoustical field could induce substantial noncentrosymmetric charge density distribution. For that purpose, the crucial role of the micro grain size in the observed effects was revealed. Applying an approach introduced for large-sized NC, one can expect a similar influence in the nanosheets (about several nm) separating the grains and their surrounding background. Previously performed molecular dynamics simulations have shown that the phase is formed at the borders separating the grains and background that are slightly different from the remaining background [8].

2. EXPERIMENTAL METHODS

2.1. Film deposition procedure

The investigated a-Si : H films were prepared by standard RF glow discharge on high optical quality CORNING glass substrates as described in [15]. We have varied several parameters. For the first group of the samples, we have varied substrate temperature and for the second one we have done *n*- and *p*-type doping. Two standard a-Si : H films, indicated by **S1** and **S2** were prepared (under standard conditions), that is, the dissociation of pure silane (10 sccm) at 40 mTorr under the RF power of 1 Watt and substrate temperature of 150 and 300°C, respectively. Three other samples were prepared at 50°C from the dissociation of 4% silane in hydrogen mixtures under a total pressure of 60 mTorr and an RF power of 1 Watt. Sample **S3** was intrinsic while phosphine was added to the mixture to obtain an *n*-type material (sample **S4**) and trymethylboron to obtain *p*-type a-Si : H film (sample **S5**). A synoptic view of the different investigated samples is proposed in Table 1.

Table 1: Labeling and the deposition conditions applied for the different investigated samples.

Samples labeling	**S1** standard	**S2** standard	**S3** intrinsic	**S4** intrinsic	**S5** intrinsic
Deposition temperature T_s (°C)	150	300	50 (undoped)	50 (*n*-type)	50 (*p*-type)
Deposition pressure P (mTorr)	40	40	60	60	60

2.2. Nonlinear optical setup

As a fundamental (probing) laser for the second harmonic generation, we have used pulsed 40 ps Q-switched Gd:YAG laser (presenting traditional Nd:YAG laser with the Gd-containing optical parametrical generator) operating at wavelength 1.76 μm, with pulse frequency repetition about 3 Hz (see Figure 1). Using parametrical generator from ZnSeTe single crystals cut under appropriate angles, we have obtained 16.0–17.5 ps durated laser pulses operating at 3.7 μm. The laser power density originated from the optical parametrical generator was varied within the 0.06–0.2 GW/cm^2. For the photoinducing changes, we have applied 20 ps Er-glass pulsed laser at $\lambda = 1.54\,\mu$m with pump power density continuously varying up to 1.2 GW/cm^2. Using a set of polarizers, we were able to operate by polarization of the incident and output laser beams. The delaying line DL allowed to operate continuously by delayed time between the pumping and probing laser beams. The grating monochromator allowed achieving the doubled frequency output SHG signal that was used for detection of the second-order optical susceptibility by a method described in [16]. The setup allowed the determination of second-order susceptibilities with a precision up to 0.1 pm/V.

3. RESULTS AND DISCUSSION

Figure 2 demonstrates a substantial difference of the SHG photoinduced behavior between the doped samples (**S4** and **S5**) and the undoped ones (**S1**, **S2**, and **S3**). In fact, the latter specimens show a substantial enhancement of SHG with the increase of photoinduced field from 0 up to 500 MW/cm^2.

Dependence of the effective second-order susceptibility d_{eff} versus the pump-probe delaying times is given in Figure 3 for doped and undoped samples. One can see that there exists a maximum of the second-order optical susceptibility at the pump-probe delaying times in the time interval 15 ps–42 ps. It clearly appears in this case that doped samples (**S5**) exhibit a sharper and higher response, their maximal position occurring at 23 ps instead of 39 ps of the undoped one (**S3**). Besides, the role of deposition temperature on the SHG behavior of a-Si : H films is evidenced in Figure 4 through the study of the second-order susceptibility. Sample **S3** deposited at 50°C exhibits a higher response than **S1** obtained at 150°C. Their particular maximum nonlinear optical (NLO) signals appear at about 120 K.

Such behaviors can be explained only within a frame of electric field induced SHG. These interactions stimulate additional noncentrosymmetry charge density, which is defined by the trapping level's number due to the dopant and the neighboring electron-phonon levels. At the same time, one

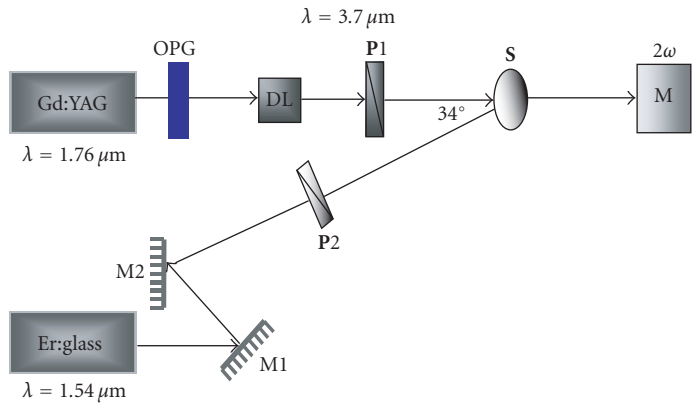

Figure 1: Principal experimental setup for the measurement of IR-induced SHG. All explanations on the process used are given in the text.

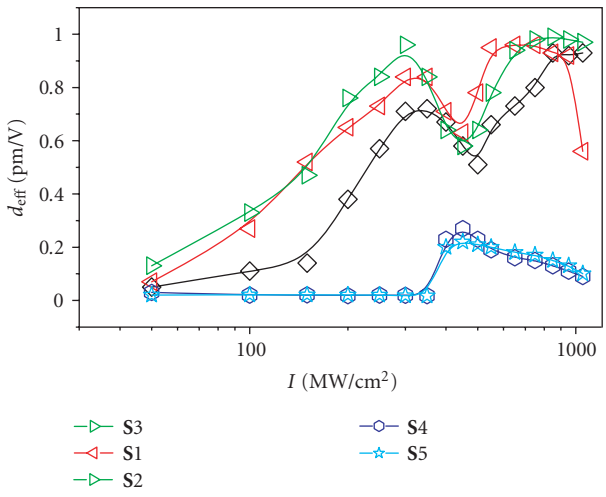

Figure 2: Photoinduced dependence of the efficient second-order susceptibility at fundamental wavelength 3.7 μm. The data are collected at optimal delaying time of every sample 20–30 ps, each of them being parallel to the polarization direction of the fundamental and pumping beam.

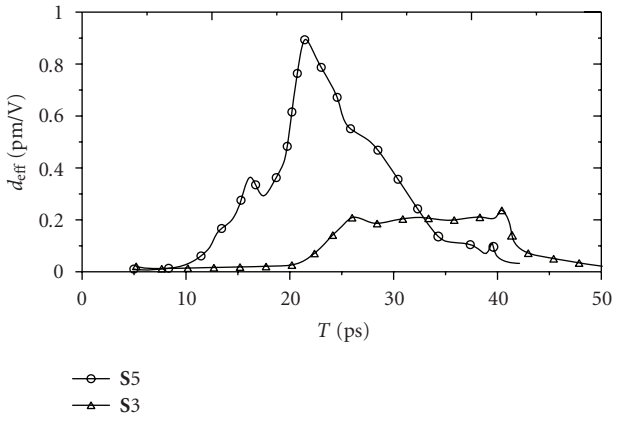

Figure 3: Typical pump-probe delaying dependence. The measurements are performed at 120 K.

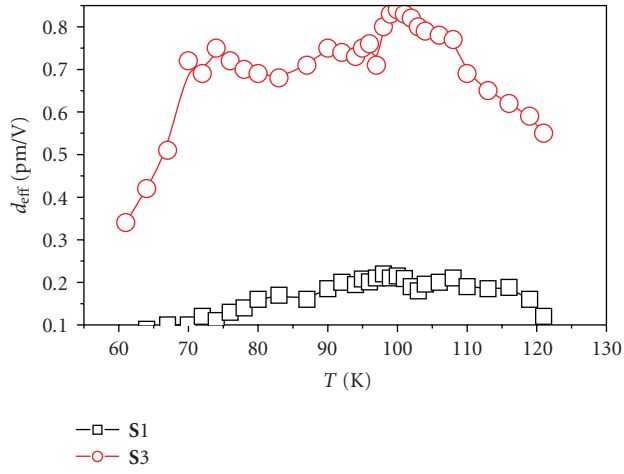

Figure 4: Temperature dependence of the efficient second-order susceptibility at optimal pump-probe delaying time.

can see in Figure 2 that the increase of substrate temperature leads to a slight decrease of the corresponding SHG dependence. This could reflect a decrease of trapping levels at the substrate-film interface. In addition, it appears that doping of p- or n-type gives almost the same behavior of the photoinduced SHG. This one indicates on a fact that origin of the doping (electrons or holes) do not change sufficiently transitions dipole moments determining corresponding hyperpolarizabilities and susceptibilities, which will be a subject of separate theoretical work in a future. One can therefore conclude that photoinduced nonlinear optics is more sensitive to the total number of the localized levels, contrary to the usual linear elipsometric measurements.

Another result reported in Figure 2 consists in an almost same value of photoinducing pump power at which exist minima and maxima of the second-order susceptibilities d_{eff} for the all investigated samples.

To have a physical insight of these results, a pump-probe NLO relaxation study of the samples has been performed.

From Figure 3, a marked increase of d_{eff} for the doped samples with respect to the undoped samples is clearly shown. This increase is almost two times larger than that of doped samples in the pump-probe range 20–39 ps. Considering the typical times for electron-phonon relaxation together with contribution of electron-phonon subsystems, one can expect an occurrence of additional IR-induced phonon mechanisms for hole and electron carriers which is quite different from that of subsystems of electron-phonon levels determining the photoinduced processes. The as-reported results appear only during the excitation and disappear out for the temperature region of about 110 K. It is necessary to emphasize that the observed second harmonic generation exists only during the photoinducing beam and completely disappears after its removement.

The observed effect is optimal at temperature range 80–120 K. There exists also a probability of an appearance a slightly modified structural phases at the borders separating the silicon films and the surrounding background. Our use of molecular dynamics simulations for the study of isostructural SiON films deposited on silicon [17] showed that for both sides of the interface there occurs a thin layer which can create a nanosheet with partial crystallization. Due to the thinner sheet, its structural control is possible only by photoinduced SHG.

By and large, it is assumed for nanocrystallites that two factors are responsible for this size-dependent SHG response: the size distribution of crystallites in film and the size distribution in a single crystallite due to random shape distortions [17]. In the case of amorphous-like films with partially nonhomogenous structure, nanoparticles could play the role of interface structure between the morphological grains and the background. It can be assumed that SHG is a result of the direct-gap Γ_{15}–$\Gamma_{25'}$ transitions in silicon nanocrystallites. Although the photon energy is less than the resonance value ($\sim$3.3 eV) for bulk silicon, the resonant SHG is achieved due to the band tail—band tail transition. The broadband tails inside the band gap of nanoparticles mainly consist of defect states that are created due to grain boundary defects. The exponential slope constants of band tails can be evaluated in 300–650 meV range. Therefore, the tail-to-tail transitions may be the possible reason of SHG response [18].

4. CONCLUSION

Following the performed photoinducing optical second harmonic generation, we have discovered a high sensitivity of SHG to the structural modifications occurred in hydrogenated silicon amorphous-like films due to some changes in their deposition conditions and doping. Considering the typical times for electron-phonon relaxation together with contribution of electron-phonon subsystems, one can expect an occurrence of additional IR-induced phonons which is quite different from that of subsystems of electron-phonon levels determining the photoinduced processes. We have found that the doping of the films leads to drastic changes of the IR-induced behavior of the SHG, possessing an anomaly for a pumping power of 1.54 μm at about 390 MW/cm^2, which becomes a minimum for the standard nondoped films. The thermo annealing leads to a slight decrease of the effective second-order susceptibilities. Larger changes are observed for the pump-probe dependences, particularly for the doped films. We observed in that case a decrease of the pump-probe delaying time from about 38 ps up to 25 ps. It is necessary to emphasize that the type of the doping does not influence substantially on the behavior of the second-order nonlinear optical susceptibility. It appears that doping of *p*- or *n*-type gives almost the same behavior of the photoinduced SHG. This one reflects a fact that origin of the doping (electrons or holes) does not change substantially transition dipole moments determining corresponding second-order hyperpolarizabilities and susceptibilities.

REFERENCES

[1] M. Kunst and H.-C. Neitzert, "The influence of deposition temperature and annealing temperature on the optoelectronic properties of hydrogenated amorphous silicon films," *Journal of Applied Physics*, vol. 69, no. 12, pp. 8320–8328, 1991.

[2] P. Roca i Cabarrocas, Z. Djebbour, J. P. Kleider, et al., "Hydrogen, microstructure and defect density in hydrogenated amorphous silicon," *Journal de Physique I*, vol. 2, pp. 1979–1998, 1992.

[3] Y. Hishikawa, S. Tsuge, N. Nakamura, S. Tsuda, S. Nakano, and Y. Kuwano, "Device-quality wide-gap hydrogenated amorphous silicon films deposited by plasma chemical vapor deposition at low substrate temperatures," *Journal of Applied Physics*, vol. 69, no. 1, pp. 508–510, 1991.

[4] M. K. Cheung and M. A. Petrich, "^{29}Si magnetic resonance study of amorphous hydrogenated silicon plasma deposited at 50°C," *Journal of Applied Physics*, vol. 73, no. 7, pp. 3237–3241, 1993.

[5] T. Kamei, G. Ganguly, N. Hata, and A. Matsuda, "Defect determination kinetics during the growth of a-Si:H," *Journal of Non-Crystalline Solids*, vol. 164–166, part 1, pp. 43–46, 1993.

[6] P. Roca i Cabarrocas, "Towards high deposition rates of a-Si:H: the limiting factors," *Journal of Non-Crystalline Solids*, vol. 164–166, part 1, pp. 37–42, 1993.

[7] P. Roca i Cabarrocas, "Deposition of intrinsic, phosphorus-doped, and boron-doped hydrogenated amorphous silicon films at 50°C," *Applied Physics Letters*, vol. 65, no. 13, pp. 1674–1676, 1994.

[8] O. Ostroverkhova, A. Stickrath, and K. D. Singer, "Electric field-induced second harmonic generation studies of chromophore orientational dynamics in photorefractive polymers," *Journal of Applied Physics*, vol. 91, no. 12, pp. 9481–9486, 2002.

[9] W. Gruhn, I. V. Kityk, and S. Benet, "Photoinduced optical second harmonic generation in Fe-Co metallic spin glasses," *Materials Letters*, vol. 55, no. 3, pp. 158–164, 2002.

[10] D. H. Reitze, T. R. Zhang, W. M. Wood, and M. Downer, "Two-photon spectroscopy of silicon using femtosecond pulses at above-gap frequencies," *Journal of the Optical Society of America B*, vol. 7, no. 1, pp. 84–89, 1990.

[11] D. E. Milovzorov, A. M. Ali, T. Inokuma, Y. Kurata, T. Suzuki, and S. Hasegawa, "Optical properties of silicon nanocrystallites in polycrystalline silicon films prepared at low temperature by plasma-enhanced chemical vapor deposition," *Thin Solid Films*, vol. 382, no. 1-2, pp. 47–55, 2001.

[12] Y. Gu, C. Hu, L.-J. Cheng, D. Y. Zang, and G.-P. Li, "Investigation of stress/strain of silicon on insulator using optical second harmonic generation method," in *Optical Characterization Techniques for High-Performance Microelectronic Device Manufacturing*, vol. 2337 of *Proceedings of SPIE*, pp. 93–102, Austin, Tex, USA, October 1994.

[13] J. Ebothé, I. V. Kityk, P. Roca i Cabarrocas, C. Godet, and B. Equer, "Acoustically induced optical second harmonic generation in hydrogenated amorphous silicon films," *Journal of Physics D: Applied Physics*, vol. 36, no. 6, pp. 713–718, 2003.

[14] K. J. Pluciński, I. V. Kityk, J. Kasperczyk, and B. Sahraoui, "The structure and electronic properties of silicon oxynitride gate dielectrics," *Semiconductor Science and Technology*, vol. 16, no. 6, pp. 467–470, 2001.

[15] P. Roca i Cborrocas, J. B. Chévrier, J. Huc, A. Lloret, J. Y. Parey, and J. P. M. Schmitt, "A fully automated hot-wall multiplasma-monochamber reactor for thin film deposition," *Journal of Vacuum Science & Technology A: Vacuum, Surfaces, and Films*, vol. 9, no. 4, pp. 2331–2341, 1991.

[16] I. V. Kityk, B. Marciniak, and A. Mefleh, "Photoinduced second harmonic generation in molecular crystals caused by defects," *Journal of Physics D: Applied Physics*, vol. 34, no. 1, pp. 1–4, 2001.

[17] D. Milovzorov and T. Suzuki, "Size-dependent second-harmonic generation by nanocrystals prepared by plasma-enhanced chemical-vapor deposition," *Applied Physics Letters*, vol. 75, no. 26, pp. 4103–4105, 1999.

[18] O. A. Aktsipetrov, P. V. Elytin, A. A. Nikulin, and E. A. Ostrovskaya, "Size effects in optical second-harmonic generation by metallic nanocrystals and semiconductor quantum dots: the role of quantum chaotic dynamics," *Physical Review B*, vol. 51, no. 24, pp. 17591–17599, 1995.